Cranfield University

Matthew Hockley

High Energy and High Intensity Electron and X-Ray Beams by Pyroelectric Effect

School of Applied Sciences

PhD

Academic Year: 2011-2012

Supervisor: Dr. Zhaorong Huang

25 July 2012

Cranfield University

School of Applied Sciences

PhD

Academic Year: 2011-2012

Matthew Hockley

High Energy and High Intensity Electron and X-Ray Beams by Pyroelectric Effect

Supervised by: Dr. Zhaorong Huang

25 July 2012

6

Abstract

The production of x-rays has been a useful technique in many areas of science, medicine and various industries for over 100 years. Over this time various new methods of generating x-rays have been produced, allowing improved performance in existing applications as well as the application of x-rays in new areas. In this project a novel method of electron beam production, with the potential for development into a novel method of x-ray production is presented, using both pyroelectric and ferroelectric materials.

The pyroelectric effect, i.e. the generation of a charge due to a change in temperature is an effect exhibited by certain dielectric materials. This effect has previously been used in x-ray generation, and has been suffiently successful that a commercial device has been produced: the Amptek Cool-X. While the Cool-X has only a limited electron / x-ray energy, high energy applications of this technology are present in the literature. This shows that these materials are capable of high voltages. However, the technique is not suitable for high beam intensity applications, limiting the potential use of pyroelectric x-ray devices.

Ferroelectric electron emission is a technique used to generate electron beams by applying a high voltage pulse to a specially prepared cathode. This technique has shown great potential for very high intensity pulsed electron beam generation. The major drawback of this technique is that while the cathodes are relitivly cheap and easy to produce, the other required equipment (such as high vacuum systems and high voltage pulse generators) is typically large and expensive. This project combines these two technologies to create an electron beam generation system that exhibits many of the advantages of each technology, while minimizing the drawbacks. The result is a device using pyroelectric materials as voltage generating

elements for electron acceleration and high voltage pulse production, while a ferroelectric cathode is employed as the electron generating element. This system has been shown to, depending on configuation, be capable of accelerating voltages above 5 kV, and generating total collected charges of more than -40 nC per pulse.

Acknowledgements

I would like to acknowledge the support and guidance provided by my supervisor, Dr Zhaorong Huang which has been invaluable throughout the course of this research. I would also like to thank Dr Chris Shaw, Mr Andrew Stellard and Mr Matt Taunt for their support and technical expertise which has been vital for the experimental phase of this project.

Thanks also go to my friends and colleagues from the Microsystems and Nanotechnology Center, including Dr Paul Jones, Dr Glenn Leighton, Dr Andy Pickwell, Mr Matt Stock, Mr Mark Tilman and Mr Tony Lusiola for their advice and moral support throughout this project. The moral support provided by my friends and family is also greatly appreciated.

Finally, I would like to acknowledge the financial support provided by the EPSRC and Cranfield University.

Contents

List of Figures

List of Tables

Nomenclature

Roman Symbols

$\alpha_{ij}^{T,E}$	Thermal expansion coefficient at constant stress and electric field
ϵ_0	Permittivity of free space
ϵ_r	Relative permittivity
$c_{ijkl}^{E,\theta}$	Elastic stiffness at constant temperature and electric field
C_{ext}	External capacitance
C_{ferro}	Capacitance of the ferroelectric cathode
C_{load}	Load capacitance
$d_{mkl}^{E,\theta}$	Piezoelectric constant at constant temperature and electric field
d_0	Size of microgap
d_{ferro}	Thickness of the ferroelectric cathode
E_c	Coercive field

$P_m^{S,E}$	Primary pyroelectric coefficient at constant strain and electric field
$P_m^{T,E}$	Total pyroelectric coefficient at constant stress and electric field
P_s	Spontaneous polarisation
V_{ferro}	Voltage across the ferroelectric cathode
V_{pyro}	Voltage across the pyroelectric material
V_{switch}	Voltage across switch/spark gap voltage
E	Electric field
FEE	Ferroelectric Electron Emission
$LiNbO_3$	Lithium Niobate
$LiNbO_3$	Lithium Niobate
$LiTaO_3$	Lithium Tantalate
OC	Open circuit condition
PZT	Lead Zirconate Titanate
SC	Short circuit condition
T_c	Curie temperature

Greek Symbols

ΔP_s	Change in spontaneous polarisation
ΔT	Temperature change
ρ	Pyroelectric coefficient

Chapter 1

Introduction

1.1 Research Rationale

The pyroelectric effect is the generation of an electric charge by a material subjected to a thermal stimulus. This electric charge is the result of a change in the spontaneous polarization of the material. This property has found use in many applications, such as thermal imaging [1], intruder detection [1], and more recently x-ray generation [2, 3, 4, 5] and neutron generation [6, 7]. As a result of the recent developments in pyroelectric x-ray generation a commercial device, the Amptek Cool-X [8] has been developed. The Cool-X has some serious limitations, such as its low x-ray energy and intensity. Possibility for further development of the technology underpinning the Cool-X is limited, so significant increases in performance from this method cannot be expected. This project proposes to combine pyroelectric crystals with a ferroelectric cathode, in order to produce high energy and high intensity of electron beam, and also X-ray beam when the high energy electron beam is used to hit a metal target. This is to be achieved by heating a pyroelectric material, which will generate the

charge needed to charge a capacitor. This capacitor will be switched to generate a high voltage pulse. This pulse will be used to fire a ferroelectric cathode, generating electrons. A second pyroelectric crystal will be heated, generating a voltage on an electrode. The electrons emitted by the ferroelectric cathode will be accelerated to high energy by this voltage.

The use of these techniques allows a potential device to maintain many of the benefits of the Cool-X, while allowing its shortcomings to be addressed. Factors affecting the intensity and the energy of the emitted electron beam will be investigated in order to obtain the in-depth understanding of the mechanisms involved in the processes, and also to maximise the power output of the proposed device.

The pyroelectric coefficient is normally measured at short circuit condition, i.e. the charge generated by the material per unit temperature change. Previous work has suggested that this may not always be appropriate since the pyroelectric coefficient may be different under open and short circuit condition [9, 10]. Since the pyroelectric elements in this project are in the open circuit condition experimental confirmation of this proposed effect would be desirable.

1.2 Research Objectives

This project aims to design and characterise a novel high energy high intensity electron beam generator based on pyroelectric crystals. More specific research objectives are:

1. High voltage pulse generation by pyroelectric effect. This high voltage pulse will be used to provide the driving voltage required for firing the ferroelctric cathode used later in this project.

2. Strong ferroelectric electron emission triggered by high voltage pyroelectric pulse. This will allow the emission of electrons from the ferroelectric cathode, which are to be accelerated by the second pyroelectric element later in this project.

3. Investigation of the effect of an accelerating voltage applied to the electron emission system

4. Pyroelectric electron acceleration system to generate high energy, high intensity electron beams

1.3 Research Methodology

1. Design and test a system for production of high voltage electrical pulses using a thermally cycled Lithium Tantalate ($LiTaO_3$) crystal, and compare these pulses to those produced by a commercial high voltage generator

2. Induce strong ferroelectric electron emission in Lead Zirconate Titanate (PZT) using a commercial high voltage pulse generator. Various pulse parameters will then be investigated to determine the optimum pulse properties. The pyroelectric pulse system will then be used to initiate strong ferroelectric emission, and various parameters investigated to improve emission porperites.

3. The system will then be modified to include an accelerating voltage on the anode. This accelerating voltage will be provided by an external high voltage generation system. Various parameters will be investigated to improve the performance of the system, with particular attention paid to the peak emitted current and the total emitted charge.

4. Finally, a second $LiTaO_3$ crystal will be added to the system to act as the voltage generation element for the acceleration of the emitted electrons. This system will demonstrate the feasibilty of an electron beam generation and acceleration device based on pyroelectric pulse and ferroelectric electron emission technologies.

1.4 Contents of this thesis

A brief overview of the work to be presented in the following chapters will be given in this section.

Chapter 2 provides a review of the existing literature relevant to this project. Pyroelectric materials will be discussed, as well as ferroelectric electron emission. An overview of an existing commercial device for the generation of electron and X-ray beams will also be given.

Chapter 3 covers the experimental methods used in this project. Two main types of experiment are presented here: those relating to the open and short circuit pyroelectric coefficient; and experiments relating to pulse generation with pyroelectric materials and electron generation from lead zirconate cathodes.

Chapter 4 presents the results and discussion of the open and short circuit pyroelectric effect experiments. The results of the use of both bare and laminar composites of pyroelectric lead zirconate titanate at both open and short circuit are presented.

Chapter 5 presents results showing the operation of the two basic components of the proposed electron / X-ray beam generation device: the pyroelectric high

voltage pulse generation system; and a ferroelectric cathode driven by this pyroelectric pulsing system. The results of an investigation of optimum pulse and circuit parameters is presented, and are explained in the context of surface plasma formation on the cathode.

Chapter 6 presents the results of using the system developed in Chapter 5 in conjunction with an accelerating voltage. Optimisation of the system is again undertaken, with modifications to the pulsing circuit improving performance. This improvement is again explained in terms of surface plasma formation on the cathode.

Chapter 7 presents the results of modification of the above system to incorporate a second pyroelectric crystal as the accelerating element. An investigation of the optimum configuration of this accelerating system was performed, and the results presented. A comparison of this system with the previous one is made, and the differences in performances between the two explained in terms of the surface plasma and electrical condition of the system.

Chapter 8 summarises the conclusion of the project, while chapter 9 presents future work which may be carried out to further develop the work of this project.

Chapter 2

Literature Review

This literature review will be split into several sections, reflecting the broad range of areas involved in this project. Initially the classes of materials used in this project will be introduced in the following order:

- The pyroelectric effect will be covered, with particular focus on the recent development of pyroelectric X-ray generation

- ferroelectric electron emission (FEE) will then be discussed, with a look at the various experimental procedures that may be used, especially with regard to the use or not of an accelerating voltage

- Discussion of the use of piezoelectric materials in high voltage electrical pulse generation will then be undertaken, with the similarity of such systems to a pyroelectric pulse generator as the focus

- Finally, a broader look at pyroelectric materials and their relation to piezoelectric materials will inform a discussion of the change in pyroelectric

coefficient under various situation. A particular interest is taken with regard to laminar composites of pyroelectric materials with non-pyroelectric materials, and the effect of the open and short circuit measurement regimes on the pyroelectric coefficient

Finally, the history of X-ray production will be discussed, leading to the development of pyroelectric X-ray production and the Amptek Cool-X device. A particular focus will be on the advantages of a miniature X-ray generator such as the Cool-X, as well as its limitations and scope for improvement.

2.1 Piezoelectricty, Pyroelectricity and Ferroelectricity

Piezoelectricity is a property present in a particular class of insulating materials. These materials are able to produce a voltage at their surfaces when a stress or strain is applied to them. This voltage is the result of the natural polarisation of the material being altered during the stress/strain. Pyroelectricity and ferroelectricity are material properties related to the more well known piezoelectricity. These materials are related in a form of hierarchy where all ferroelectric materials are pyroelectric and all pyroelectric materials are piezoelectric [1]. This is illustrated in Fig. 2.1. This hierarchy is the result of increasing restraints on the material properties at the unit cell scale: piezoelectric materials must have a non-centrosymmetric unit cell; pyroelectric materials must have both a non-centrosymmetric and polar unit cell; ferroelectric materials must have both these properties as well as the unit cell polarisation being reversible by an external electric field [11]. It is worth noting that all of these materials have a temperature at which their pyro- piezo and ferro-electric properties disappear:

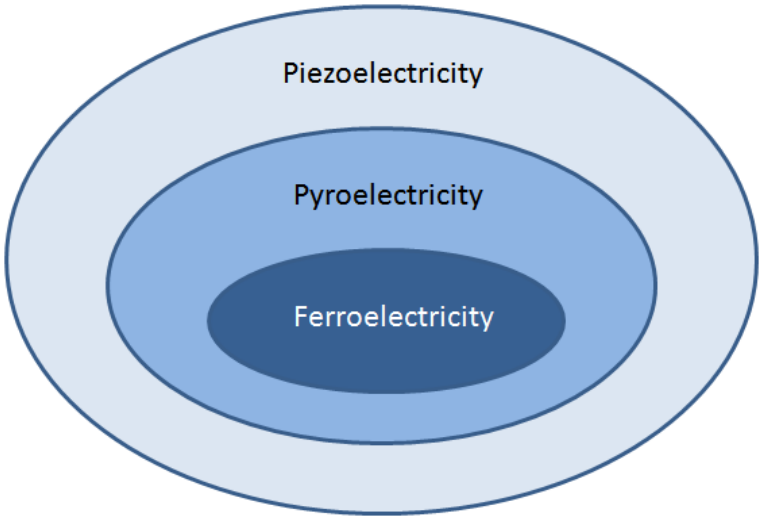

Figure 2.1: The relationship between piezo- pyro- and ferroelectric materials shown as a hierarchy

the Curie temperature, . Above the Curie temperature these materials undergo a phase change to any of a variety of other phases, which may be dielectric, antiferroelectric or paraelectric. The application of these materials to this project and the related literature will be discussed separately for each material type in the following sections.

2.1.1 Piezoelectricity

Piezoelectricty is the the most common of these three material properties, due to its less stringent material requirements: the material must be an insulator (dielectric), and must have a polar axis. These properties allow a charge to be generated on the surface of a piezoelectric material in response to a forced change in the shape of the material. Piezoelectric material have found wide application in areas such as transducers, sensors and actuators. more recently, research has found piezoelectric materials may have potential in high voltage pulse generation [12, 13, 14, 15], which will be discussed later in this chapter. The piezoelectric effect must also be considered in pyroelectricity, since any

thermal expansion will result in a piezoelectric response due to the secondary pyroelectric effect. This is discussed further in section 2.3

2.1.2 Pyroelectricity

Pyroelectricity is a property exhibited by certain polar dielectric materials in which a temperature change alters the polarisation of the material. This is shown mathematically in Eq. 2.1, where ΔP_s is the charge in spontaneous polarisation, ρ is the pyroelectric coefficient of the material, and ΔT is the temperature change the material undergoes.

$$\Delta P_s = \rho \Delta T \tag{2.1}$$

Pyroelectricity arises in crystalline materials, and can be understood from consideration of the unit cell of the material. The unit cell must be both symmetric about only one axis, and be polar. An example is the perovskite unit cell of $LiTaO_3$ / $LiNbO_3$, shown schematically in Fig. 2.2[2], which is both symmetric about only the Z-axis, and is polar, so is therefore a pyroelectric material. Fig 2.2 a) shows the material at above the Curie temperature, where the crystal is not polar, and b) at below the Curie temperature, where the crystal is polar. When the material is above the T_c the tantalum/niobium and lithium atoms are not displaced from the neutral position. However, below the T_c the material takes on a different structure where the tantalum/niobium and

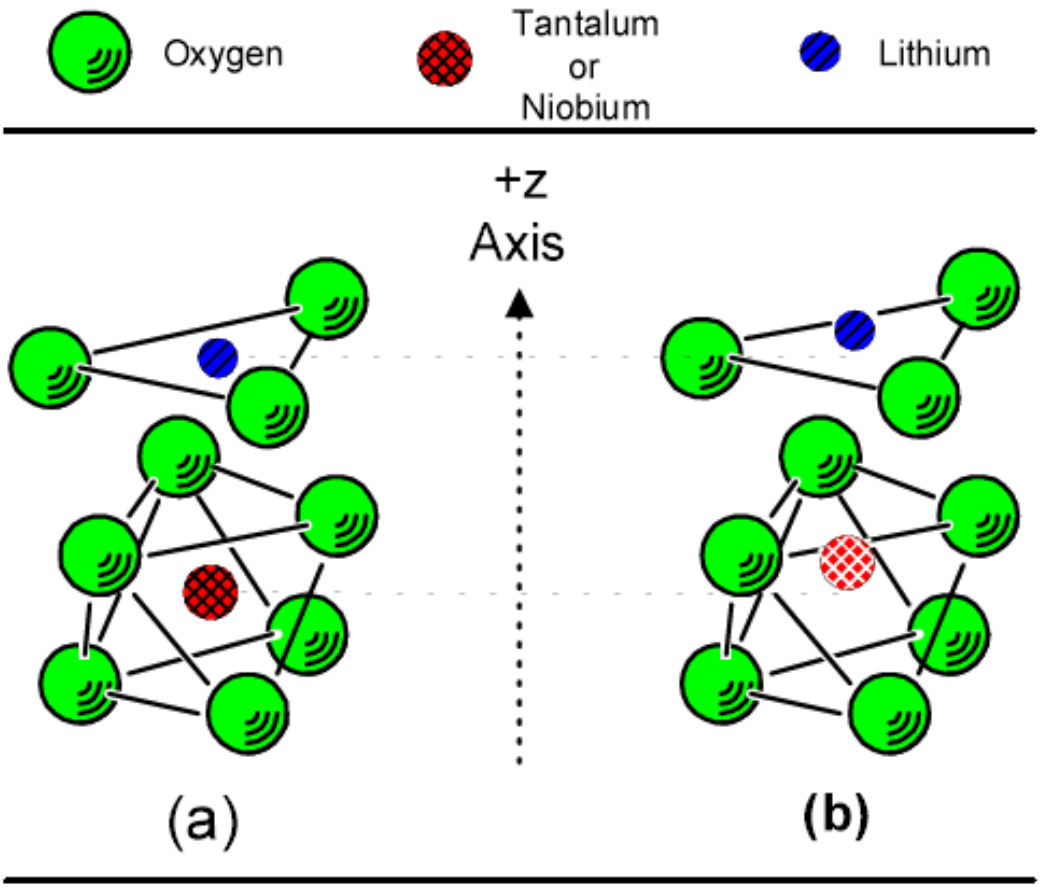

Figure 2.2: Simple representation of $LiTaO_3$ / $LiNbO_3$, to show the structure of pyroelectric perovskite materials

lithium atoms are displaced slightly along the Z axis, resulting in a polarization of charge along the Z axis.

Pyroelectric materials may today be found in a wide range of applications. Some of these applications may be familiar, such as motion detection by passive infrared (PIR) sensors, non-contact temperature measurement, and thermal imaging. Many new areas of application for pyroelectric materials have been developed more recently, such as X-ray generation[3, 2, 4] (see section 2.4.2), and the related technique of neutron generation[7], as well as other techniques such as lithography [16]. Recently the use of pyroelectric materials has also been demonstrated in mass spectroscopy applications [17].

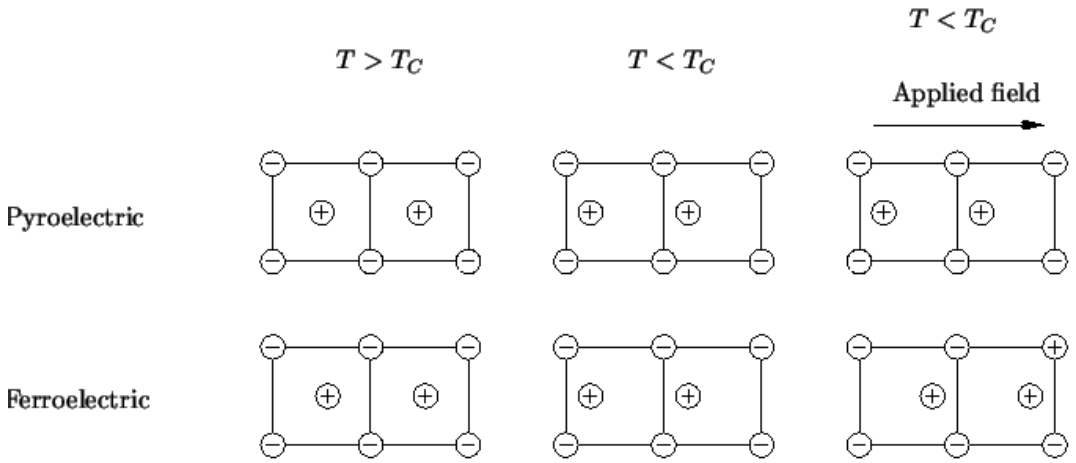

Figure 2.3: Reaction of pyroelectric and ferroelectric materials to temperature and electric field

2.1.3 Ferroelectricty

Ferroelectricity is a material property closely related to both pyroelectricity and piezoelectricity, but with the additional property of the spontaneous polarization being reversible by a sufficient external electric field.

Pyroelectric materials are also of the same family as ferroelectric materials. Ferroelectric materials have all the properties characteristic of pyroelectric materials, but also have the property that their polarisation vector may be reversed by a sufficiently strong electric field, known as the coercive field. The reaction of both pyroelectric and ferroelectric materials to temperature and electric field is illustrated in Fig. 2.3[11]. The Curie temperature T_c is the temperature at which a phase change occurs in the material, and it is no longer pyro/ferroelectric. The materials are shown both above and below T_c with no applied electric field, and below T_c with an applied field. These diagrams show that both materials behave in an identical fashion when no field is applied, but behave differently when an electric field is applied.

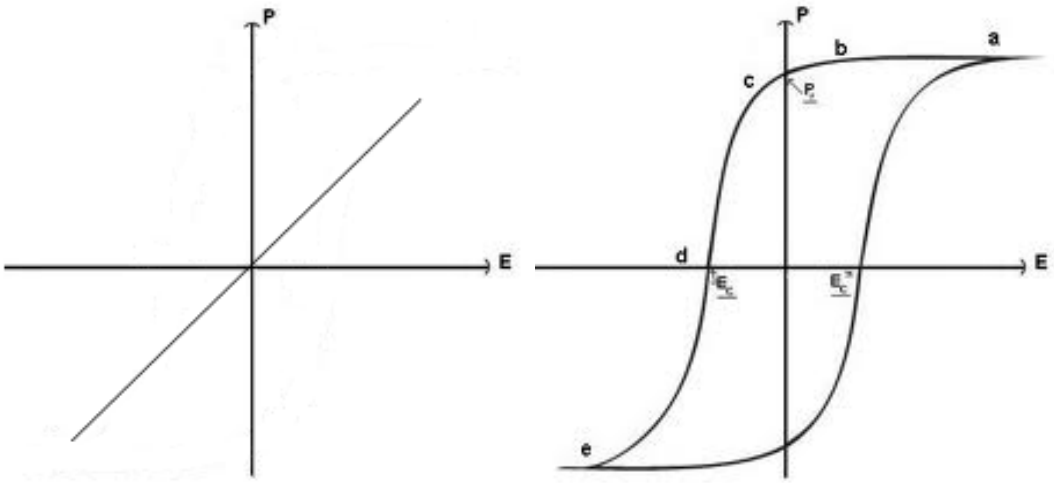

(a) Dielectric voltage/polarization behaviour (b) Ferroelectric voltage/polarization behaviour

Figure 2.4: Comparison of dielectric and ferroelectric polarization behaviour

2.1.4 Ferroelectric Electron Emission

Ferroelectric electron emission is a process used in producing pulsed electron emission. A typical experiment would use a thin ($\sim$ 1 mm) thick ferroelectric plate with a patterned electrode on the front surface and a solid electrode on the rear surface. The patterned electrode is often of the form of grids or stripes of 200 μm wide separated by 200 μm gaps. It should be noted at this point that ferroelectric electron emission may be considered a misnomer since it is the dielectric properties of the material that are relevant to the process, not the ferroelectric properties. This can be seen from various sources where a temperature change is used to induce a phase transition from ferro- to non-ferroelectric [18, 19, 20], or not prepoling the material [18]. However, the name ferroelectric electron emission is still widely used in the literature for this phemonenon.

2.1.4.1 Emission Mechanism

There are two proposed mechanisms by which ferroelectric electron emission may occur, which are summarised in the following sections

Polarisation Switching Mechanism [21] The mechanism proposed in the fast polarization change is that a fast rising high voltage pulse applied across a ferroelectric cathode with a solid rear electrode and a patterned front electrode. reverses the polarisation of the ferroelectric material. This would require a pulse of voltage great enough to exceed the coercive field of the cathode. The reversal of the spontaneous polarization of the material is proposed to release charges that were held to the ferroelectric surface by the surface charge. These charges are then collected by an anode. This process can be understood by considering the E-P (electric field - polarization) loop of a ferroelectric material as compared to a dielectric, as shown in Fig. 2.4. The polarization of the materials at various externally applied electric fields is plotted. Figure 2.4 a) shows the linear response of a dielectric material; the polarisation is directly proportional to the applied field. Figure 2.4 b) shows the response of a ferroelectric to an applied field. Point a shows the material at maximum polarisation with a large electric field. Reduction of this field to zero at point b has almost no effect on the polarisation of the material. Applying an electric field of opposite polarity then begins to reduce material polarization at point c. At point d the material polarization is zero; the external field at this point is the coercive field (E_c). The polarization continues to reverse until point e, where it reaches a maximum value, equal and opposite to the value at point a. The field is then increased again and the process continues back to point a. It is this property of ferroelectric materials that is used in this explanation of FEE. At atmospheric pressure the spontaneous polarisation (P_s) of the ferroelectric material is neutralised, or screened by free

ions and electrons in the air. When the ferroelectric material is place under high vacuum there is an insufficient number of these particles to quickly neutralise any change in P_s

Triple Point Emission The second mechanism, metal-dielectric-vacuum triple point emission works on the same principle as weak ferroelectric electron emission, but makes use of a special electrode arrangement. This results in the voltage pulse applied across the cathode being intensified at the interface of the ferroelectric (dielectric), grid (metal) and vacuum due to the microgaps formed between the surfaces. The level of enhancement of the field can be estimated as:

$$E = \frac{V \times \epsilon}{(d_0 \times \epsilon/d) + 1} \tag{2.2}$$

Where E is the electric field in the microgap, V is the applied voltage, ϵ is the cathode dielectric constant, d_0 is the microgap size and d is the cathode thickness[19]. This shows that a thin material with a rough surface is desirable. This intensification of the electric field at the triple points is thought to be sufficiently great that field emission of electrons can occur. These field emitted electrons are then accelerated along the surface of the cathode by a component of the electric field parallel with the cathode surface, which is provided by the grid structure of the front electrode. These electrons then avalanche along the surface, freeing further electrons and ions as they travel. The build up of the charged species on the surface of the cathode then results in the formation of a surface plasma, from which the charged particles are emitted. Various studied have also observed the emission of light associated with the formation of the plasma.

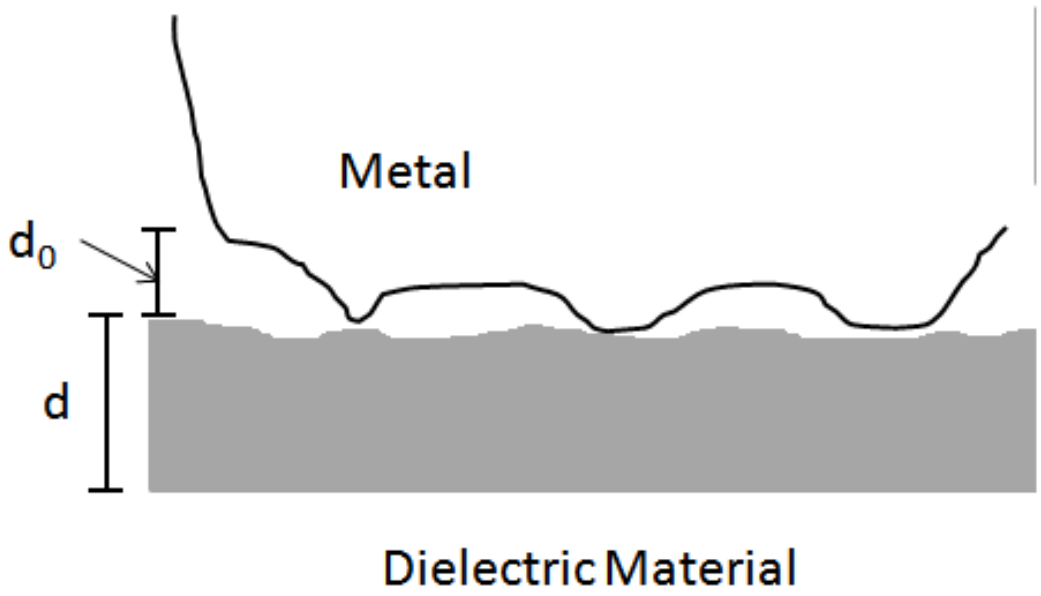

Figure 2.5: Schematic of a metal dielectric cathode, showing the microgaps d_0 formed between the two surfaces

Various studies have been performed to elucidate the correct mechanism involved in FEE. Many of these have focused on excluding the fast polarization effect, rather than the proof of the plasma assisted emission. In an attempt to exclude the fast polarization explanation experiments have been conducted which allow the ferroelectric material to be heated. This allows the state of the ferroelectric material to be changed by heating above the Curie temperature to another state, or sometimes several other states. A typical FEE experiment would then be carried out with the material in the ferroelectric state to confirm operation of the system. The material would then be heated to above its Curie temperature to cause a state change, and the experiment repeated. The emission of electrons in this non-ferroelectric state confirms that polar properties of ferroelectric are not important in this process. Further evidence can be provided by the fact that unpoled ferroelectric materials are able to be used for this process, as are electrical pulses of either polarity applied to either a front or rear electrode, which would not be possible if the polarization of the material needed to be reversed. While none of this directly proves the correctness of the triple point

emission hypothesis, it does provide support for it since none of the above factor disagrees with what would be expected such a system. More direct evidence for the triple point emission system is the observation of light emission by the system during the emission process, the only reasonable explanation for which is plasma formation. The physical wearing of the cathode surface (both metal and ferroelectric regions) has been observed [22], as well as the deposition of metal to the ferroelectric and ferroelectric to the metal. These precesses are also readily explained by the formation of plasma, but cannot be explained by the polarization switching mechanism.

Further evidence for the process being the triple point/plasma one will be discussed in the results section of this thesis, since the unique pulse generation system of this project has allowed certain phenomena to be observed that are likely masked by the pulse generation systems used in other research. These phenomena may all be explained by the formation of surface plasma on the emitting surface of the cathode.

The mechanism in ferroelectric electron emission is a relatively complex one which takes place over several stages. First, an electric field applied to either the solid rear electrode or the grid front electrode causes a very high electric field gradient in the gaps (due to the surface of the ferroelectric not being perfectly smooth) between the ferroelectric material and the metallic grid. This high electric field causes electrons to be emitted from the cathode by explosive electron emission. These electrons are then accelerated along the surface of the cathode by the component of the electric field parallel to its surface. These accelerated electrons collide with atoms in the surface of cathode, causing the formation of a surface plasma. Ions and electrons are then emitted from this plasma.

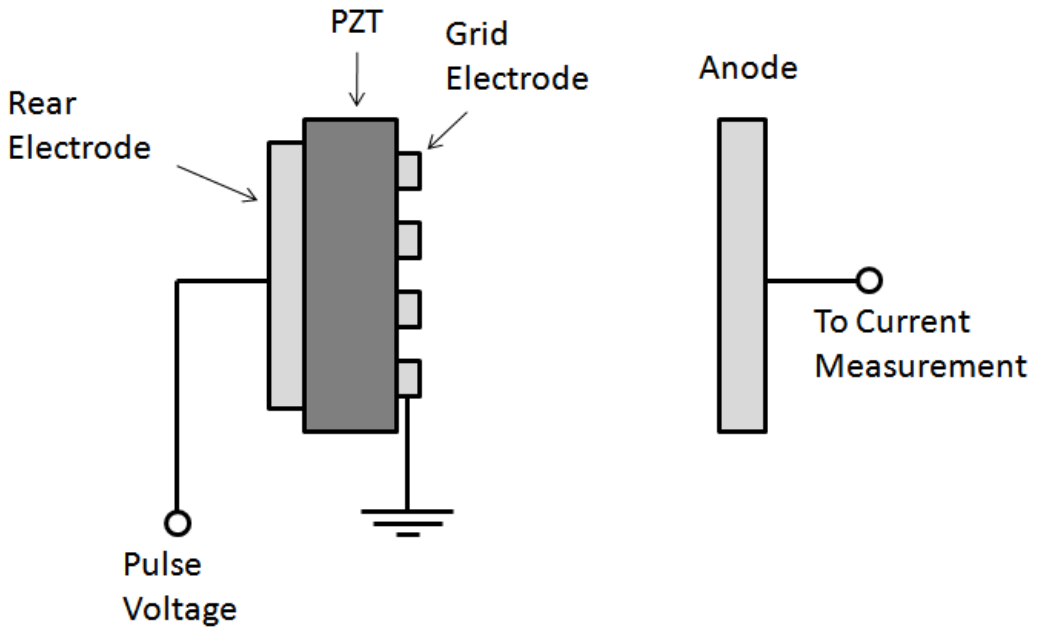

Figure 2.6: Schematic of a typical FEE system. Note that the pulse is applied to the rear electrode, and the front grid electrode is grounded

A more detailed explanation of the process of the plasma covering the surface of the cathode has been proposed by Peleg et al [23]. This work begins with the usual approach of triple point emission caused by a high voltage pulse applied to the rear of the cathode. This causes both a plasma to form on the front surface of the cathode, and the cathode to be dielectrically polarized. The authors then look at the propagation of the plasma across the ferroelectric surface, compensating the polarisation charges as it proceeds. The authors make the assumption that the voltage pulse driving the plasma formation is sufficiently high as to generate enough plasma to fully cover the ferroelectric surface. This has several consequences: first, this means that since the plasma is electrically conductive it will take on the voltage of the grounded front electrode, i.e. on the bulk scale the plasma is neutral. Secondly, it means that the ferroelectric cathode very closely resembles a perfect capacitor of two conducting surfaces separated by a dielectric. This second point is of particular importance to this analysis of the cathode since it gives a framework in which the process may be

considered. Once the polarisation charge of the ferroelectric cathode has been compensated by the plasma there remains charges within thee plasma which may be ejected towards the anode to be collected. The charge of the emitted particles depends upon the polarity of the applied voltage pulse; a positive voltage gives positive ion emission while a negative voltage results in electron emission.

2.1.5 Applied Voltage

The magnitude of the voltage, its polarity and the method of application of the pulse all have a significant effect on the emission process. It has been shown that there is a threshold voltage in the process, below which no emission may occur [24, 25]. Above this threshold the emitted charge and current have been observed to initially increase slowly, but a relatively small increase in voltage above the threshold will result in a rapid increase in both charge and current up to the point at which the sample succumbs to electrical breakdown. Some work has suggested that the polarity and application (front or rear electrode) are of importance to this process. Improved emission has been seen with negative pulses compared to positive pulses, and application of the pulse to the front electrode appears to result in better emission characteristics than a pulse applied to the rear electrode.

2.1.6 Without Accelerating Voltage

Much work focusses on the non-accelerated, or 'self emission' scenario. In this situation the triggering pulse is applied to the cathode, but no accelerating voltage is used to extract or accelerate electrons. This results in generally lower

peak currents than with the accelerated emission systems. A trend typically seen in this scenario is that increasing triggering voltage gives greater emitted charge / peak current [26, 27, 18, 28].

2.1.7 With Accelerating Voltage

Ferroelectric electron emission can be combined with a high voltage across the anode-cathode gap. This provides a voltage to extract electrons from the plasma produced by the FEE process. The aim of this is to increase the current density during the emission process. Two methods have previously been used to provide this extraction voltage: a steady DC field, and a pulsed field.

2.1.7.1 DC Accelerating Voltage

Most of the work on accelerated ferroelectric emission has focussed on the use of a DC acceleration/extraction voltage. There is large variation in the voltages used in the acceleration process depending on the experimental set-up; the voltages are usually well below 1 kV or at least several tens of kV. Almost no work has investigated the intermediate range.

The use of an accelerating voltage on the anode of the ferroelectric electron emission system has been shown to result in significant increases in the peak emission current and total charge during an emission event[24, 29, 30]. The application of a DC accelerating field has also been seen to increase the width of the electron pulse in some cases[31]. The use of a wide range of acceleration voltages has been used in ferroelectric emission, from a few hundred volts [32] to several hundred thousand [33].

2.1.7.2 Pulsed Accelerating Voltage

Little work has been conducted on the use of electrical pulses in the acceleration, perhaps due to the technical difficulty in developing a system which can apply the pulse at an accurately timed interval after the triggering of emission. A further barrier to this work is that a system which can both apply an accelerating pulse and measure the emission pulse is technically challenging. Hence the limited literature on this area of research. However, work has shown that the timing of a pulsed accelerating voltage changes the emission properties of the system [33].

2.2 Piezoelectric High Voltage Pulse Generation

Little work has been done with regard to the production of high voltage pulses with piezoelectric materials. However, the work which has been done has some use with regard to the pyroelectric pulse generation section of this project. Experimental and modelling work has been conducted on piezoelectric pulse generators [34, 12, 13, 14, 35, 15, 36], mainly focussing on the a method using a large mass bonded to a stack of piezoelectric elements. The piezo stack/mass construction would be then subjected to a large force, either through firing at a solid surface, or by dropping. The sudden large force applied would cause a substantial compression of the piezoelectric stack, which in turn would generate a large voltage on the device. A schematic for a typical device is shown in Fig 2.7. This method has been used by T. G. Engel et. al. to produce high voltage electrical pulses, with power up to 25 kW into 10 Ω [13]. This method used a compressed gas gun to accelerate a device similar to that in Fig. 2.7 into a target. The rapid deceleration upon striking the target induced a large force on the

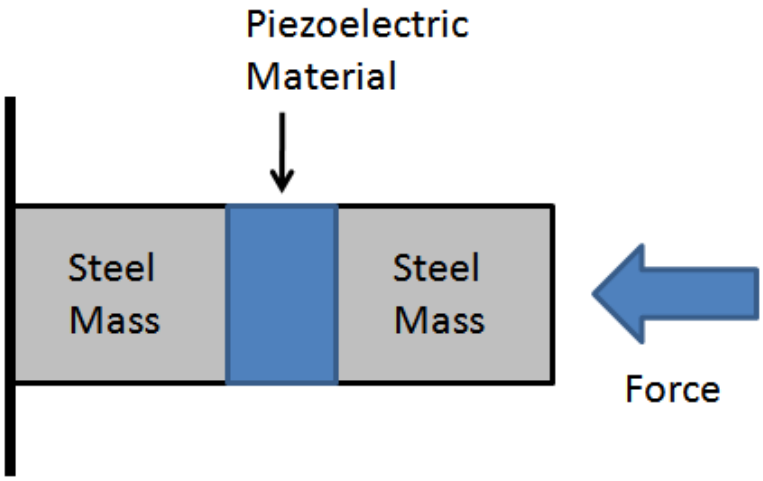

Figure 2.7: Schematic of a typical piezoelectric pulse generation system

piezoelectric element, deforming it. The deformation of the piezoelectric element causes charge to be generated at is surface, which causes a voltage across the capacitor-like element. This voltage increases with increasing force/deformation until it exceeds the breakdown voltage of a spark gap switch connected to it, at which point a current will flow through the load. These devices are of interest due to their similarity to the pyroelectric pulse generation system of this project.

2.3 Open Circuit Pyroelectric Coefficient

The pyroelectric coefficient is always quoted in literature under the short circuit condition, and it is usually assumed that there is no difference between its value at open and short circuit condition. Recent works [9, 37, 10, 38] have challenged this assumption by developing a numerical model for the open circuit pyroelectric coefficient. This model was used to generate theoretical values of the open circuit pyroelectric coefficients of several common pyroelectric materials. Chang and Huang state that the pyroelectric coefficient for the open circuit

condition is:

$$P_m^{T,E} = P_m^{S,E} + d_{mkl}^{E,\Theta} c_{ijkl}^{E,\Theta} \alpha_{ij}^{T,E} \tag{2.3}$$

$P_m^{T,E}$ is the total pyroelectric coefficient at open circuit condition, $P_m^{S,E}$ is the primary pyroelectric coefficient (which is invariant under open or short circuit condition), $d_{mkl}^{E,\Theta}$ is the piezoelectric constant (also invariant under open or short circuit condition), $c_{ijkl}^{E,\Theta}$ is the stiffness constant. This equation gives the pyroelectric coefficient at the open circuit condition. Enhancement of the pyroelectric coefficient under open circuit condition has been theoretically predicted [10] and experimentally verified [39, 40].

2.3.1 Pyroelectric Coefficient Enhancement

The enhancement of the pyroelectric coefficient is of interest due to the many applications in which pyroelectric materials are found. Enhancement of the pyroelectric coefficient will enable improvements in many applications of pyroelectric materials, in particular energy harvesting. Various techniques have been investigated to increase the pyroelectric coefficient of various materials. The use of the secondary pyroelectric coefficient as the means to increase the pyroelectric coefficient was investigated by Newnham at al. [41] and Nan [42].

Fig. 2.8[43] gives a representation of the effects of thermal, mechanical and electrical inputs. In particular it shows the relationship between an input of heat and an electrical output i.e. the pyroelectric effect. Of particular interest is the fact that the pyroelectric effect can be achieved by two main routes. The first is

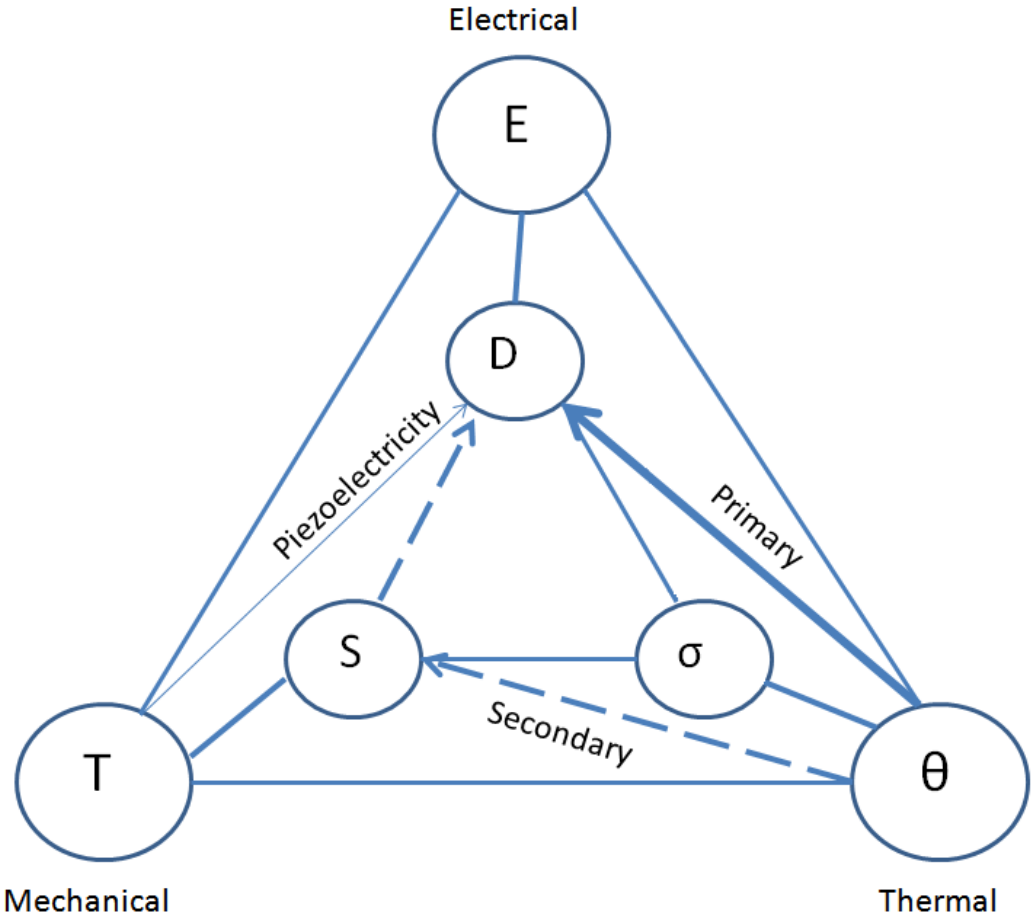

Figure 2.8: Routes by which the pyroelectric effect can be achieved.

the primary pyroelectric effect: a thermal input causes a change in the entropy of the crystal, which then leads to a change in the electrical displacement of the material. The second is the secondary effect, where a change in entropy causes a change in strain, from which the piezoelectric effect causes and electrical response. This gives an explanation as to the origin of the secondary pyroelectric effect of Eq. 2.3[10]: $d_{mkl}^{E,\Theta} c_{ijkl}^{E,\Theta} \alpha_{ij}^{T,E}$, which is the component of the total pyroelectric effect that is caused by the non-direct, piezoelectrically induced pyroelectricty. This aspect of pyroelectricity has been the focus for work attempting to increase the total pyroelctric effect.

2.4 X-Rays

2.4.1 Conventional X-Ray Production Methods

X-rays are a form of electromagnetic radiation with energy in the range 120 eV to 120 keV. They are often broadly divided into two categories: hard and soft X-rays. These two categories roughly separate the more penetrating (hard) X-rays from the less penetrating (soft) X-rays. This distinction, though rough is useful in many practical applications since only one of the two types is typically useful in any particular application. Hence X-ray energy is an important factor in any X-ray application. A second major consideration is the intensity of the X-rays.

The earliest method of X-ray production is the Crookes tube. Its principle of operation is simple: an anode and cathode, held under vacuum are subjected to a large electric field, causing ionisation of atoms within the partial vacuum. The electrons released in the ionisation process are then accelerated towards the anode, colliding with gas atoms and molecules remaining in the dilute gas of the vacuum. These collisions, assuming sufficient energy has been imparted to the electrons by the electric field, generate further free electrons as the particles involved in the collisions are ionised. This results in a significant electron current beging accelerated towards the anode, and producing X-rays upon collision with it. The vacuum is typically in the region of 10^{-4} torr [44], since this region of vacuum is sufficient to prevent electrical breakdown between the anode and cathode, but still retains sufficient particles to allow avalanche ionisation to take place. Fig. 2.9[45] shows a schematic of the device.

A more recent and more useful device is the Coolidge tube, which at first may seem similar to the Crookes tube, but has a significantly different mode of

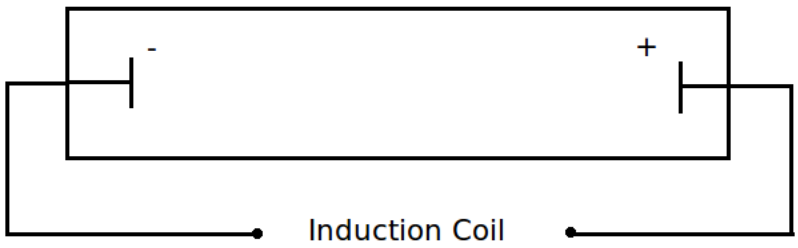

Figure 2.9: schematic of the Crookes tube X-ray device

operation. This device again consists of an anode and a cathode under high vacuum conditions. The anode may be very similar the that of the Crookes tube, and is held at a high positive voltage. However, the cathode is very different. The cathode is constructed from a coil of wire, which is heated to incandescence by a low voltage power supply. This causes the wire to emit electrons via thermionic emission. These electrons are then accelerated towards the anode by the voltage gradient in the anode cathode gap. This voltage may be provided by a negative voltage on the cathode alone, or a negative voltage on the cathode and a positive voltage on the anode. It should also be noted that the vacuum of the Coolidge tube is frequently higher (i.e. lower pressure) than that of the Crookes tube, since the ionisation of gas within the chamber is not desirable for its operation. A schematic of this device is shown in Fig. 2.10[46].

The Coolodge tube has many advantages over the Crookes tube. Chief amongst these is the separation of the electron beam generation system from the acceleration system; the incandescent cathode controls electron production while the voltage between the anode and cathode controls the electron energy. In the Crookes tube the electron current is a function of the anode-cathode voltage (as well as other factors, including tube pressure). This means that the Coolidge

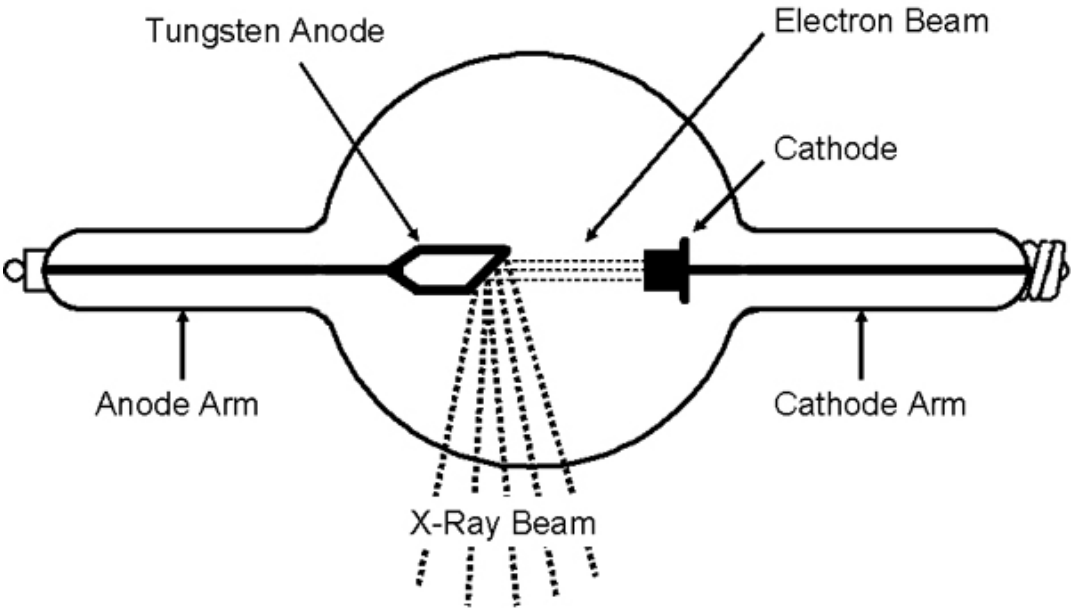

Figure 2.10: Schematic of the Coolidge tube X-ray device

can be used for various applications, due to the wide range of electron currents and energies available, while the Crookes tube is much more specialised, due to its limited range of outputs. From this comparison it is obvious that there is a significant advantage in separation of the electron production stage and the acceleration stage. Most of the current X-ray tubes in use are Coolidge tubes.

2.4.2 Pyroelectric X-Ray Generation

Pyroelectric X-ray generation is the generation of X-rays using a pyroelectric material such as $LiTaO_3$ or $LiNbO_3$. A typical experimental pyroelectric X-ray generation system may be constructed and operated as follows: the pyroelectric material is mounted to a heating or cooling device and placed within a vacuum chamber. The chamber is then evacuated to at least rough vacuum. The pyroelectric material is then heated or cooled. This results in a change of the pyroelectric materials spontaneous polarisation, which, since the material is under the open circuit condition produces a voltage across the materials

Z-faces. In this open circuit regime the pyroelectric material acts in a similar manner to a capacitor in parallel with a current source, an equivalent circuit for which is shown in fig. 2.11[5]. It is therefore convenient to model the electrical properties of a pyroelectric material on a capacitor. The low dielectric constant of typically used materials ($\epsilon = 43$ for $LiTaO_3$ and 29 for $LiNbO_3$ [47]), and dimensions typically on the order of 1 cm^3 lead to very low capacitance. This combined with the high pyroelectric coefficient of these materials results in very high voltages with modest temperature changes: 215 kV has been achieved with a temperature change of 165°C when using a double crystal geometry similar to that shown in Fig. 2.13 [5]. The mechanism for production of high energy electrons by pyroelectric effect is as follows: the pyroelectric material is subjected to a temperature change while under vacuum; this temperature change results in a change in the spontaneous polarisation of the crystal (see Eq. 2.1. Since the surface charge due to the spontaneous polarization of was previously masked by charges acquired from the atmosphere, i.e the surface appeared neutral prior to the temperature change, a voltage now appears across the Z faces of the material. As the temperature change increases the voltage generated increases. Assuming no charge leakage through the material and the absence of electrical breakdown, this voltage will continue to rise. The voltage will then reach a point where it begins to ionize any remaining gasses within the vacuum chamber if they pass close to a Z face. When the atom is ionized to an electron and positive ion, one charged species will accelerate towards the pyroelectric material while the other will be accelerated away from it.

This high voltage ionises residual gas particles within the vacuum chamber, resulting in particles of opposite charge to the exposed Z-surface of the pyroelectric material being accelerated towards it, and particles of opposite charge

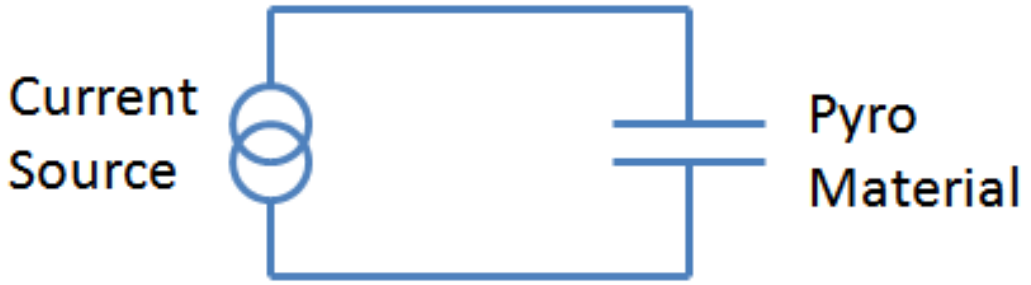

Figure 2.11: Equivalent circuit for charging pyroelectric material

being accelerated away. Both of these processes are useful for X-ray generation: electrons accelerated into the pyroelectric material or a metal target will produce both Bremsstrahlung and characteristic X-rays.

Early work on pyroelectric X-ray production was conducted using thermally cycled $LiNbO_3$ [48].

Pyroelectric electron emission is a cyclic process, with both a heating and cooling phase. A simple cycle is illustrated in Fig. 2.12. The pyroelectric material is initially at temperature T_1. At this temperature there is no net charge on the Z+ and Z- faces, as the material is above its Curie temperature, and is therefore not pyroelectric. The pyroelectric material is then cooled from T_1 under vacuum. As the material is cooled through it's Curie temperature it undergoes a change of state and becomes pyroelectric. At temperature T_2 a spontaneous polarisation is present in the material, which is compensated by screening charge. This results in a zero net charge on the Z+ and Z- faces. As the material is cooled further to temperature T_3 the spontaneous polarisation changes according to the relationship given in Eq. 2.1, resulting in an increase in the charge density on the Z+ and Z- surfaces. Ions in the region of the material are accelerated towards or away from the Z surfaces depending on the electrical polarity of both the ion and Z surface. If left for a sufficient time at T_3 the charge resulting from the spontaneous polarisation will be neutralised by ions, leading to the T_3 state on the right of Fig. 2.12[49], where the net charge on each Z surface is again

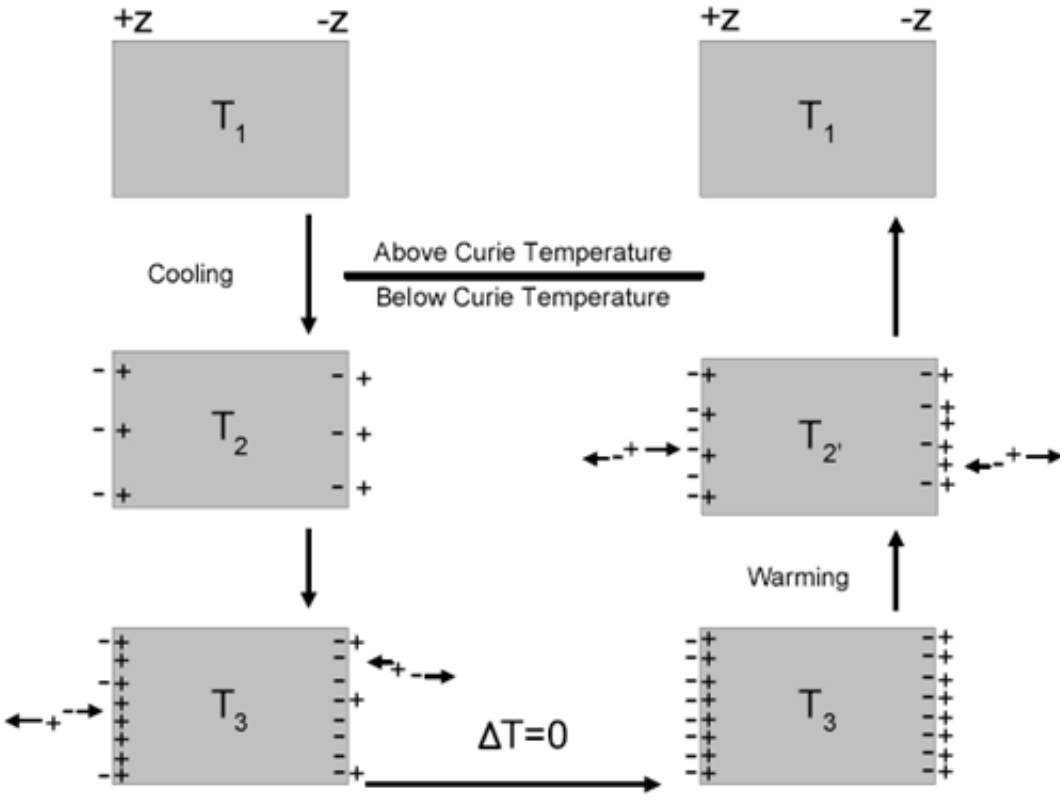

Figure 2.12: Thermal cycling of a pyroelectric material to generate X-rays

zero. Heating from this state to T_2' then begin to reverse the process, with each Z surface now attracting the charge that it previously repelled and vice versa.

A development of this technique to improve both the maximum possible voltage and the total charge produced is the double crystal geometry. This method uses two pyroelectric crystals orientated so that the Z+ face of one is facing the Z- face of the other. This is shown schematically in fig 2.13

2.4.3 The Amptek Cool-X

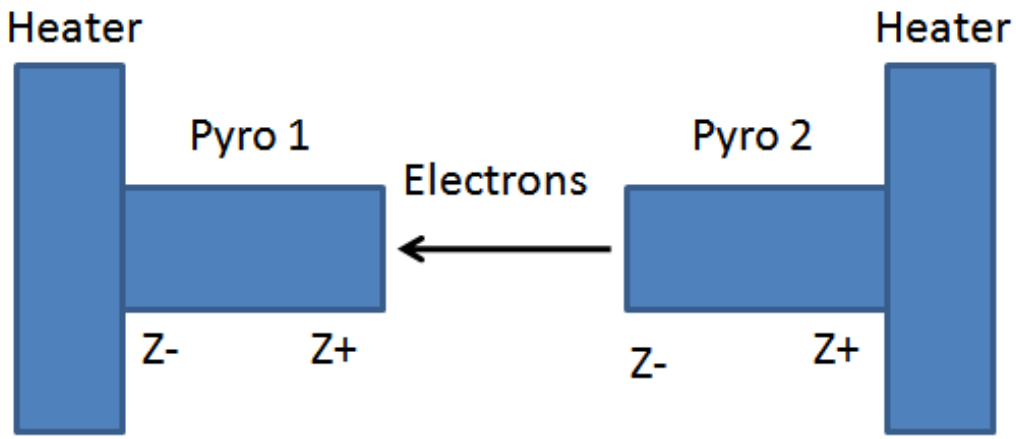

Figure 2.13: The double crystal geometry for enhanced X-ray production

The Amptek Cool-X, the active element of which is depicted in Fig 2.14[8] is a miniature X-ray device based on pyroelectric X-ray generation. It is designed to have several advantages over traditional X-ray sources, such as Coolidge tubes or radioisotopes. Amongst its benefits are its small size, light weight, robustness and on board power supply (via battery). These features make it an attractive device for many applications, such as XRD. The device has serious limitation however, which may have limited is widespread adoption. The peak X-ray energy is 35 keV due to the temperature change limitations of the device, with almost all X-rays below 10 keV. This energy is too low for many applications to be practical; an X-ray of a mummified field mouse takes 3 run cycles, which takes between 6 and 15 minutes. This is also related to the limited electron current available in a pyroelectric system; such systems typically have an electron current 3-6 orders of magnitude less than a commercial Coolidge tube for many applications. A further limitation is the lifetime of the device, which may be as short as 200 hours of operation, as stated by the manufacturer. The variation of the X-ray flux with time is also a major problem for the Cool-X, since this prevents many applications being feasible. However, the greatest limitation of the Cool-X technology is that all of these issues are inherent to the method of producing X-rays by pyroelectric effect, and there is only very limited potential

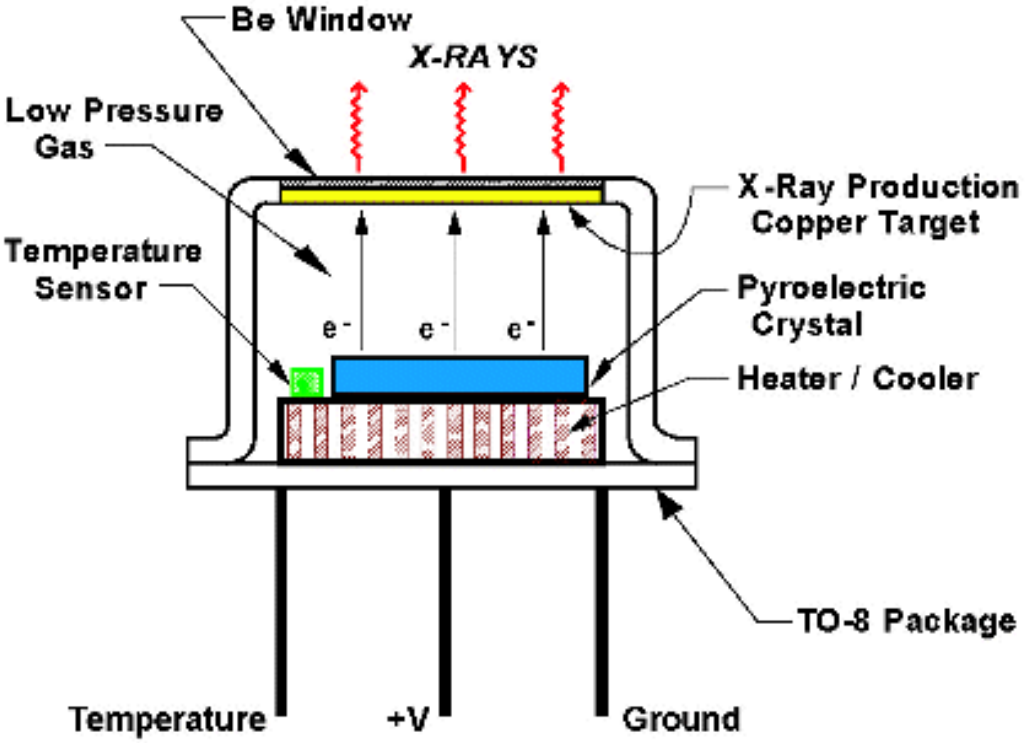

Figure 2.14: Schematic diagram of the Amptek Cool-X device

for the improvement of the technique. Despite the above shortcomings, the Cool-X has been recognised as an innovative device, being awarded the R&D 100 Award in 2003 [50].

The Cool-X, shown schematically in Fig 2.14 shows how the device operates. The pyroelectric material is heated by the heating element, causing the change in spontaneous polarization, which results in pyroelectric electron emission. These electrons are accelerated by the field produced by the pyroelectric crystal and collide with the thin copper target. This produces characteristic copper X-rays as well as a Bremsstrahlung continuum. These X-rays then pass through the Beryllium window and on to their desired target. Figure 2.15[8] shows a typical set up with the device.

Figure 2.15: Photograph of the Cool-X being used to analyse a material with an X-ray detector

Chapter 3

Methodology

3.1 Overview of Experimental Systems

Several experimental set ups are used in this project, which are broadly similar, but have several significant differences. These systems will be summarised in this section, with full details given later in this chapter.

The first system was that used in Chapter 4, for open and short circuit measurements of the pyroelectric coefficient of PZT. Two types of PZT were used in this chapter: PZT-5A and PZT-5H. Two methods were used for pyroelectric coefficient measurments: an electrometer in current (short circuit) and voltage (open circuit) modes; and a a voltage follower circuit directly connected to the sample (open circuit) and with a parallel capacitor (short circuit). Both of these systems used a Peltier element to heat and cool a plate in a vacuum chamber to change the temperature of a pyroelectric PZT sample. The electrometer system used was operated at a vacuum of around 100 mTorr and the voltage follower system was operated at around 0.01 mTorr.

Several systems were used in Chapter 5. Initially an external high voltage pulse generator was used to fire a ferroelectric cathode. Emitted ions and electrons were collected and the current and charge measured using a Faraday cup. The cathodes in all experiments from this point were contructed from ceramic PZ34, supplied by ferroperm. This material was chosen primarily due to it's dielectric constant of 210, which allowed cathodes with the correct capacitance and of practical physical dimensions to be made.

A second series of experiments, presented in Chapter 5, used a pyroelectric $LiTaO_3$ crystal undergoing a temperature change to charge a capacitor. When charged to a certain voltage the capacitor was discharged through a spark gap switch, and the pulse applied to a load capacitor. The voltage profile across this load capacitor was measured using a voltage divider. This pulse generating system was then used in place of the external pulse generator to fire the ferroelectric cathode, resulting in a ferroelectric electron emission system using a heated pyroelectric crystal to provide the triggering voltage. Various system parameters were then investigated to improve emission properties.

pyroelectric pulsing circuit / ferroelectric cathode system developed in Chapter 5 was then modifed in Chapter 6 by applying an accelerating voltage to the anode/charge collector. The voltage on this anode was provided by an external voltage generator. Modifications were also made to the pyroelectric pusling and ferroelectric cathode system to improve performace.

Chapter 7 uses a modified version of the system in Chapter 6. A second $LiTaO_3$ crystal is used to generate the accelerating voltage in place of the external voltage generator system. This crystal is connected to the anode, and has a capacitor connected in parallel to it. This capacitor was used to adjust the voltage generated on the anode by a temperature change of the pyroelectric

crystal. This completed system demonstrated an electron emission system based on a ferroelectric cathode driven by a pyroelectric pulse generator, with electron acceleration voltage provided by a second pyroelectric system.

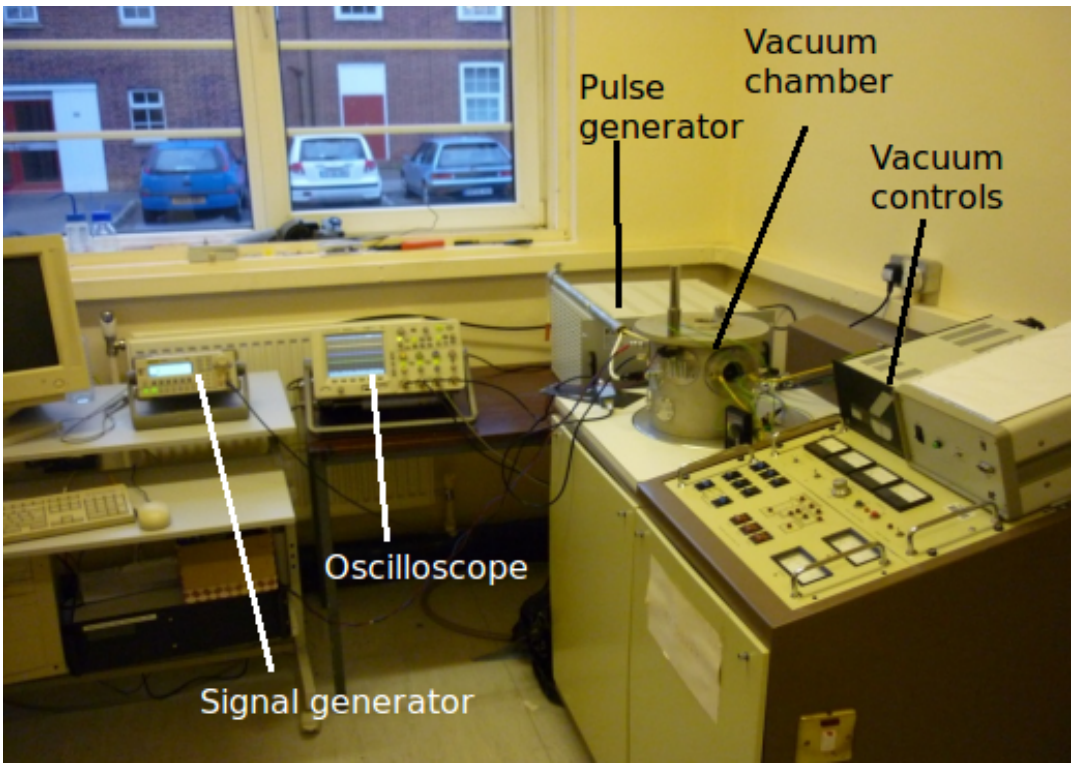

Figure 3.1: Photograph of the entire system, showing the vacuum system, high voltage pulse generator, oscilloscope, and related components.

3.2 General Experimental Procedure

The basic experimental procedure and apparatus will be outlined in this section, while the specifics for each experiment will be detailed in the relevent section later in this chapter.

A cathode was manufactured as described above. This cathode was placed in the vacuum chamber, and the electrical connections made to the pulsing

system. Electrical connections are made to monitoring systems in the relavent systems. The anode was mounted in the chamber, electrical connections made and the alignment and gap set. All other electrical connections are made inside the chamber. The chamber is sealed and pumped down to high vacuum as described above. The high voltage pulse is then applied to the cathode by the method relavent to the experiment. The recording of the emission process on the oscilloscope is then triggered by the rising edge of the applied pulse, with 100 data points recorded before the trigger and 900 after. The vacuum chamber is then shut down and vented as describe above. Any adjustements within the chamber are then made and the process repeated. Figure 3.4 shows the experimental set up inside the chamber. Note the cathode, Faraday cup, precision stage and H-shaped mounting frame.

3.2.1 System Component Details

Details of each part of the system are given in the following paragraphs.

3.2.1.1 Oscilloscope

The oscilloscope is an Agilent Technologies MSO6104 model. It was chosen due to its high sampling rate (up to 4GHz, i.e. 1 sample every 25 ps, four inputs as opposed to the two seen on many models, and its 1000 sample recording capability. The oscilloscope was typically used to record over a few μs. Triggering was performed using the oscilloscope's built in trigger feature, where a rising or falling edge of the applied pulse above a selected voltage would trigger the recording process.

3.2.1.2 Pulse Generator

The pulse generator was a GBS Electronik RUP-3a device. This device is capable of producing positive pulses of up to 25 kV. A schematic of the pulse generator circuit is shown in Fig. 5 of Appendix 2. This device uses an active turn off feature, where the device can ground the load at the end of the pulse.

3.2.1.3 Signal Generator

The pulse generator is controlled by a signal genertor, which provides a 5 V square wave signal. The pulse gnerator applies a voltage to the load while the control signal from this signal genertor is at 5 V, and grounds it at 0 V. The length of the pulse is controlled by the length of the signal genertor pulse. The voltage of the pulse is controlled by a potentiometer on the front panel of the pulse genertor. A rough value of the pulse voltage is given by a dial on the front panel of the device. Accurate readings of both pulse voltage an current are provided by monitoring BNC terminals on the front panel of the device, which are connected to the oscilloscope.

3.2.1.4 External Pulse System

Figure 3.1 shows the entire system as used in the external pulse application procedure. The oscilloscope used for monitoring, the signal generator used for controlling the HV pulse generator, the HV pulse generator, the vacuum chamber and the vacuum control system are shown. Note the physical size of the system, which is a common drawback of such ferroelectric electron emission systems.

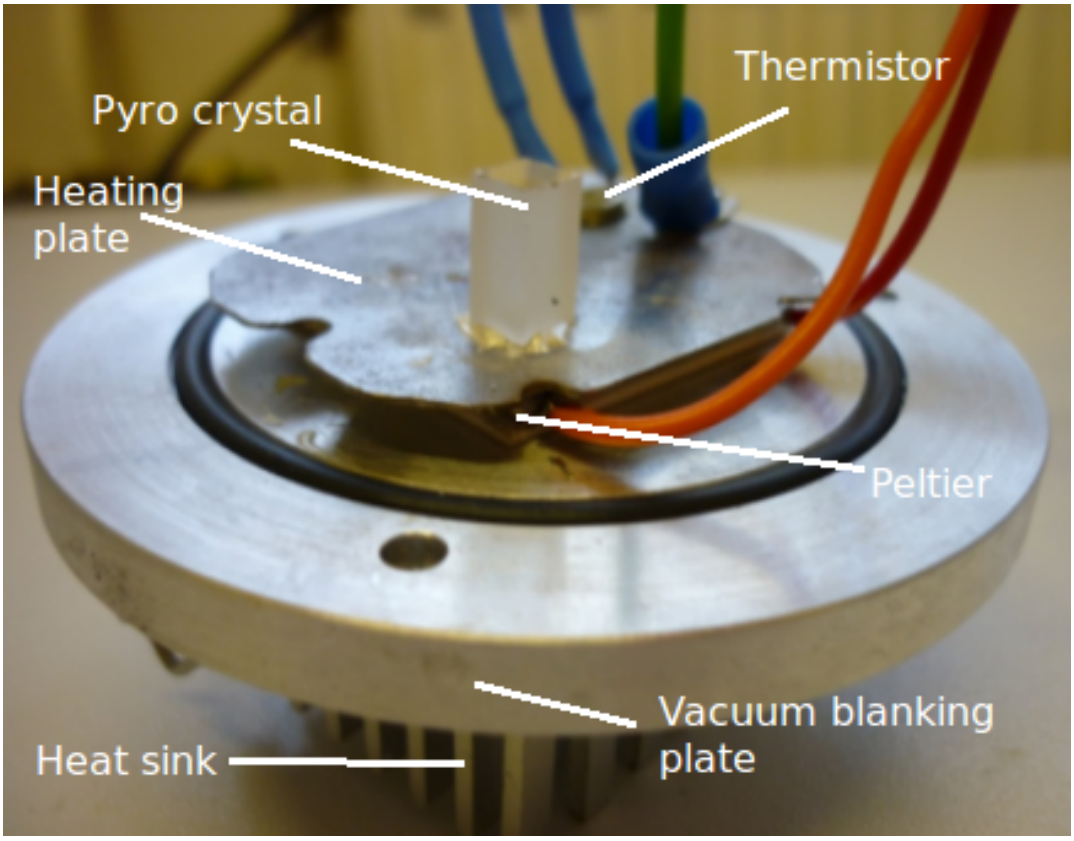

Figure 3.2: Photograph of the Peltier element heating system on the vacuum blanking plate. The themistor, heating plate and $LiTaO_3$pyro crystal are also shown.

3.2.1.5 Peltier Heater

Figure 3.2 shows the pyroelectric pulse generation system used to perform the function of the HV pulse generator. The vacuum blanking plate shown is 76.2 mm in ⌀, as compared to the very large HV pulse generator. The pyroelectric crystal was heated by the Peltier element. The Peltier element is powered by a commercially sourced Peltier controller, with a PC interface. Temperature data is provided by a bead thermistor, again interfaced with the PC via the Peltier controller. This allows accurate temperature control of the pyroelectric crystal.

3.2.1.6 Faraday Cup

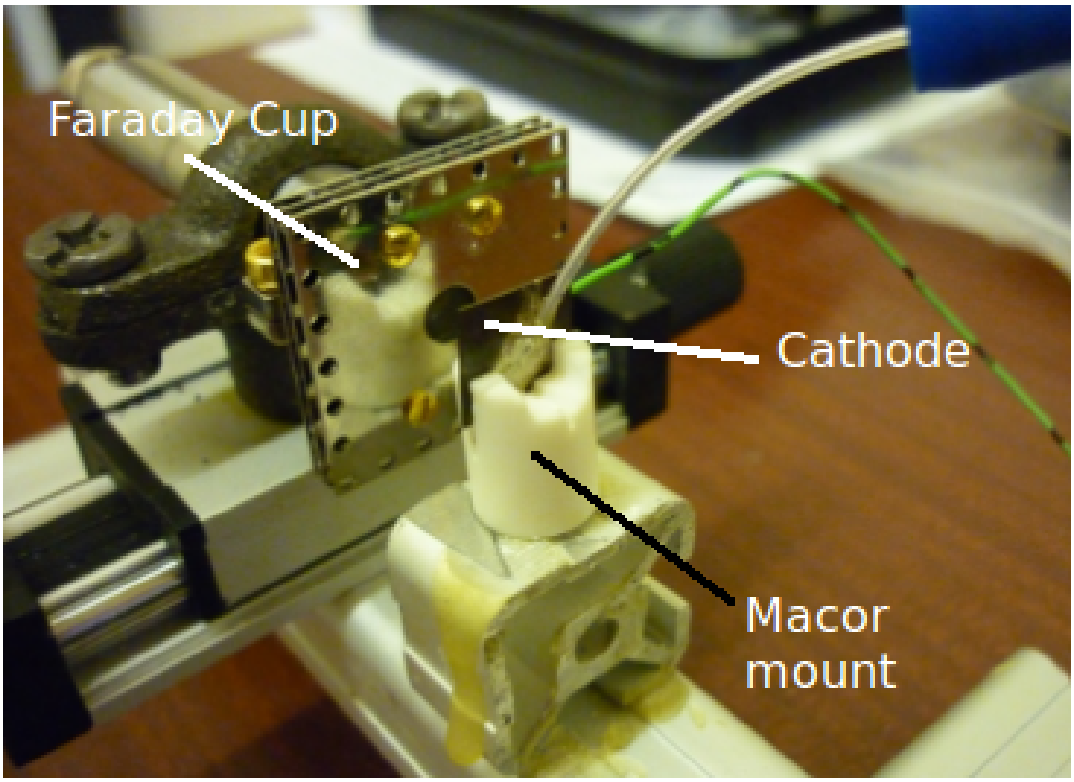

Figure 3.3: Photograph showing the Faraday cup and a ferroelectric cathode in their mounts.

Emitted charges were detected using a Faraday cup (Kimball Physics model FC-71). The Faraday cup used has a 5 mm diameter aperture. The Faraday cup was mounted in a bracket, on a precision stage. The precision stage allowed accurate alignment of the aperture with the front electrode of the ferroelectric cathode. Figure 3.3 shows the Faraday cup in its mount, and the ferroelectric cathode in its Macor holder.

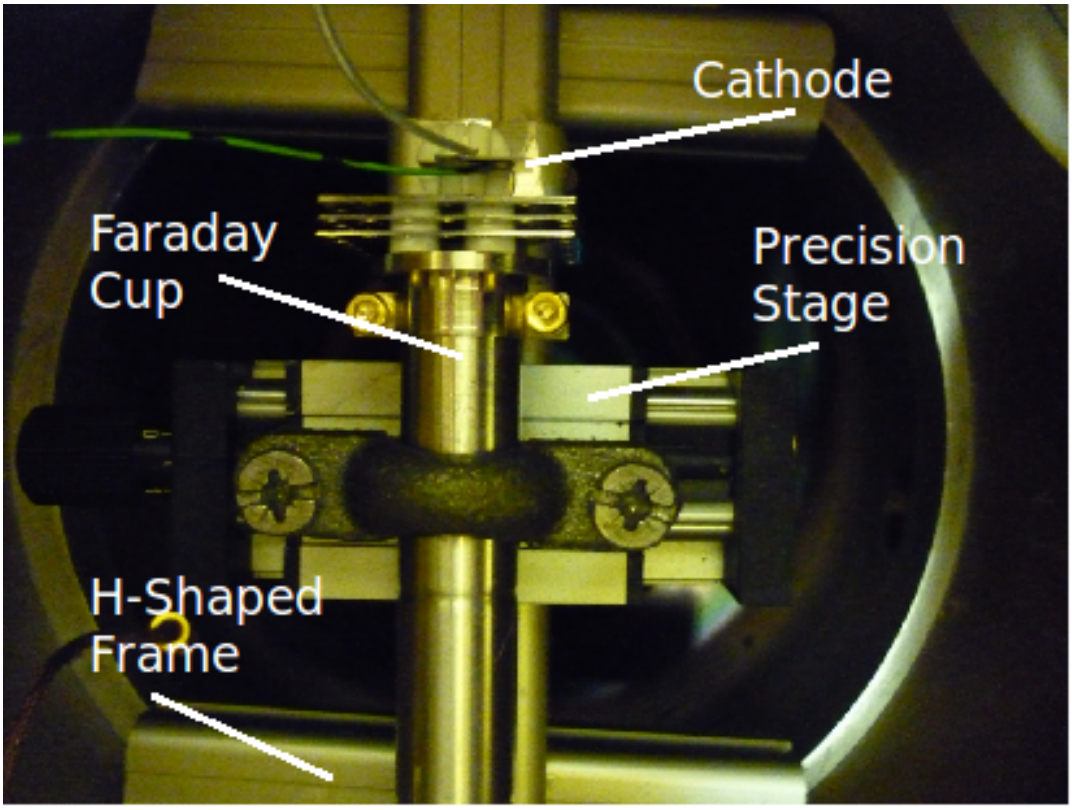

Figure 3.4: Photograph of the cathode and Faraday cup mounted in the vacuum chamber in the external pulse system configuration.

3.3 System Construction

The initial task for this project was to construct a suitable system. The total system can be broken down into a few subsystems:

- Vacuum System
- Pulsing System
- Measurement System

The construction and operation of these subsystems is described below.

3.3.1 Vacuum System

It is necessary to conduct the ferroelectric electron emission experiments under high vacuum, since atmospheric molecules will prevent the flow of electrons. The improved electrical insulation and greater breakdown voltage of high vacuum compared to atmospheric pressure air is also of considerable use in this application. It was therefore necessary to construct a high vacuum system.

The basis for the high vacuum system was an aluminium walled ion milling machine chamber. The chamber was equipped with several ports of 50.8 mm and 72.6 mm ⌀. Custom blanking plates were constructed for these ports using 6 mm thick aluminium. These blanking plates were manufactured by the university workshop. An Edwards rough pump was used for roughing the chamber, while a Leybold turbomolecular pump was used to achieve high vacuum. A Leybold Turbotronic NT20 controller was used to control both the rough pump and the high vacuum pump. Pressure monitoring was via a Pirani gauge from atmosphere to 10^{-2} torr, and a penning gauge was used below 10^{-2} torr.

This system had several requirements:

- Must achieve high vacuum (at least 10^{-4} torr)
- Multiple electrical feedthroughs needed
- Several high voltage feedthroughs needed
- Internal heating/cooling system
- Large enough to house all systems

3.3.2 Pulsing System

A system was designed and constructed to apply a high voltage to a custom made ferroelectric cathode. This system comprised a high voltage pulse generator (GBS Electronik RUP3-25a) capable of producing pulses of 0 V to +25 kV, with arbitrarily variable pulse length. This pulse generator included a current and a voltage monitor output for connection to an oscilloscope. The oscilloscope used was an Agilent MSO 6104a model. An arbitrary function generator was used to provide the 5 V TTL (Transistor-Transistor Logic) signal to trigger the high voltage pulse generator. The ferroelectric cathodes were manufactured as previously described. A high voltage feedthrough was manufactured from a automotive spark plug. A thick steel wire was bonded to the tip of the spark plug using electrically conductive epoxy. A hole was drilled through a 10 mm ⌀, 15 mm long rod of Macor ceramic, which was then placed over the tip of the plug and wire, to improve the insulation of the system. A blanking plate was tapped to the appropriate M8-1.5 thread. The spark plug was then screwed into the blanking plate, and tightened down so as to compress the metal crush washer into the blanking plate. This provided a vacuum tight seal. Screw cap plugs were selected as this increases the inherent safety of the system. A schematic of this system is shown in Fig. 3.1.

3.3.3 Measurement System

3.3.3.1 Within the Vacuum Chamber

The current emitted by the ferroelectric cathode was measured by a Kimball Physics FC-71 Faraday Cup (FC), which was fitted with a 5 mm ⌀aperture. The FC was mounted to a precision stage via a clamp. The precision stage allowed

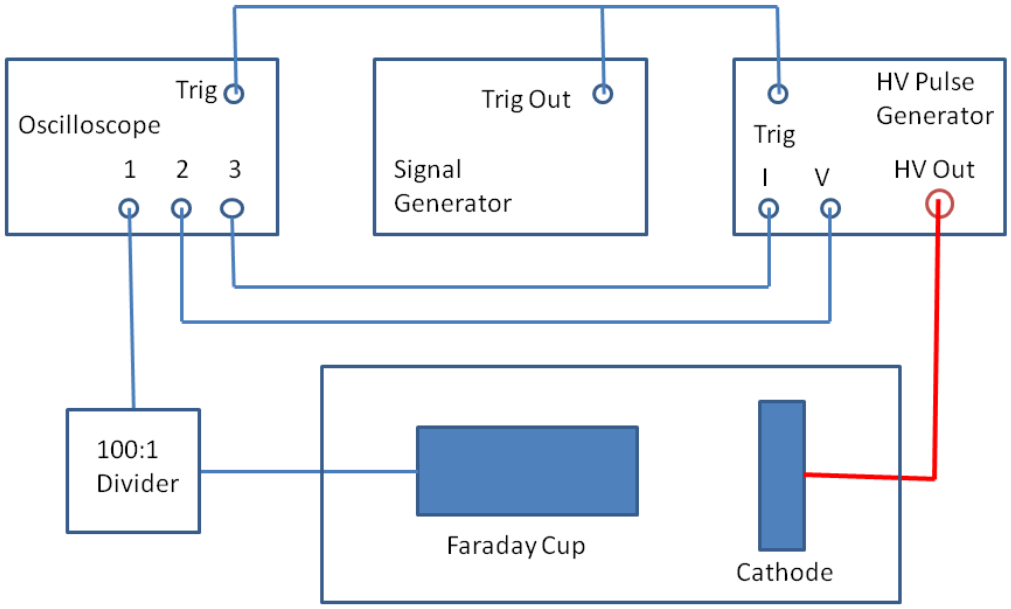

Figure 3.5: External pulse generator FEE system

the FC to be moved left and right with respect to the ferroelectric cathode, which allowed precise alignment of the two components. The FC/precision stage arrangement was mounted to an 'H' shaped frame constructed from 20 mm box section aluminium. This allowed the system to be mounted in the vacuum chamber. Electrical connection to the FC was made using RG-59 coaxial cable both within and outside the vacuum chamber. A schematic of the system is shown in Fig. 3.5.

3.3.3.2 Outside the Vacuum Chamber

The signal from the FC was fed into a coaxial box which contained a 100:1 voltage divider, comprised of 4.7 kΩ and 52 Ω resistors. The 4.7 kΩ resistor was a high powered model, which served the purpose of reducing the voltage generated across the 52 Ω resistor to a suitable level for the oscilloscope. The current was calculated by measuring the voltage generated across the 50 Ω

resistor, and using Ohm's Law $I = \frac{V}{R}$, where V is the measured voltage, R is the resistance and I is the current. The emitted charge is calculated using the oscilloscopes 'integrate' function to integrate the current trace with respect to time, since:

$$Q = \int I dt$$

where Q is the emitted charge and I is the current. This data was then saved for later analysis. Numerical integration of the current trace using both Microsoft Excel (in conjunction with a macro) and QtiPlot were found to be equivalent to the oscilloscope integration, and were used in some cases.

3.4 Ferroelectric Cathodes

The ferroelectric cathodes were manufactured using PZ34 supplied by Ferroperm. The samples were of dimensions 10 mm $\times$10 mm $\times$400 μm. The samples had conductive electrodes on each large face. To prepare these samples for use as ferroelectric cathodes the electrode was removed on one face entirely, and partially on the other. The electrodes were removed by manually abrading the surface with fine (4000 grit) abrasive paper. The electrode was partially removed from the other face to help prevent electrical arcing between the front and rear electrodes. The electrode-free face was used to mount the grid electrode. A transmission electron microscope (TEM) sample support grid was then bonded to the center of the PZ sample using a small amount of conductive epoxy. The samples were then place in a glassware drying oven at $\sim$ 60°C to cure the

epoxy. Various grid densities (i.e. number of bars/cells per unit area) were used, ranging from a ring with no bars to 200 bars per inch. All TEM grids were of the 3.05 mm ⌀ type, and were made of copper. Once the conductive epoxy was cured, a fine wire was bonded to the edge of the TEM grid, and the sample again cured in the oven. Finally, a wire was bonded to the rear electrode and the sample cured in the drying oven again. A microscope image of a 100 mesh electrode is shown in Fig 3.6, while an example of a completed cathode is shown in Fig. 3.7.

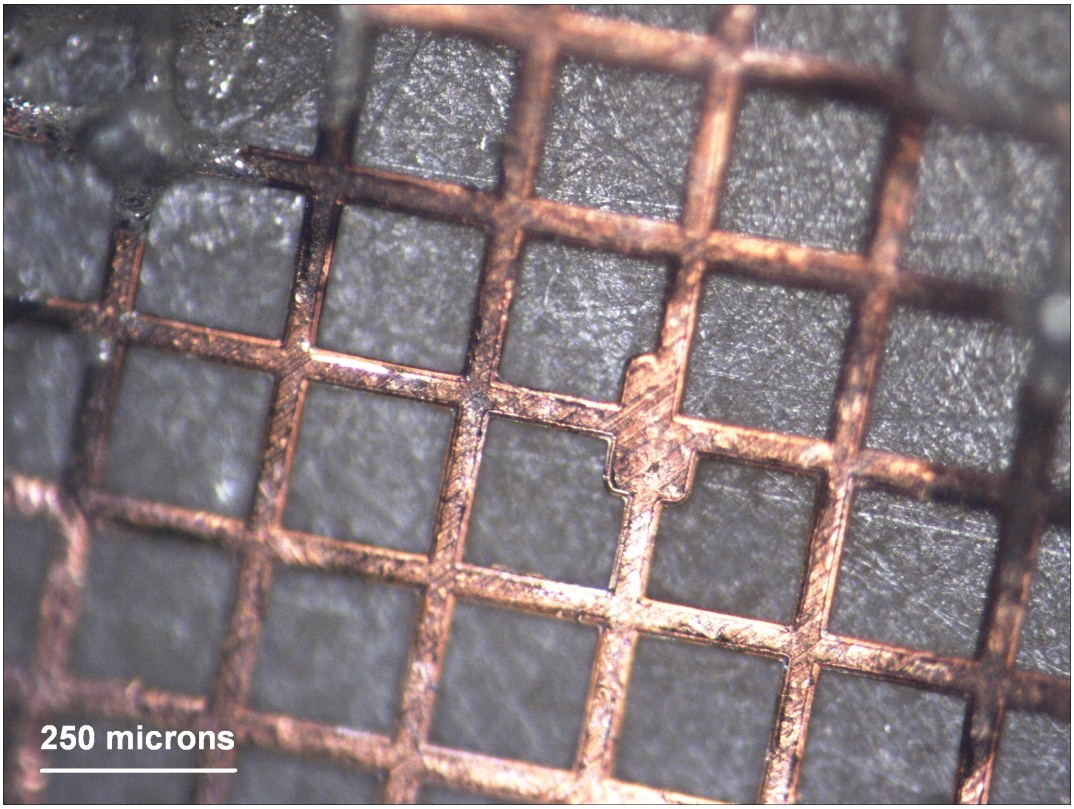

Figure 3.6: A PZ cathode with a 100 mesh electrode at 10× magnification. The scale bar shows 250 μm.

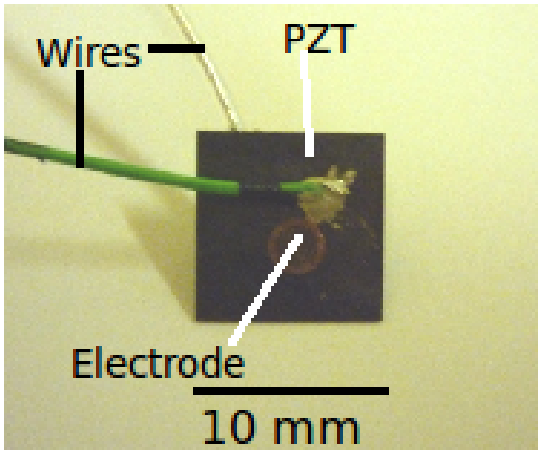

Figure 3.7: Photograph of a ferroelectric cathode of the type used in this project.

3.5 System Operation

The system was operated by first placing the ferroelectric cathode in the Macor holder, and making electrical connections to the HV feedthrough and ground. The vacuum chamber is then sealed and pumped down to high vacuum. The HV pulse parameters were then defined using the function generator to set the pulse width, and the HV pulse generator to set the pulse voltage. The minimum pulse width that allows sufficient time for the pulse to rise to it's full value is ~ 1.5 μs. The oscilloscope trigger is set to trigger on a positive going edge on the channel monitoring the HV pulse voltage. Appropriate voltage and current settings are chosen for each channel, and the voltage and current monitor channels are set to the correct attenuation: 1000:1 for the voltage monitor and 10 V:1 A for the current monitor. The oscilloscope time base is then set to 5μ s / div, and the timebase centred to the left. The oscilloscope channels are paired: 1 and 2; 3 and 4. This pairing results in a drop from a maximum sample rate of 4 GS/s to 2 GS/s when both channels in a pair are used. For this reason the current and voltage monitors are both connected to one pair, while the emission current system is connected to a single channel of the other pair. This allows the emission current to be recorded at the maximum horizontal resolution. The

oscilloscope inputs were set to 1 mω input impedance, and bandwidth limiting activated on all active channels. This reduced noise in the signals. The system is then fired using the function generator to trigger the pulse generator. This in turn triggers the oscilloscope, which records traces of applied current, applied voltage and emission current over 5μ s. The HV pulse was always applied to the rear of the ferroelectric cathode, and is always positive.

3.5.1 Temperature Control System

3.5.1.1 Electrical

The temperature control system comprised several sections: the heating/cooling element, temperature monitoring and power supply. A 37 W Peltier element (Global Component Sourcing model ET-127-10-13-RS) was used as the heating/cooling element since it is one of the few devices capable of both heating and cooling, is easily controlled, and is compatible with high vacuum. A Supercool PR-59 Peltier controller module was used to provide power to the Peltier element, and also to process temperature information from the element. A suitable 15 V power supply (Traco Power model TXL 100-0533TI) was used to power the controller module. The controller and power supply were mounted in a 19 inch racking box to prevent electrical hazards. Temperature monitoring was conducted using a 10 kΩ bead thermistor.

3.5.1.2 Peltier Element

A Peltier element was chosen as the temperature control device as it allows both heating and cooling of the sample while under vacuum. A typical resistance

heating device does not have this capability, which may reduce the speed at which the system may be thermally cycled. The device chosen was a 37 W device capable of a maximum operation temperature of 80°C , and a maximum temperature differential between sides of 74°C . The "hot" side (i.e. the side with the electrical connections) of the Peltier was bonded to the blanking plate. This was done since a small amount of ohmic heating would be present due to the current flow, and the large heat sink bonded to the outside of the chamber would greatly reduce its affect.

3.5.1.3 Crystal Mounting

The Peltier element was mounted to a 76.2 mm ⌀, 6 mm thick vacuum blanking plate. A small section of thermally conductive, double sided adhesive sheet was cut to size for this purpose. On the external side of the blanking plate, a large heatsink was bonded to the surface in a similar manner. This heatsink is intended to hold one side of the Peltier element at an approximately constant temperature. A 2 mm thick section of aluminium was cut to the size of the Peltier element, and bonded to it with the thermally conductive sheet. This plate was used to ensure even heat distribution of heat across the Peltier element, and to provide a heat reservior for the $LiTaO_3$ to be heated. This aluminium plate will be referred to from now as the hot plate. The hot plate was connected to electrical ground via a wire connected to the chamber wall. The $LiTaO_3$ crystal was then bonded to the surface of the hot plate using Circuitworks silver epoxy, which is both electrically and thermally conductive. This allowed to side of the crystal connected to the hotplate to be held at ground potential. A thin wire was bonded to the exposed surface of the $LiTaO_3$ using the conductive epoxy.

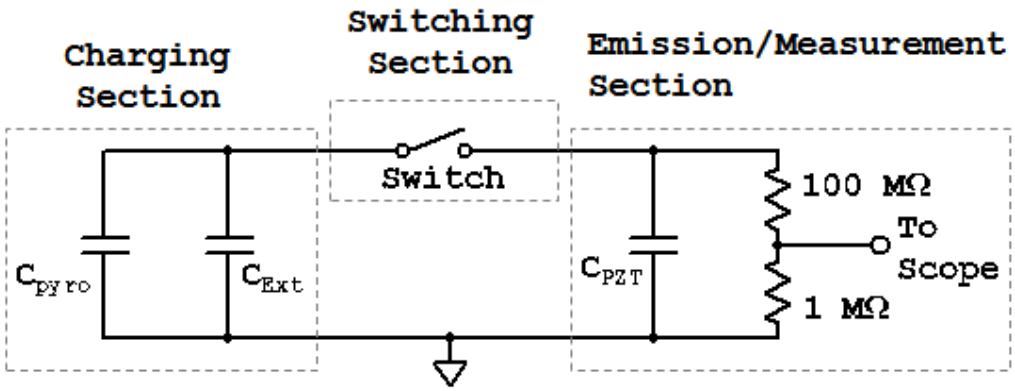

Figure 3.8: Schematic of the pulsing circuit, highlighting each section

3.5.2 Pulse Generation Circuit

The pulse generation circuit was constructed on electrical stripboard. This allowed quick and easy manufacture, as well as easy modification. The circuit comprised three main sections: the charging section, the switch and the measurement section. A schematic of this circuit is shown in Fig. 3.8.

3.5.2.1 Charging Section

The charging section of the pulse generation circuit was comprised of a capacitance in the range 50 - 120 pF. High voltage capacitors were used for this application.

3.5.2.2 Measurement Section

The measurement section of the pulse generation circuit comprised a load capacitor, C_{PZT}, and a 100:1 high voltage divider. The load capacitance was used to provide a load to the pulse that would be similar to the ferroelectric cathode when emission was not occuring, i.e. when it behaves as a capacitor. The high voltage divider allowed the voltage present across the capacitor to be measured using the oscilloscope.

3.5.2.3 Switching Device

The switching device is the most important part of the pulse generation circuit, with strict demands placed upon it by the intended application. The requirements and potential devices are discussed below.

3.5.2.3.1 Switching Requirements The switching device has several stringent requirements placed on it by the rest of the system, several of which are listed below:

- Very high off-state resistance

  The resistance of the device must be very high due to the low charge produced by the pyroelectric material during heating. An off-state resistance of $\sim 1{\times}10^{13}$ will results in a sufficiently high time constant for the system.

- Physical size

  The device must be very small so as to avoid dominating the size of the overall device.

- Vacuum compatibility

  The device should ideally be compatible with high vacuum, as this will simplify construction of the device.

- High voltage capability

  Since the voltages involved in this system will be on the order of several thousand volts the device must be suitable for this.

- Fast switching

  The literature shows that optimum emission from a ferroelectric cathode is achieved with a very fast (tens of ns) rise time pulse.

3.5.2.3.2 Possible Switches Several devices were considered for use as the pulsing system switch. Broadly, these devices can be categorised as either semiconductor devices or solid state devices. These two groups of devices will be discussed separately, as there were several issues common to the members of each group. Several semiconductor devices were considered:

- High voltage transistor
- Insulated Gate Bipolar Transistor (IGBT)
- Thyristor
- Metal oxide varistor
- Avalanche diode
- Optocoulper

While all of these devices had many attractive qualities, such as vacuum compatibility, and the ability to be electrically/optically triggered, the off state leakage current was always vastly in excess of acceptable levels. As a result, all of these devices were dismissed as candidates for the switching device.

Solid state devices considered:

- Reed relay
- Electromechanical relay
- Spark gap
- Miniature spark gap

Consideration of these devices gave a wider range of issues than was experienced for the semiconductor devices, hence each device will be discussed individually. The reed relay, while having the advantage of being manually triggerable had several disadvantages. The devices were relatively large, and had a relatively slow switching time of a few μs. The electromechanical relay shared many of the problems of the reed relay, but has the additional issues of having much lower off-state resistance. Spark gaps were considered, and found to be good candidates in terms of electrical performance. however, mechanical considerations highlighted issues with the device: the spark gaps were physically quite large, and are frequently made of glass. This rendered them unsuitable for vacuum use. This led to the consideration of the miniature spark gap; a smaller, lower voltage version of the regular spark gap, with a metal and ceramic construction. These devices are physically small, typically less than 1 mm^3. They also operate in the range of tens of volts to several thousand volts, have high current capabilities and are highly reliable. Testing showed that these devices are able to switch high voltages with rise times of a few tens of ns. These considerations led to the choice of the miniature spark gap as the switching device. The spark gap device selected was a Littelfuse CG3 model, with a DC breakdown voltage of 1.5 kV.

3.6 Chapter 5

In chapter 5 the basic elements of the pyroelectric pulse system and ferroelectric emission system are studied. Several seperate experiments are performed for this purpose. Firstly, the external high voltage pulse generator is used to apply a positive high voltage pulse to the rear electrode of a ferroelectric cathode. The cathode is held under high vacuum, and emitted electrons and ions are

collected in a Faraday cup. This allowed confirmation that the ferroelectric cathodes operated correctly.

The pulsing circuit was then used in conjunction with a $LiTaO_3$ crystal to produce a high voltage pulsing system. This system was operated under high vacuum. The Peltier element was used to heat the $LiTaO_3$. Heating and temperature monitoring of the Peltier was performed using the temperature controller module and manufacturer provided software. The charged capacitor of the pulsing circuit was then switch by a spark gap switch, which applied a voltage pulse to a load capacitor. The voltage on this load capacitor was measured across a voltage divider, and recorded by the oscilloscope.

The ferroelectric cathode and pyroelectric pulsing system of the above sections were then combined so as to use the pulse from the pyroelectric pulsing system to drive the ferroelectric cathode. Various parameters were investigated in this section of the experiments. Positive or negative voltage pulses from the pyroelectric pulsing circuit were applied to either the front or rear electrode of the ferroelectric cathode, and several grid structures for the front electrode were tested. Several different values of the external capacitor of the pulsing circuit were also used to investigate their effect.

3.7 Chapter 6

The pulsing/cathode system was the same as previously used. A new anode/measurement system was used. This system used an anode mounted to a precision table to allow the distance between the anode and cathode to be adjusted. This anode was connected to a GBS Electronik RUP-3A high voltage pulse generator. This pulse generator was used as both the supply for a DC

acceleration voltage and as the measurement system. The actual measurement element was a current sensing coil contained within the pulse generator, which was calibrated by the manufacturer. A schematic of the external pulse generator circuit is shown in Fig. 5 of Appendix 2. A schematic of the pulsing, emission and acceleration system is shown in Fig. 3.9. Unless otherwise stated a 12.5 mm diameter anode is used, and is placed 10 mm from the cathode.

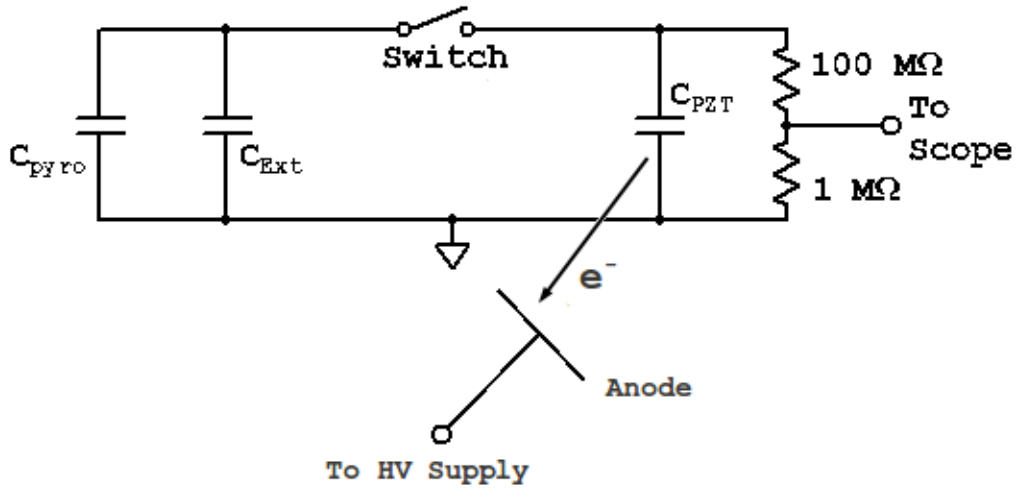

Figure 3.9: Schematic of acceleration circuit

3.8 Chapter 7

The experimental set up for this series of experiments uses a modifed version of the system used in the previous chapter. The pulse/FEE circuit remained the same as previously, but the acceleration system was changed. Instead of the external pulse generator being used as the acceleration and current/charge measurement system a custom circuit was designed. This circuit comprised

a capacitive divider connected in parallel with a $LiTaO_3$ single crystal of dimensions 5x5x10 mm^3. The spontaneous polarisation vector was aligned with the 10 mm direction. The $LiTaO_3$ crystal was orientated such that heating it would produce a positive voltage on the capacitive divider. An anode was connected to this circuit such that the voltage on the top surface of the $LiTaO_3$ would be applied to it. To heat the $LiTaO_3$ a heating plate based on a Peltier element was constructed within the vacuum chamber. The Peltier was bonded to a blanking plate on one side and an aluminum plate on the other. A heat sink was bonded to the other side of the blaking plate, outside of the vacuum chamber. This maintained one side of the Peltier at close to room temperature. The other side of the Peltier was bonded to the aluminium plate using conductive epoxy. The aluminium plate, and therefore one side of the $LiTaO_3$ was electrically grounded. A thermistor was used for temperature monitoring, via the Supercool PR-59 temperature controller circuit. In all experiments a 12.5 mm diameter anode was used and was placed 10 mm from the cathode.

3.8.1 Accleration Voltage Measurment

To determine the voltage on the acceleration system a voltage follower circuit was used in conjunction with the capacitive divider of the acceleration system. The voltage follower was needed due to the very small amount of charge involved in the system. A schematic of the system is shown in Fig 3.10

3.8.2 Charge Measurment

To measure the charge collected by the acceleration system the voltage follower could not be used since it did not have a sufficient slew rate, which led to signif-

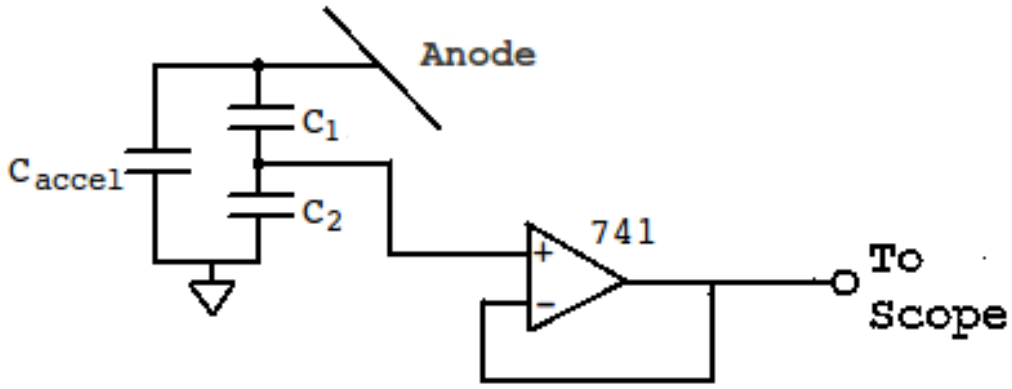

Figure 3.10: Acceleration voltage V_{acc} measurment system for the pyro acceleration system. is the accelerating pyroelectric element.

icant signal distortion. The output of the capacitive divider of the acceleration system was instead monitored by the oscilloscope via a probe. A schematic of the system is shown in Fig 3.11.

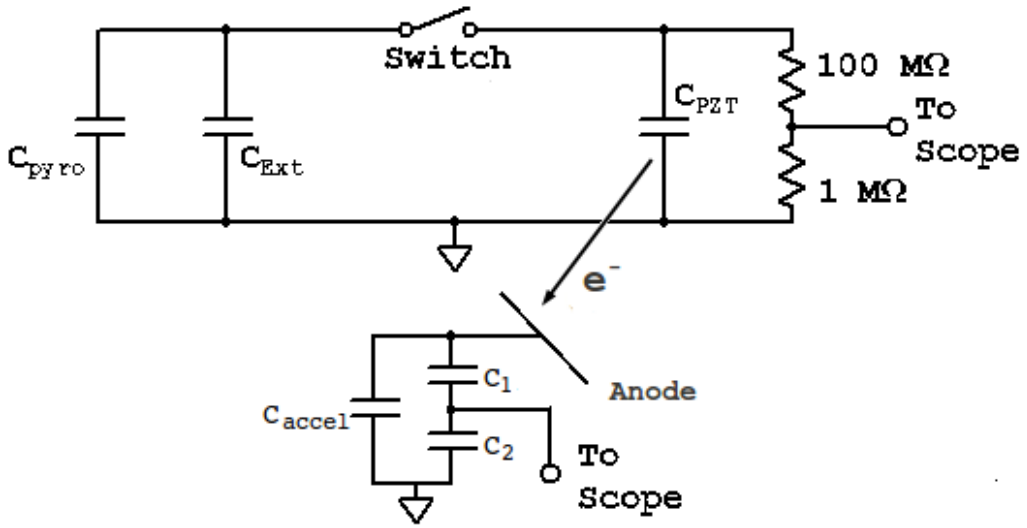

Figure 3.11: Pulsing, acceleration and measurment system schematic for the pyroelectric electron accelration system. is the acceleration pyroelectric element.

Chapter 4

Open Circuit Pyroelectric Coefficient

This section of the project looked at the effect of the open circuit condition on the pyroelectric coefficient of various bare and composite PZT samples. Previous work on the subject of enhancement of the pyroelectric coefficient has suggested that there may be a difference in the open and short circuit pyroelectric coefficients [9, 37, 38]. Work on using the secondary pyroelectric effect (as defined in Eq. 2.1 has been conducted [41, 42], which has shown the techniques potential. This is significant to this project since the pyroelectric elements in the system are in the open circuit condition, while the pyroelectric coeffients are given in literature under the short circuit condition. The use of laminar composites of PZT and stainless steel were also investigated since this has previously been shown to increase the pyroelectric coefficient of pyroelectirc materials under the SC condition. To understand the reasoning behind the difference in coefficients at open and short circuits Eq. 4.1 must be considered. This equation describes the total pyroelectric coefficient ($P_m^{T,E}$) in terms of its component parts: the

primary ($P_m^{S,E}$) and secondary ($d_{mkl}^{E,\Theta} c_{ijkl}^{E,\Theta} \alpha_{ij}^{T,E}$) pyroelectric coefficients. Within the term for the secondary coefficient $d_{mkl}^{E,\Theta}$ is the piezoelectric constant, $\alpha_{ij}^{T,E}$ is the thermal expansion coefficient and $c_{ijkl}^{E,\Theta}$ the stiffness constants. The primary coefficient simply describes the 'true' pyroelectric response as described in Eq. 4.1[10]. The secondary coefficient is a more complex concept. It describes the 'apparent' pyroelectric response of a material due to its thermal expansion generating a piezoelectric response. Equation 4.1 shows that a variation in any of the components relating to the secondary components between open and short circuit condition will result in change in the total coefficient.

$$P_m^{T,E} = P_m^{S,E} + d_{mkl}^{E,\Theta} c_{ijkl}^{E,\Theta} \alpha_{ij}^{T,E} \tag{4.1}$$

4.1 Open and Short Circuit Measurement

This series of experiments required measurement systems able to approximate open and short circuit conditions while measuring either the charge or voltage generated by a heated pyroelectric material. Two systems with different approaches where used for this. The present system used a high input impedance operational amplifier operating as a voltage follower. Simply connecting the pyroelectric material to the op amp input provides an approximation of open circuit. To approximate short circuit a large capacitor was connected in parallel to the sample, reducing the voltage across it to almost zero. The pyro rig system used a similar apprach for open circuit measurments, using an electrometer operating in voltage mode in place of the op amp of the present system. The short circuit measurement differed however. The electrometer was operated in current mode, thus measuring the current produced by the pyroelectric material during heating. Integrating this data over time gave the charge produced.

4.2 PZT Samples

Two main sample types were used in this section of the project: bare PZT samples, and composite stainless steel/PZT/stainless steel samples. These two sample types were used so a comparison could be made.

4.2.1 Bare PZT Samples

Two types of PZT were used in this series of experiments; PZT-5A and PZT-5H, both supplied by Piezo Systems Inc.

4.2.2 Laminar Composite PZT Samples

The composite samples were constructed from thin bulk of PZT-5H sandwiched between two sheets of stainless steel (SS). This symmetrical structure was used to prevent bending of the PZT samples, leading to undesired piezoelectric effects. The structure was then bonded together using epoxy. A schematic of the structure of the composite samples is shown in Fig. 4.1. Using PZT of thickness 127 μm, 191 μm and 267 μm, and SS of thickness 50 μm, 125 μm and 250 μm allowed a variety of laminar composite samples to be produced with a range of thickness ratios (R) of PZT to steel from 0.385 to 2.67. The thickness ratio is defined in Eq. 4.2.

$$Thickness\ Ratio = \frac{Thickness\ of\ PZT}{Total\ thickness\ of\ stainless\ steel} \tag{4.2}$$

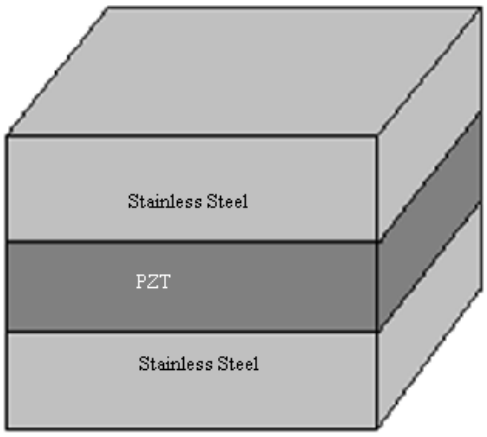

Figure 4.1: Composite structure sample

4.3 Measurement System

4.3.1 System Construction

A vacuum system composed of a turbomolecular pump backed by a mechanical rough pump was used to achieve a vacuum of around 10^{-5} torr. A heating system was constructed in the vacuum chamber by bonding a Peltier element to a 76.2 mm $\varnothing$, 6 mm thick aluminium blanking plate. The "cold" side of the Peltier was bonded to the blanking plate to improve temperature regulation of the system. An aluminium plate was bonded to the 'hot' side of the Peltier to act as a heating plate for the system. This plate was grounded. A thermistor was bonded to the surface of the aluminium plate to monitor the system temperature. A bracket was contructed to hold a wire just above the aluminium plate so that electrical connection could be made to the measurement system. The electrical measurement system was contructed from a custom voltage folllower circuit. A very high input impedance 741 op-amp was used, with a rated input impedance of at least 1.5 $T\Omega$. This was necessary to prevent charge leakage in the system. The input of the voltage follower circuit was connected to the pyroelectric sample. Two variations of this circuit were used to approximate the open and short

circuit conditions. These equivalent circuits are shown schematically in Fig. 4.2. For open circuit measurements only the sample was connected to the voltage follower, which approximates the open circuit condition. To make the short cirucit measurement a capacitor was connected in parallel to the sample. This capacitor had a capacitance several hundred times that of the sample (3.59 μF for the capacitor compared to $\sim 10\ nF$ for the sample). Thus most of the charge generated by heating would leave the sample and be stored on the capacitor, giving a close approximation of the short circuit condition. The output of the voltage follower was monitored by an Agilent MSO6104A oscilloscope. Plots of voltage vs temperature were produced and used to calculate the pyroelectric coefficient.

4.3.2 System Validation

To confirm correct operation of the system a series of experiments were conducted to validate the present system against an existing system. This existing system will be refered to as the 'pyro rig' from here on. The pyro rig operated in a similar way to the present system in terms of the heating system: a heater is attached to a copper block on which the sample sits, and the sample is electrically connected to the measurement system by a wire from above. An electrometer was used as the measurement device in the pyro rig system. The electrometer was used in 'voltage mode' for open circuit measurment and 'current mode' for short circuit measurements. Voltage mode is electrically similar to the open circuit system of the present system and uses a voltage follower circuit. Current mode operates in a different way to the short circuit mode of the present system, and acts as an ammeter measuring the current produced by the sample as it is heated. The pyro rig has been used at the university for over ten years and is known to give credible results. A major difference between the pyro rig and present systems is

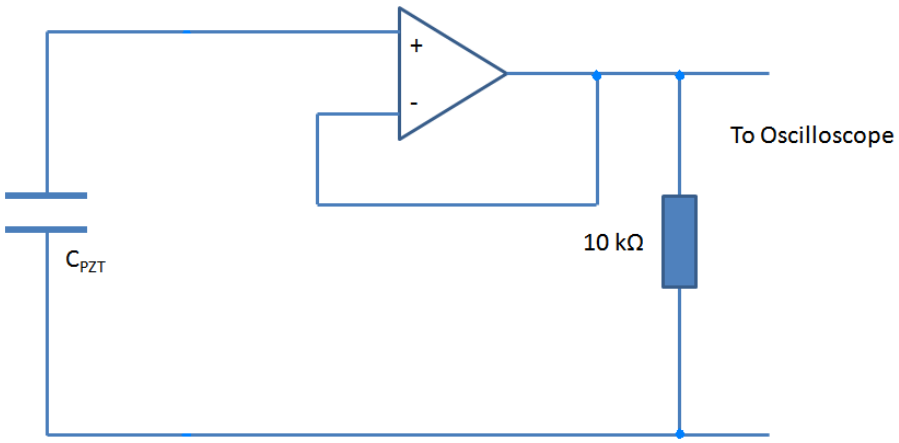

(a) Open Circuit

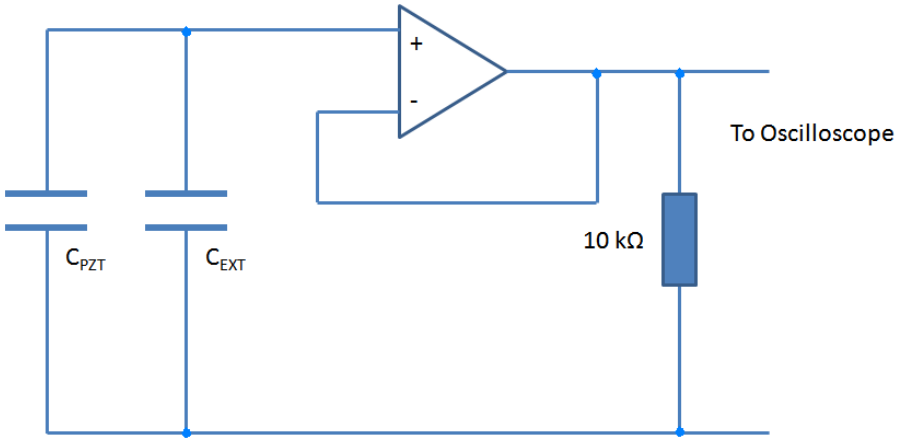

(b) Short Circuit

Figure 4.2: Schematic of the equivalent circuits (a) open circuit and (b) short circuit

the ability of the present system to achieve vacuum as low as 10^{-5} torr, while the pyro rig can achieve only around 10^{-1} torr.

4.4 Method

4.4.1 Present System

The experiments were conducted in the following way: a pyroelectric sample was place on the heating plate of system, and electrical connections made to the measurement system. The vacuum chamber was sealed and pumped down to $\sim 10^{-5}$ torr. The sample was heated to ~ 5 K above ambient temperature and allowed to slowly cool. The voltage output from the voltage follower was monitored by the oscilloscope for 50 s during the cooling. Plots of voltage vs temperature were calculated from the data and the pyroelectric coefficient produced from this.

4.4.2 Pyro Rig System

The method for the pyro rig system involved placing a pyroelectric sample on the heating plate of the system and making the electrical connections to the system. The chamber was sealed and pumped to a rough vacuum of around 10^{-1} torr. The sample was then cycled around room temperature by a few degrees, with a temperature ramp rate of 2 K per minute. In a similar way to the present system this data was used to produce plots of voltage (open circuit system) or current (short circuit system) vs time. From this the pyroelectric coefficient was determined.

4.5 Results and Discussion

Initially a validation of the system was performed to confirm proper operation of the system. The results of this validation of the present system against the pyro rig are shown in Table 4.1. These results show a general similarity between the present system and the pyro rig for both open and short circuit conditions. However, the present system measurments are larger than the pyro rig measurments for all samples at OC and SC. This is shown best by the relative difference column in table 4.1. The relative percentage differences between the present system and the pyro rig are shown to be significantly different at open and short circuit condition. At OC condition the average relative difference is 27.4% while at SC it is 16.7%. These results can be explained as the result of two factors: differences in the systems, and charge leakage due to the differing vacuum systems. A difference between the two systems due to systematic differences is expected since there are differences in the temperature measurement systems, i.e the thermistor is bonded to the top of the hotplate in the present system while it is in the middle of the hotplate in the pyro rig. The differing vacuum conditions of the two systems would also be expected to make a difference; the higher vacuum of the present system will greatly reduce any charge leakage in the measurement process, while such charge leakage cannot be neglected in the pyro rig system. It is also reasonable to assume that charge leakage in the pyro-rig will be more significant at OC condition than in the SC condition. These considerations explain why there is a difference between the two systems, and also why the difference between the two systems is greater at OC than SC. Since the average relative difference at SC is 16.7% and 27.4% at OC it can be assumed that the 16.7% difference is due to system differences and a further $27.4\% - 16.7\% = 10.7\%$ is due to the greater charge leakage in the pyro rig system.

An experiment was carried out to confirm that charge leakage was negligible in the present system by heating a sample a few degrees and holding it there for several minutes. During this time no change in the output of the voltage follower was detected. However, for the pyro-rig system an apparent voltage drop with time was observed when holding the sample at a constant temperature. It was this consideration, i.e that the pyro-rig could not properly approximate the open circuit condition due to charge leakage, that made the present system necessary.

Table 4.1: Comparison of the pyroelectric coefficient measurement results from the present system in the high vacuum and the pyro rig in low vacuum systems for a few stainless steel/PZT laminar composite samples under open and short circuit condition. The present system, pyro-rig, relative difference and absolute difference are shown. The unit of the pyroelectric coefficient is $10^{-4}Cm^{-2}K^{-1}$.

, and is used for all values except relative difference.

	OC				SC			
Thickness Ratio	Present System	Pyro-Rig	Rel. Diff. / %	Abs. Diff.	Present System	Pyro-Rig	Rel. Diff. / %	Abs. Diff.
2.67	-6.22	-4.31	30.8	1.91	-7.17	-6.29	12.3	0.81
1.068	-8.57	-5.91	31.1	2.66	-9.68	-8.05	16.9	1.63
0.543	-8.12	-6.08	25.2	2.04	-9.22	-7.56	18.0	1.66
0.382	-9.04	-6.98	22.8	2.06	-10.68	-8.57	19.8	2.11
Average			27.4	2.17			16.7	1.63

Measurement results for the pyroelectric coefficient of bare PZT and PZT/SS composites are shown in table 4.2. Five samples of bare PZT-5A were tested with the present system and the pyroelectric coefficient was found to range from $-3.93 \times 10^{-4}\ Cm^{-2}K^{-1}$ to $-4.06 \times 10^{-4}\ Cm^{-2}K^{-1}$ at OC condition, while at SC condition the results range from $-4.92 \times 10^{-4}\ Cm^{-2}K^{-1}$ to $-5.44 \times 10^{-4}\ Cm^{-2}K^{-1}$. This gives average pyroelectric coefficient values of $-3.98 \times 10^{-4}\ Cm^{-2}K^{-1}$ at OC condition and $-5.12 \times 10^{-4}\ Cm^{-2}K^{-1}$ at SC condition. This shows a reduction of the pyroelectric coefficient of PZT-5A of 22.3% at OC compared to the SC value. Table 4.2 also shows the results for several thickness ratios of PZT/SS composite samples. The values of the pyroelectric coefficient are shown to increase with decreasing thickness ratio, for both OC and SC conditions. At the highest thickness ratio studied (R = 2.67) the values measured are $-7.17 \times 10^{-4}\ Cm^{-2}K^{-1}$ at SC and $-6.22 \times 10^{-4}\ Cm^{-2}K^{-1}$ at OC, giving a decrease at OC of 13.3%. At the smallest thickness ratio (R = 0.386) the SC value is $-10.68 \times 10^{-4}\ Cm^{-2}K^{-1}$, while at OC it is $-9.04 \times 10^{-4}\ Cm^{-2}K^{-1}$, a decresase of 15.4% at OC compared to SC. These results show a clear increase of pyroelectric coefficient with decreasing thickness ratio, i.e. the samples with the most SS relative to the PZT show the greatest increase in pyroelectric coefficient, and that the OC value is always less than the SC value. This is shown graphically in Fig. 4.3. Also shown is the experimentally determined value of the pyroelectric coefficient for bare PZT-5A at SC condition.

Theoretical values of the pyroelectric coefficient at OC were previously calculated by Chang and Huang [9, 37], and these are shown in Fig. 4.4. This shows a reasonable fit for the experimental and theoretical data. To obtain this theoretical value an interfacial coupling factor k is used, which takes account of strain loss at the bonding layer between the PZT and SS. A value of k = 0.8 is used in this calculation, where k = 0 means no bonding (total strain loss) and k = 1

Table 4.2: Summary of the pyroelectric coefficients of the bare PZT-5A and PZT/ stainless steel laminar composites under open and short circuit conditions, as measured by the presnent system at high vacuum and pyro-rig at rough vacuum, and their relative and absolute differences relative to short circuit values. The unit of the pyroelectric coefficient is $10^{-4}\ Cm^{-2}K^{-1}$, and is used for all values except relative difference.

	Present System				Pyro-Rig			
Sample	OC	SC	% Diff	Abs. Diff	OC	SC	% Diff	Abs. Diff
PZT-5A	-4.06	-5.44	25.4	1.38				
PZT-5A	-4.00	-5.27	24.1	1.27				
PZT-5A	-3.99	-4.92	18.9	0.93				
PZT-5A	-3.94	-4.92	19.9	1.02				
PZT-5A	-3.93	-5.04	22.0	1.11				
PZT/SS	-6.22	-7.17	13.3	0.95	-4.31	-6.29	31.5	1.98
PZT/SS	-8.57	-9.68	11.4	1.11	-5.91	-8.05	26.6	2.14
PZT/SS	-8.12	-9.22	11.9	1.10	-6.08	-7.56	18.5	1.48
PZT/SS	-9.04	-10.68	15.4	1.64	-6.98	-8.57	18.5	1.52
Average			18.0	1.17			24.1	1.78

means perfect bonding (no strain loss). This gives a strain loss at the interface of about 20% for these laminar samples.

Comparing the OC and SC values of the PZT/SS composites with the SC value of the bare PZT allows the enhancement of the pyroelectric coefficient to be determined. The results of this are summarised in table 4.3, with the percentage enhancement defined as in Eq. 4.3.

$$Enhancement = \frac{(PZT/SS\ Value\ -\ Bare\ SC\ Value)}{Bare\ SC\ Value} \tag{4.3}$$

The enhancement for the SC condition varies from 41.1% to 108.7%, with greater enhancement observed with smaller thickness ratios. A similar result is seen with the OC results, with smaller thickness ratios resulting in greater enhanment, in this case from 21.5% to 76.6% for thickness ratios of 2.7 to 0.4. These results are shown graphically in Fig. 4.5.

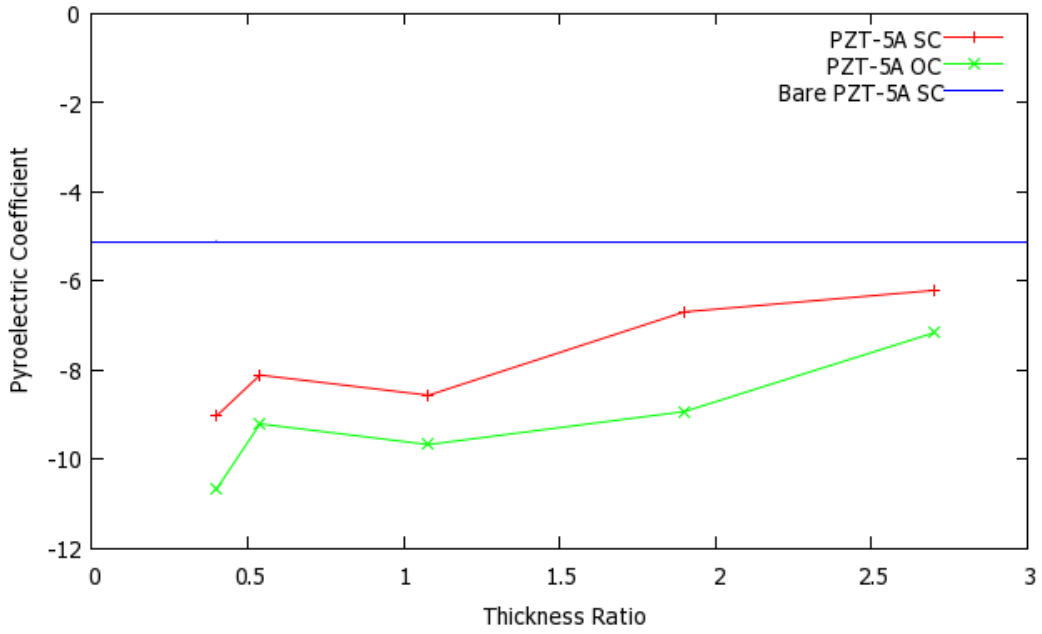

Figure 4.3: Experimental values of the pyroelectric coefficient of SS/PZT-5A/SS composites at both open and short circuit conditions as functions of thickness ratio, with the experimental determined pyroelectric coefficient of bare PZT-5A shown for comparison. The unit of the pyroelectric coefficient is $\times 10^{-4}\ Cm^{-2}K^{-1}$.

The greater enhancement of the pyroelectric coefficient in the laminar composite samples when compared to the bare samples is due to the different thermal

Table 4.3: Enhancement of pyroelectric coefficients of PZT/SS composites at OC and SC compared to bare PZT at SC condition

Thickness Ratio	Open Circuit / %	Short Circuit / %
0.386	76.6	108.7
0.54	58.6	80.0
1.08	67.4	89.1
1.9	30.9	74.6
2.67	21.5	40.0

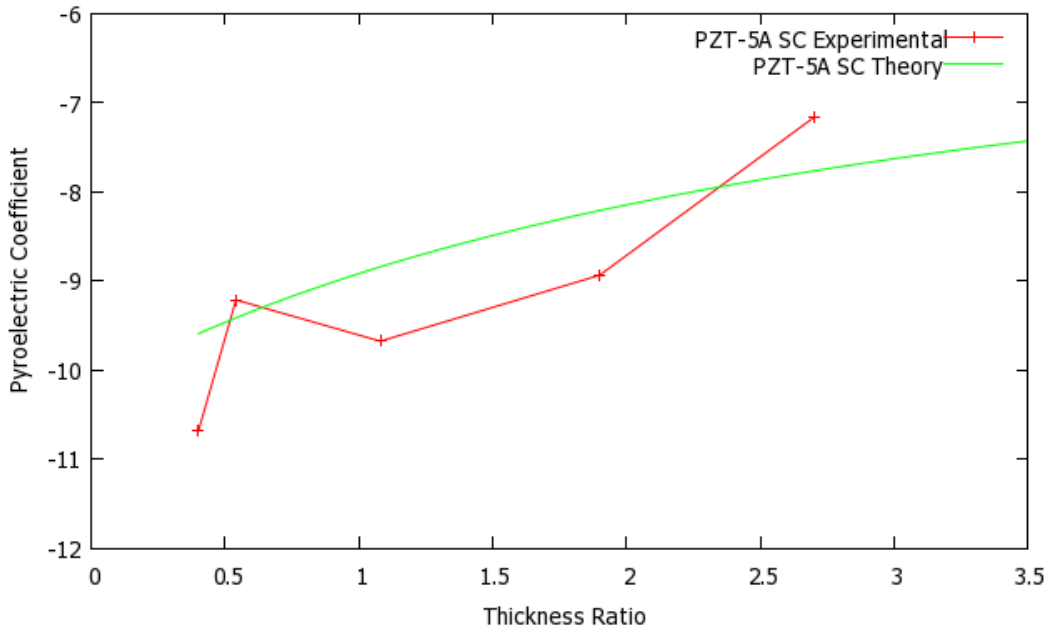

Figure 4.4: Comparison of the experimental and theoretical values of the pyroelectric coefficient of SS/PZT-5A/SS composites under short circuit condition. The unit of the pyroelectric coefficient is $\times 10^{-4}\ Cm^{-2}K^{-1}$

expansion coefficients of the PZT and SS. This results in the PZT and SS expanding at different rates during a temperature change. This causes the SS to extert a force on the PZT, and thus the PZT experiencing a secondary pyroelectric effect as shown in Eq. 4.1. Therefore a difference in pyroelectric coefficient is to be expected.

The difference in pyroelectric coefficient may be understood by considering the effect of the build up of surface charge in the OC condition. This charge creates an electric field across the pyroelectric material which will act to oppose the change in spontaneous polarization of the PZT as it undergoes a temperature change. This is in contrast to the SC condition where the charges are removed from the PZT, so no electric field can be generated to oppose the change in spontaneous polarization.

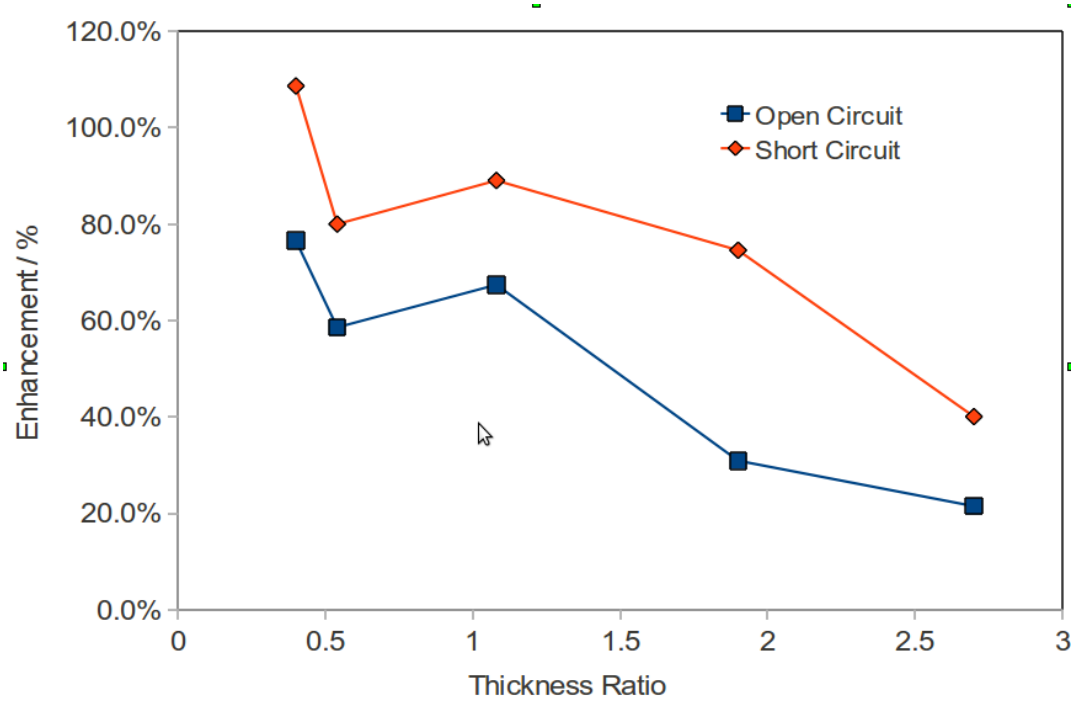

Figure 4.5: Pyroelectric coefficient enhancement compared to bare PZT at SC condition in PZT/SS composites at OC and SC condition

4.6 Conclusions

This series of experiments has shown that the pyroelectric coefficient may differ under open and short circuit conditions, and this difference for PZT may be as much as 20%. Also shown is that the use of laminar composites of PZT and stainless steel can result in the enhancement of the total pyroelectric effect due to the secondary pyroelectric effect. A difference in open and short circuit values of the pyroelctric coefficient is also observed with these laminar composites. This difference suggests that different values of pyroelectric coefficient should be used for OC and SC applications for the same material depending on the application in which it is being used.

Chapter 5

Ferroelectric Electron Emission and Pyroelectric Pulses

5.1 Introduction

This section of the thesis coveres the work conducted on non-accelerated ferroelectric electron emission. Initially an external pulse genertor is used in the manner of previous experiments reported in the literature. This was done to validate the system. Work was then conducted on the design of a system to allow the pyroelectric crystal to be used as the charge generting system in a high voltage pulse generating circuit. The major issue in this section was the switching device to be used. This led to consideration being given to many devices, with the miniature spark gap being found to be the only suitable one. A circuit was then built around this device and a crystal, and the production of positive and negative high voltage pulses being demostrated. This pulsing circuit was then used to trigger ferroelectric electron emission in PT cathodes. An investigation into the optimum pulse parameters was conducted by applying

both positive and negative high voltage pulses to the front and rear electrodes of the cathode. This also allowed an analysis of the emission mechanism to be performed. The effect of the grid structure of the cathode was then investigated by using a variety of different grid structures.

The major areas covered are the use of different pulse parameters i.e. positive and negative high voltage pulses applied to both the front and rear electrodes of the cathode. The use of a variety of values of the external capacitor C_{Ext} was then investigated.

5.2 Results

5.2.1 External Pulse Generator

The external high voltage pulse generator was used to apply a positive high voltage pulse to the rear electrode of the ferroelectric cathode. This was done to confirm proper operation of the system. Figure 5.1 shows typical traces. Several points on these traces are labelled a-g. These points denote important aspects of the emission process. An explanation of these points is given in Fig 5.2. The points labelled a-g in Fig 5.1 correspond to subfigures 5.2a to 5.2g of Fig 5.2. These two figures will be discussed together to describe the emission process. Point 'a' / Fig 5.2a show the pulse being applied to the rear electrode of the cathode. Note the pulse of applied current and the corresponding rise in voltage on the rear of the cathode. Point 'b' / Fig 5.2b shows the point at which the plasma begins to form on the front surface of the cathode, and the start of positive ion emission. This results in an increase in the capacitance of the cathode due to the plasma acting as an electrode. Notice at this point

the dip in the pulse voltage as the capacitance increases and the corresponding second pulse current peak to restore the pulse voltage. The fall in pulse voltage with a constant charge on a capacitor is consistent with what is expected from $Q = CV$. At point 'c' / Fig 5.2c the emission of ions continues due to the excess of unscreened ions in the plasma.

Points 'd' and 'e', and Figs. 5.2d and 5.2e show the point at which the applied pulse is stopped, the relaxation of the dipoles in the PZT begins to occur, and the positive ion emission ends.

Points 'd', 'e' and 'f' and Figs. 5.2d, 5.2e and 5.2f show the ending of the positive ion emission, the stopping of the applied pulse and the beginning of electron emission. The removal of the applied pulse on the rear of the cathode removes the dielectric polarisation of the cathode material, and thus the electrons bound to the ferroelectric surface by this are now released, causing electron emission. Point 'g' / Fig 5.2g shows the final state of the emission system, where all free electrons have been emitted.

5.2.2 High Voltage Pyroelectric Pulse Production

The pyroelectric pulsing circuit was used with a both a 50 pF and 100 pF C_{Ext} and a 50 pF load capacitor. This was done to confirm proper operation of the pulsing circuit and measurement systems. Figure 5.3 shows the voltage time profies on the load capacitor for the pyroelectric pulse circuit in both positive and negative pulse configurations. Since these profiles are almost identical only the positive ones will be discussed. Several interesting features of the voltage variation with time are present. Firstly the very fast rise time of the voltage,

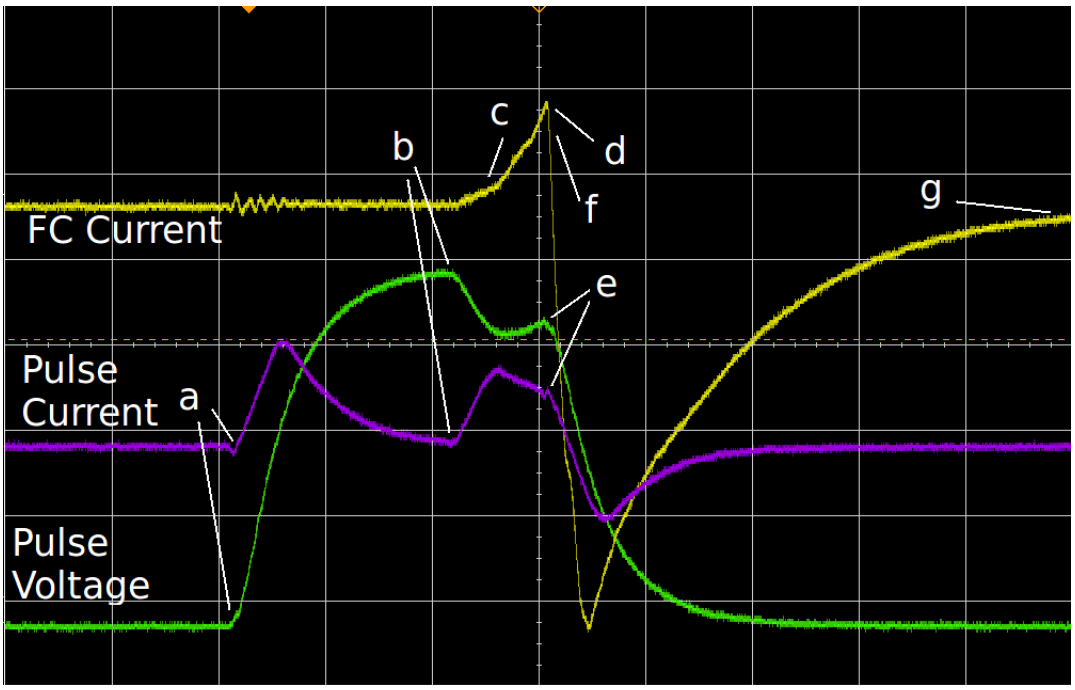

Figure 5.1: Oscilloscope trace of emission when an external pulse generator applied a positive pulse to the rear electrode. The yellow trace is the FC current, the purple trace is the pulse current and the green trace is the pulse voltage.

which is on the order of a few tens of ns. Secondly, the peak of the voltage at around 1.5 kV with C_{Ext} = 100 pF and 1000 V with C_{Ext} = 50 pF. This is interesting when considered with the profile of the pulse over the next few μs, which show the pulse decaying to around 1000 V and 700 V when C_{Ext} = 100 pF and 50 pF respectively. By considering the electrical condition of the system the post pulse voltage can be calculated. First the total pulse charge is calculated:

$$Q = C_{ext} V_{spark} \tag{5.1}$$

This gives a charge Q of 152 nC and 76.5 nC for C_{Ext} = 100 pF and 50 pF respectively. This value is then used to calculate the final voltage V_f:

$$V_f = \frac{Q}{C_{ext} + C_{load}} \tag{5.2}$$

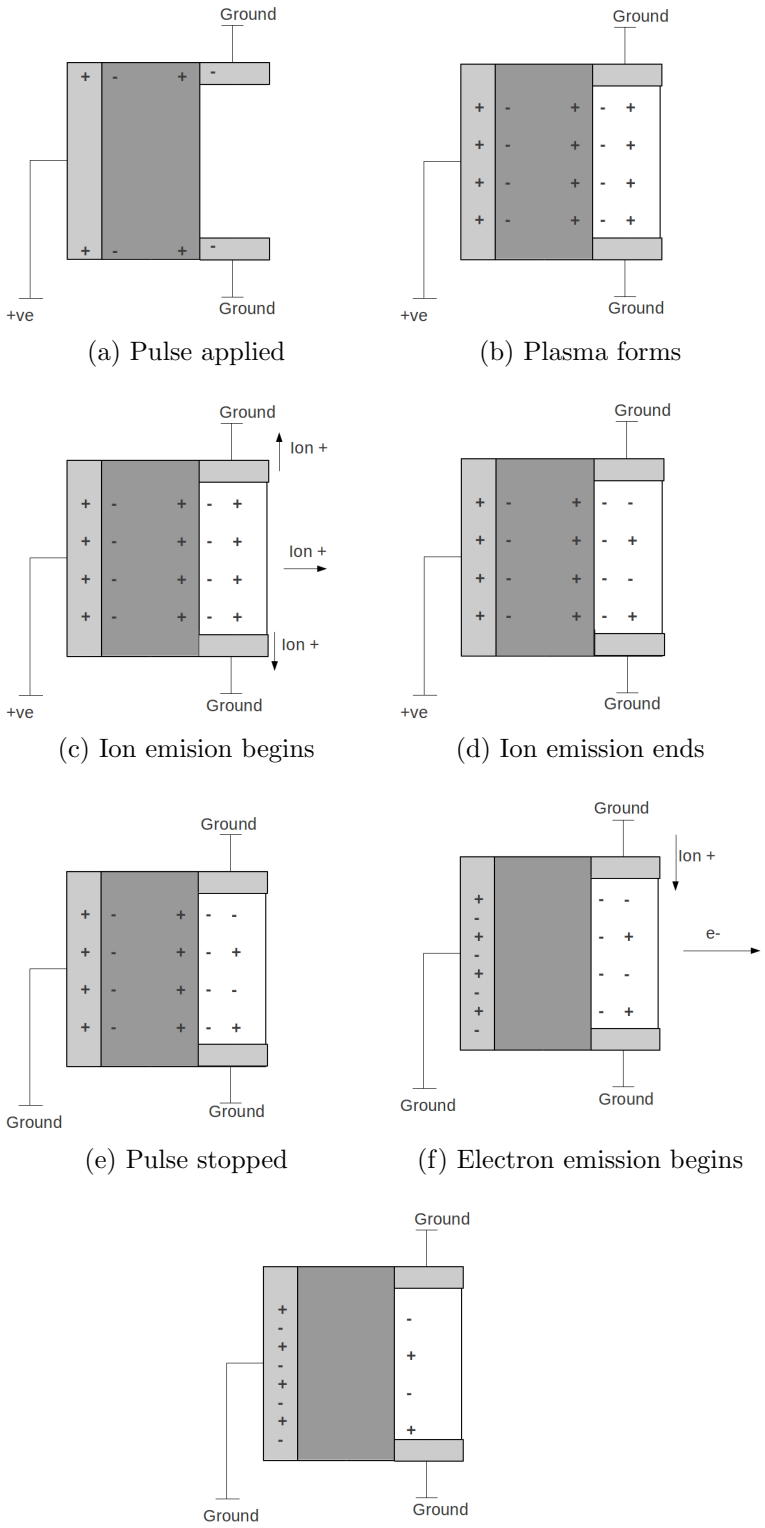

(a) Pulse applied

(b) Plasma forms

(c) Ion emision begins

(d) Ion emission ends

(e) Pulse stopped

(f) Electron emission begins

(g) Electron emission ends

Figure 5.2: Positive pulse to the rear electrode with the external pulse generator

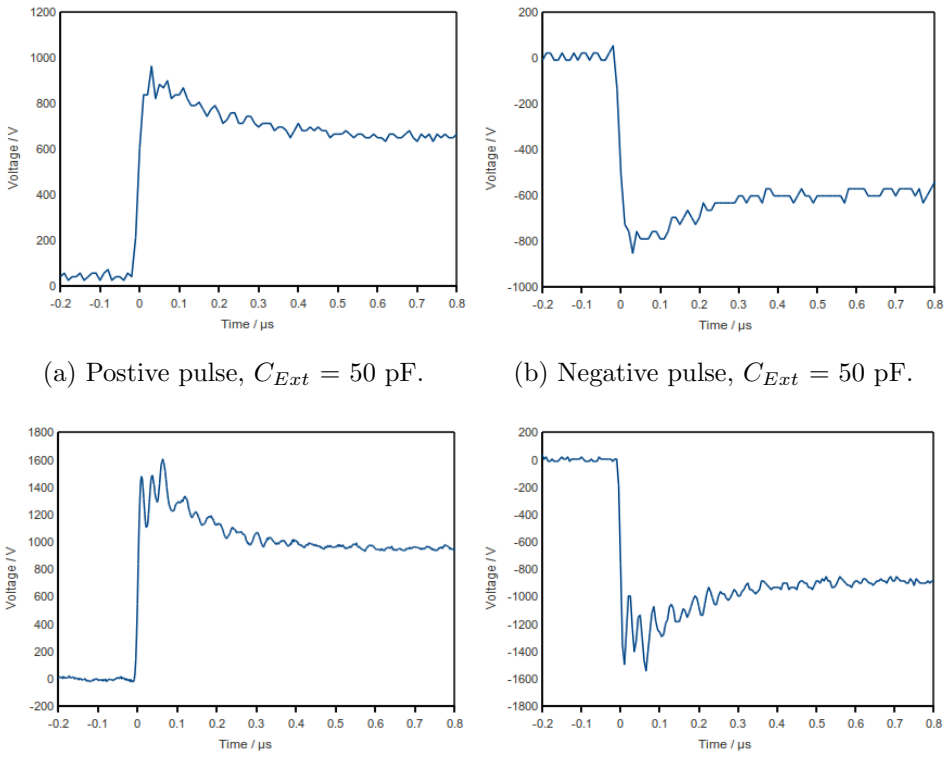

(a) Postive pulse, $C_{Ext} = 50$ pF.

(b) Negative pulse, $C_{Ext} = 50$ pF.

(c) Postive pulse, $C_{Ext} = 100$ pF.

(d) Negative pulse, $C_{Ext} = 100$ pF.

Figure 5.3: Positive and negative high voltage pulses produced by the pyroelectric pulsing circuit with various values of C_{Ext} .

This gives theoretical voltages of 1007 V and 757 V, which is very close to that observed in both positive and negative experimental runs. It should be noted that the switching voltage of the spark gap V_{spark}, while quoted as 1500 V by the manufacturer does vary between runs. This variation may be accounted for by calculating the breakdown voltage from the temperature change on the pyro crystal, and therfore the charge and voltage generated.

Thus the fact that the pulse peaks at around the switching voltage after a few tens of ns, and then settles to the value expected theoretically suggests that the period between these two states is due to the slew rate of the capacitor, i.e the time it takes the capacitor to respond to the change in voltage.

5.2.3 Pulse Polarity and Application

The pyroelectric pulsing system, as detailed in section 5.2.2 was used to apply a high voltage pulse to the a ferroelectric cathode. Both positive and negative pulses were used, and they were applied to both the front and rear electrodes. External capacitances of $C_{Ext} = 50$ pF and 100 pF were used in all configurations. A summary of the pulsing sytem charge Q_{pyro}, collected current I_{FC}, collected charge Q_{FC}, and ratio of Q_{pyro} to Q_{FC} with differing pulse parameters is shown in table 5.1. The peak emitted currents with $C_{Ext} = 50$ pF range from 0 A in the 'positive pulse, front electrode case' to -6.1 mA in the 'negative pulse, front electrode case'. A similar trend is seen when considering Q_{FC}; 0 nC and -4.99 nC for the 'positive front' and 'negative front' cases. In the 'negative rear' case and 'positive rear' cases with $C_{Ext} = 50$ pF the results show a similar but opposite trend. These case give I_{FC} of -0.11 mA and 0.03 mA, and Q_{FC} of -0.06 nC and 0.06 nC respectively. To account for any variation in emission properties due to variations in the pulsing charge the ratio of pulsing system charge to collected charge $|Q_{pyro}|/|Q_{FC}|$ is calculated. For the 'positive front' case the results of this calculation is 0% with $C_{Ext} = 50$ pF and 100 pF. In the 'pos front' case the ratio is 0.06% and 0.03% with $C_{Ext} = 50$ pF and 100 pF. The 'negative rear' case gives a similar result of 0.06% and 0.07 % with $C_{Ext} = 50$ pF and 100 pF. The 'negative front' case gives by far the best ratio, with values of 4.12% and 3.14% with $C_{Ext} = 50$ pF and 100 pF.

Table 5.1: Summary of data for the peak current and total emitted charge for positive and negative pyroelectric pulses applied to the front and rear electrodes, using capacitances of 50 pF and 100 pF. The current was collected by the Faraday cup.

C_{Ext} / pF	Pulse Polarity	Electrode	Q_{Pyro} / nC	I_{FC} / mA	Q_{FC} / nC	$\lvert Q_{FC}\rvert/\lvert Q_{Pyro}\rvert$ / %
50	Positive	Rear	97.8	0.03	0.06	0.06
		Front	104	0	0	0
	Negative	Rear	-97.8	-0.11	-0.06	0.06
		Front	-121	-6.1	-4.99	4.12
100	Positive	Rear	219	0.04	0.073	0.03
		Front	-207	0	0	0
	Negative	Rear	-190	-0.2	-0.13	0.07
		Front	-190	-6.7	-6.16	3.24

5.2.3.1 Time Profiles

This section will look at the time profiles of the pulse voltage, collected current and collected charge in the emission process. Time profiles for positive and negative pulses to the front and rear electrodes will be examined, with C_{Ext} = 50 pF and 100 pF. This process will be used to gain insight into the emission process, in particular the behaviour of the surface plasma over time. From this reasons for the very different emission properties detailed in table 5.1 will be suggested.

One major aspect of the time profiles is that they differ considerably depending on the pulse applicattion method. These differences are of great interest since they give information on the emission process, and can be compared to the time profiles in Fig. 5.3. This comparison gives further information on the emission process since it gives a reference time profile where a 'static' capacitor (i.e. one with no change of capacitance with time, and no emission of electrons).

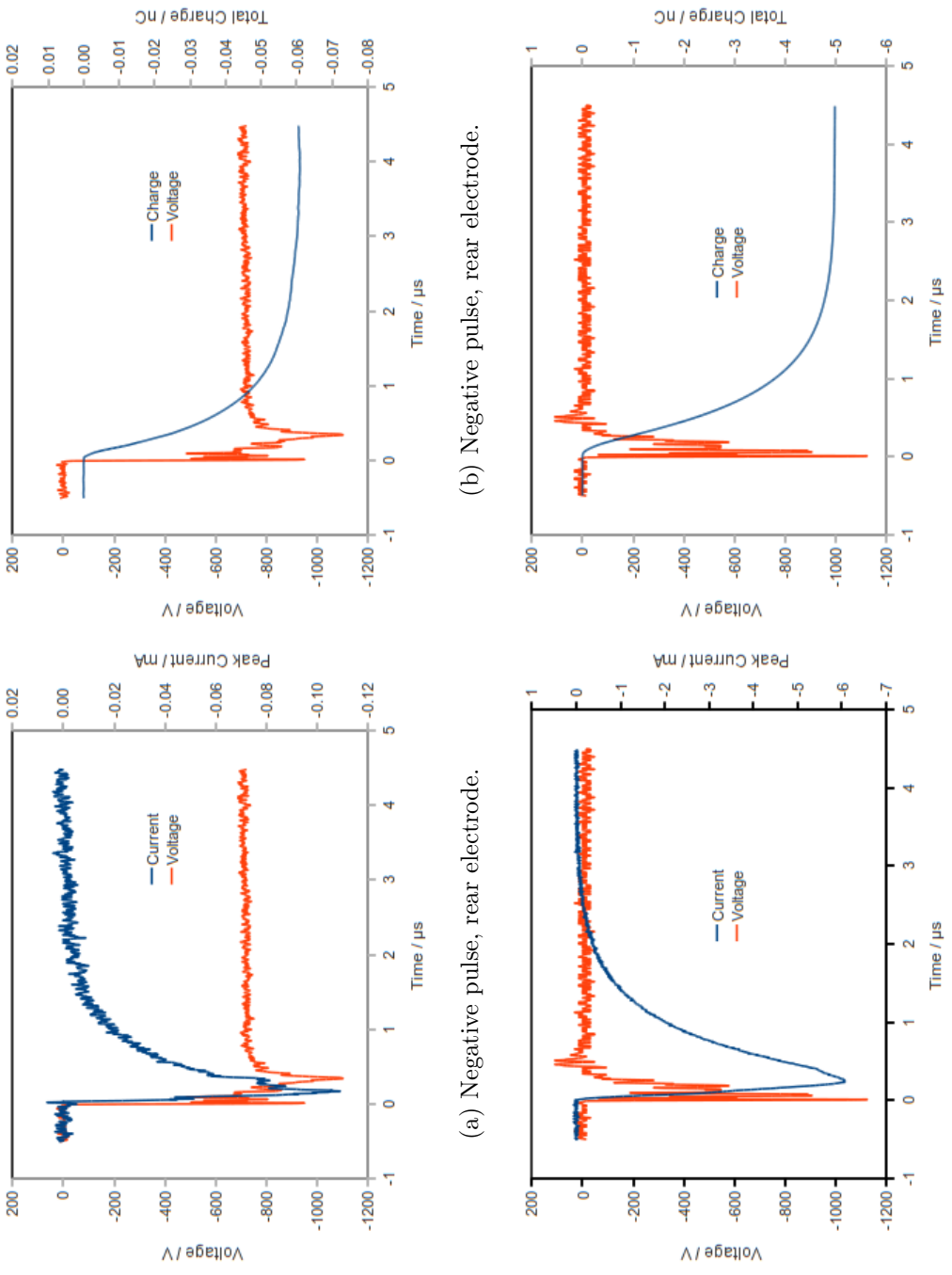

(a) Negative pulse, rear electrode.

(b) Negative pulse, rear electrode.

(c) Negative pulse, front electrode.

(d) Negative pulse, front electrode.

Figure 5.4: Emission current, charge and pyro voltage when a negative voltage is applied to the front and rear electrodes using a 1.5 kV spark gap and with $C_{Ext} = 50$ pF

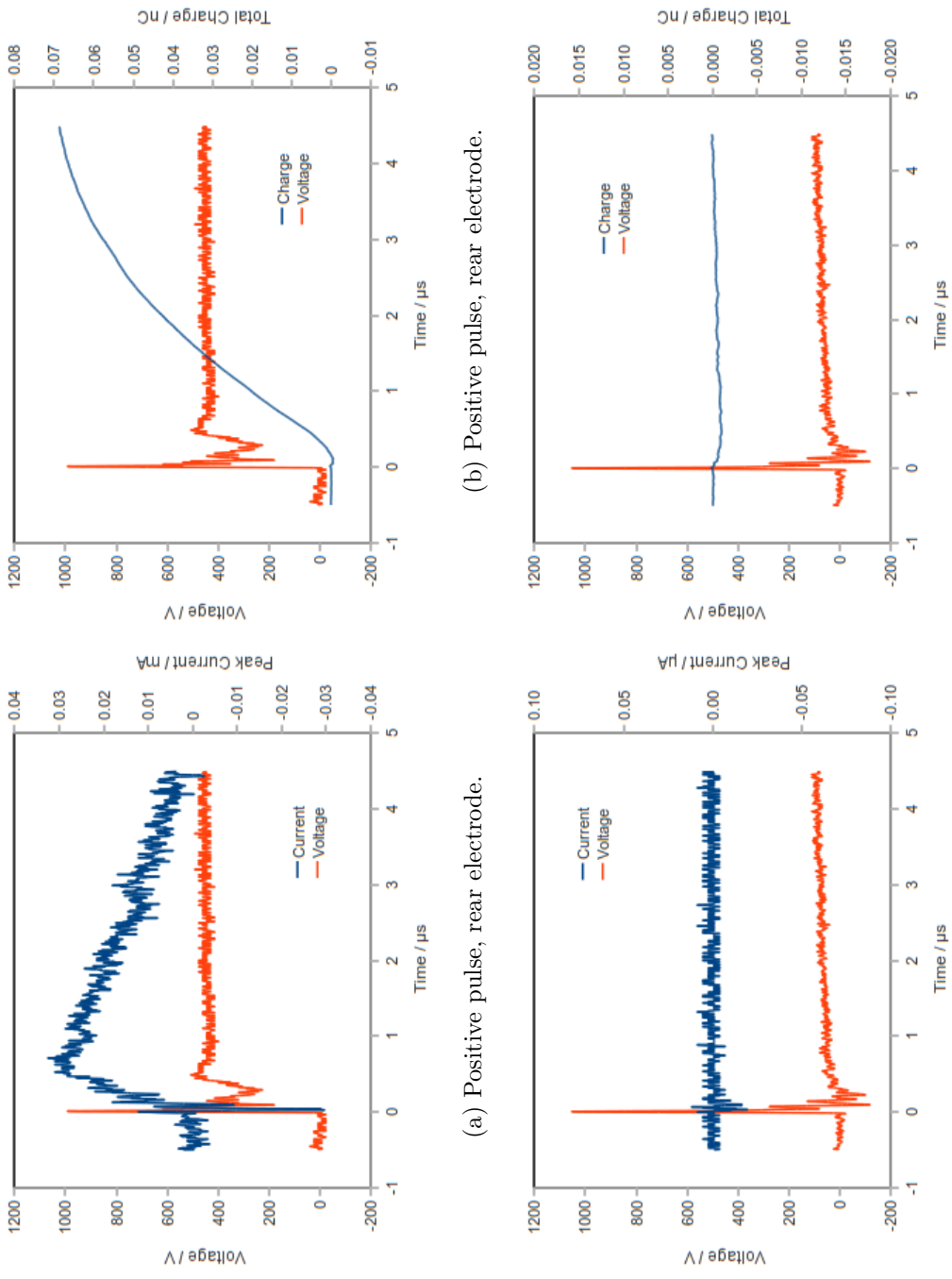

(a) Positive pulse, rear electrode.

(b) Positive pulse, rear electrode.

(c) Positive pulse, front electrode.

(d) Positive pulse, front electrode.

Figure 5.5: Emission current, charge and pyro voltage when a negative voltage is applied to the front and rear electrodes using a 1.5 kV spark gap and with $C_{Ext} = 50$ pF

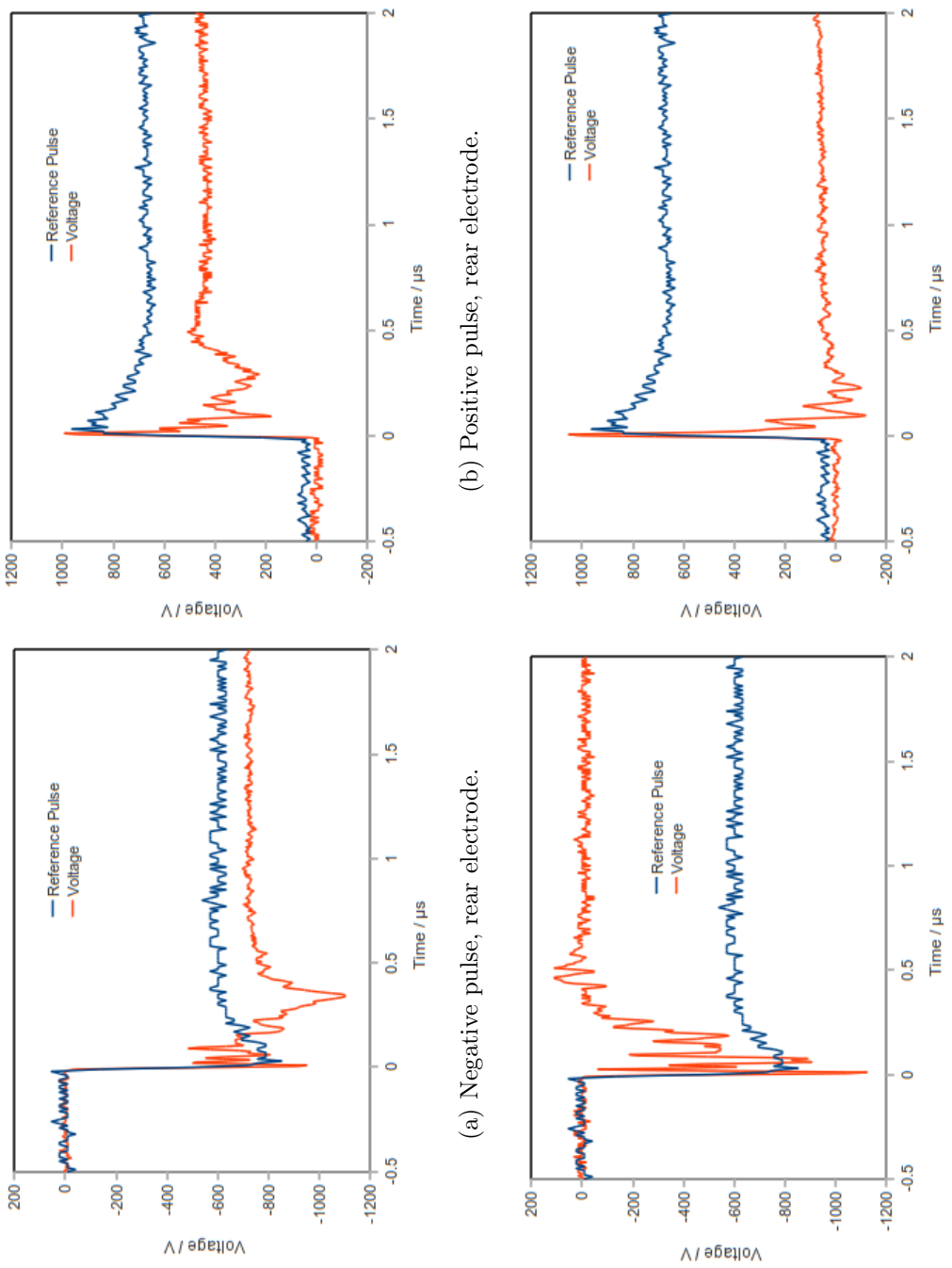

(a) Negative pulse, rear electrode.

(b) Positive pulse, rear electrode.

(c) Negative pulse, front electrode.

(d) Positive pulse, front electrode.

Figure 5.6: Comparison of voltage pulse profiles on the cathode with different pulse parameters and reference pulses produced using a load capacitance. $C_{Ext} = 50$ pF

A comparison of the voltage pulse profiles on the cathode with those produced on a load capacitor are shown in Fig. 5.6. Figure 5.6a shows a negative pulse applied to the rear electrode and a negative pulse applied to the load capacitor. This shows that the two pulses are quite similar, with several of the same features. Both pulses exhibit a fast rise to around 1000 V, and after around 1 μs settle to a constant voltage, which is around 600 V for the reference pulse and 750 V for the emission pulse. However, there is a significant difference in the profile of the pulses between the initial peak at 1000 V and the steady voltage after 1 μs. While the reference pulse smoothly decreases from the peak to the steady state due to the capacitor slew rate, the emission pulse initially drops sharply immidiately after the initial peak and then rises for a few hundred ns, before settling to the steady voltage. These features of the pulse profile may be explained by considering the role of plasma in the emission process. The rapid drop after the peak may be explained by the plasma formation on the front surface of the cathode, which increases the capacitance of the cathode. The subsequent rise is then due to the 'evaporation' of the plasma on the front surface of the cathode, which reduces the capacitance of the system to it's original pre-plasma value. The final steady state results when the plasma has completly evaporated, leaving just the static capacitance of the cathode.

Figure 5.6b shows the data for a positive pulse applied to the rear electrode, and the corresponding positive pulse applied to a 50 pF load capacitor. A very similar trend is seen in the emission pulse to that discused above; the initial peak of around 1000 V is followed by a rapid decrease in voltage, a slower increase and then finally a steady state voltage. The steady state voltage is in this case around 500 V, which is lower than in the previous case.

The 'negative pulse, front electode' time profile for the cathode and the corresponding reference pulse are shown in Fig. 5.6c. The emission pulse in this

case differs greatly from both the previous (i.e. rear electrode) cases, as well as the reference pulse. While the redreference pulse follows the familiar profile of initial peak followed by steady reduction to a steady state, the emission pulse peaks at around 1000 V and then rapidly drops to around 0 V. This very different voltage profile may be explained by considering the very different electrical condition in this set up. While in the 'rear electrode' cases the plasma is electrically insulated from the pulse by the cathode material, in the 'front electrode' cases this is not the case. The pulsing system and the plasma are in electrical contact for some period during the emission process, allowing positive ions to flow from the plasma directly into the pulsing system. It is this process of flow of ions between the 'pulsing system/cathode' system that allows the rapid and large drop in voltage.

Figure 5.6d shows a positive pulse applied to the front electrode of the cathode, and the corresponding reference pulse. A similar trend is seen to that described above; an initial peak of around 1000 V and then a rapid drop to around 0 V. This is again explained by the electrical contact of the pulsing system with the plasma. This allows the electrons produced in the plasma to be removed from it by the positive voltage on the pulsing system.

These observations can then be applied to the time profiles in Figs. 5.4 and 5.5. Figure 5.4 shows the time profile of the pulse voltage and collected current when a negative pulse is applied to the rear electrode. Since the triggering pulse is electrically isolated from the plasma the only source of electrons for emission is the plasma itself.

5.2.3.2 Emission Mechanism

The emission properties of ferroelectic cathodes are different with different pulse parameters. This report details proposed differences in the emission process for

various pulse parameters which explain these differences.

The emission process of the external pulsing system can be described as follows. A positive voltage is applied to the rear electrode by the pulse generator, inducing reorientation of the dipoles in the PZT (Fig. 5.2a). Plamsa forms on the front of the cathode, and electrons are attracted to the positive bould charges in the PZT, screening them. This leaves positive ions in the plasma free to be emitted (Fig. 5.2b). Ions in the plasma flow towards the electrodes, where they are compensated by free electrons in the metal electrode, as shown in Fig. 5.2c). The applied pulse is stopped, and the applied voltage drops to 0 V, ending ion emission (Figs. 5.2d and 5.2e). As the applied pulse voltage falls to 0 V the dipoles in the PZT relax, releasing the previously bound electrons (Fig. 5.2e). These electrons do not flow to ground since the plasma has eveporated by this point. Once all charges are compensated emission ends (Fig. 5.2f).

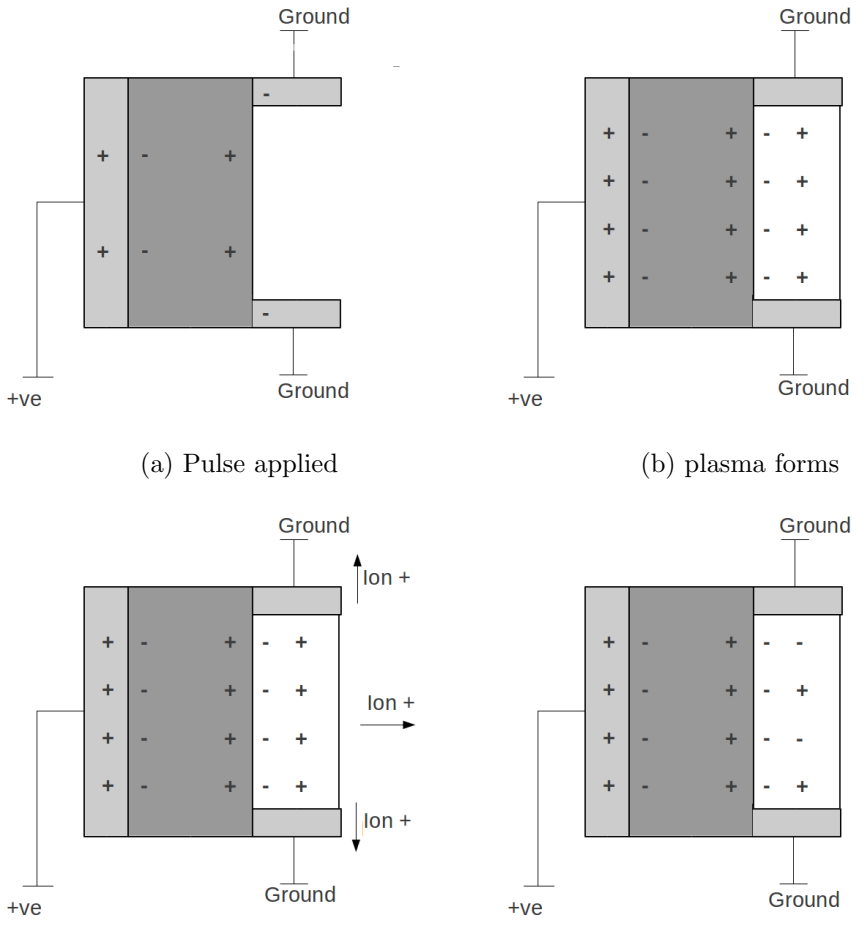

(a) Pulse applied

(b) plasma forms

(c) Ion emission

(d) Process complete

Figure 5.7: Positive pulse to the rear electrode with the pyro pulse generator

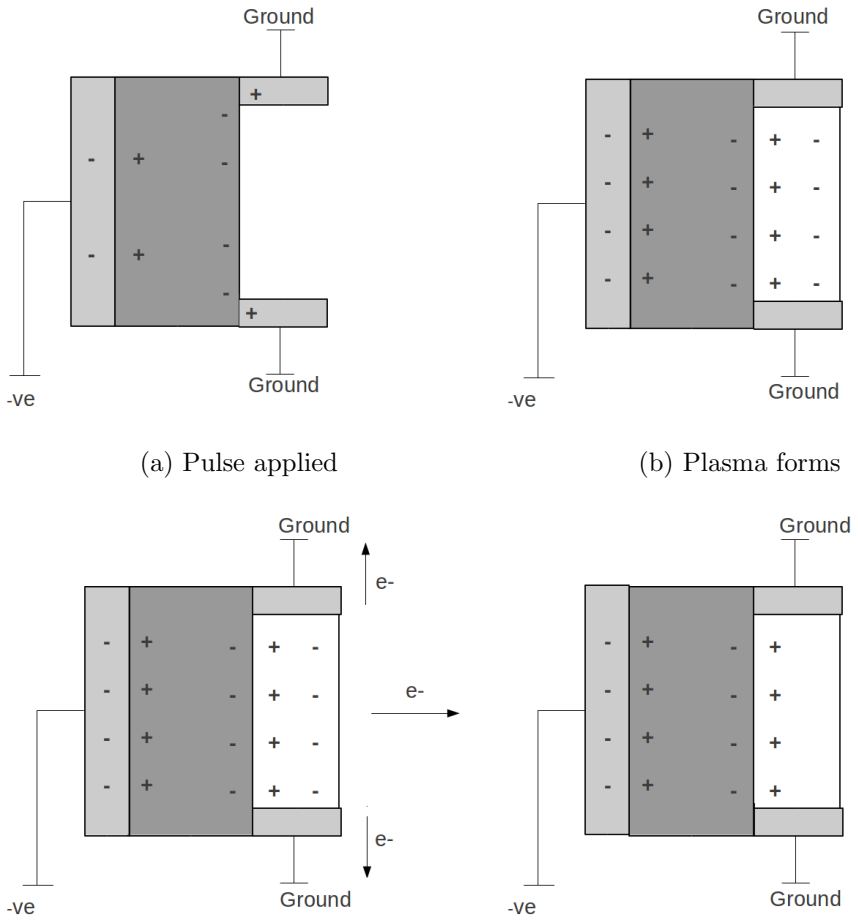

(a) Pulse applied

(b) Plasma forms

(c) Electron emission

(d) Process complete

Figure 5.8: Negative pulse applied to the rear electrode by the pyro pulse generator

Figure 5.7 depicts the emission process when a positive pulse is applied to the rear electrode of the cathode by the pyroelectric pulsign system. This system is different to the previously discussed external pulsing system as the rear of the cathode is not grounded after the application of the pulse. Figures 5.7a to 5.7c proceed in a similar manner to the previous system. However, the process ends in figure 5.7d since the lack of grounding of the system prevents the relaxation of the polarisation charge, and the associated electron emission.

Figure 5.8 shows the emission process when a negative pulse is applied to the rear of the cathode using the pyroelectric pulsing system. This is very similar

to the process for a positive voltage applied to the rear electrode as shown in Fig. 5.7 with the pyroelectiric pulse system, but with all polarities reversed. Experimental results support this explanation, as similar total emitted charges are seen in both these configuartions, but with opposite polarities, as shown in Table 5.1.

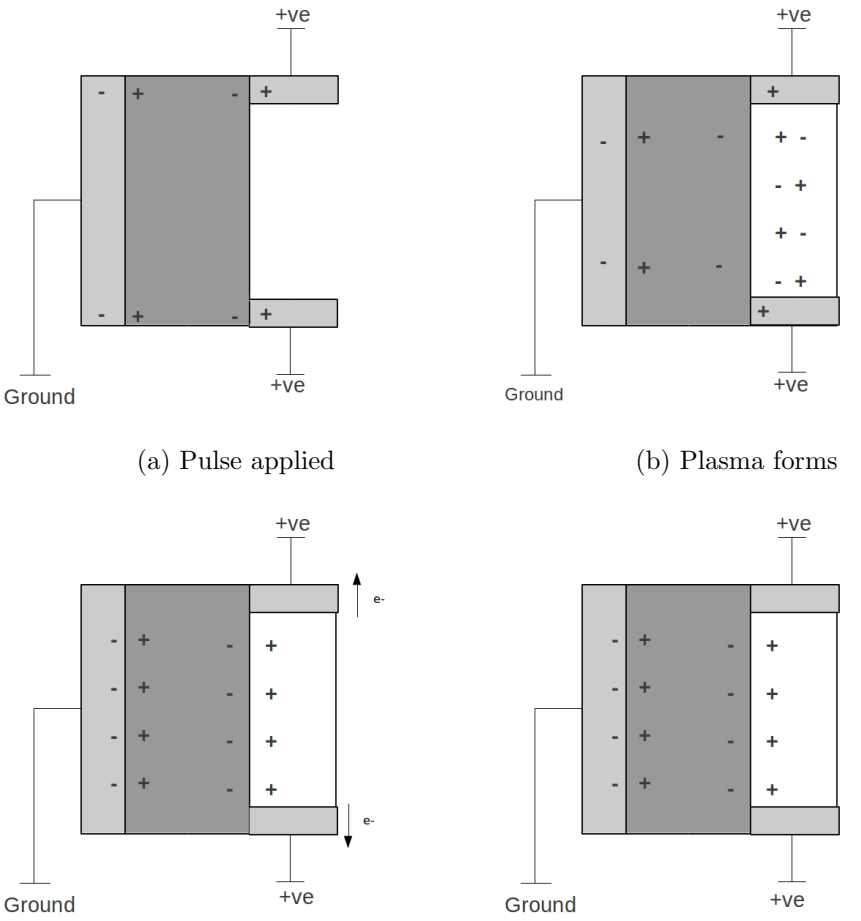

(a) Pulse applied

(b) Plasma forms

(c) Electrons removed from cathode

(d) Process complete

Figure 5.9: Positive pulse applied to the front electrode by the pyro pulse generator

Figure 5.9 illustrates the process when a positive pulse is applied to the front electrode with the pyroelectric pulse generator. Figure 5.9a shows the application of the pulse. Figures 5.9b and 5.9c show the plasma forming, and the electrons being removed from it by the positive charge of the pyroelectric pulsing system. This would result in no emission of either ions or electrons occuring, since the removal of electrons during plasma production greatly limits the quantity of plasma produced, and any positive ions remain to screen the polarisation charges in the cathode. This is supported by experimental data where no emission is detected in this configuration.

No emission occurs in this case because the positive voltage of the front electrode removes electrons produced in the field emission stage. This prevents significant plasma formation, and reduces the applied voltage as the pulsing system absorbs electrons.

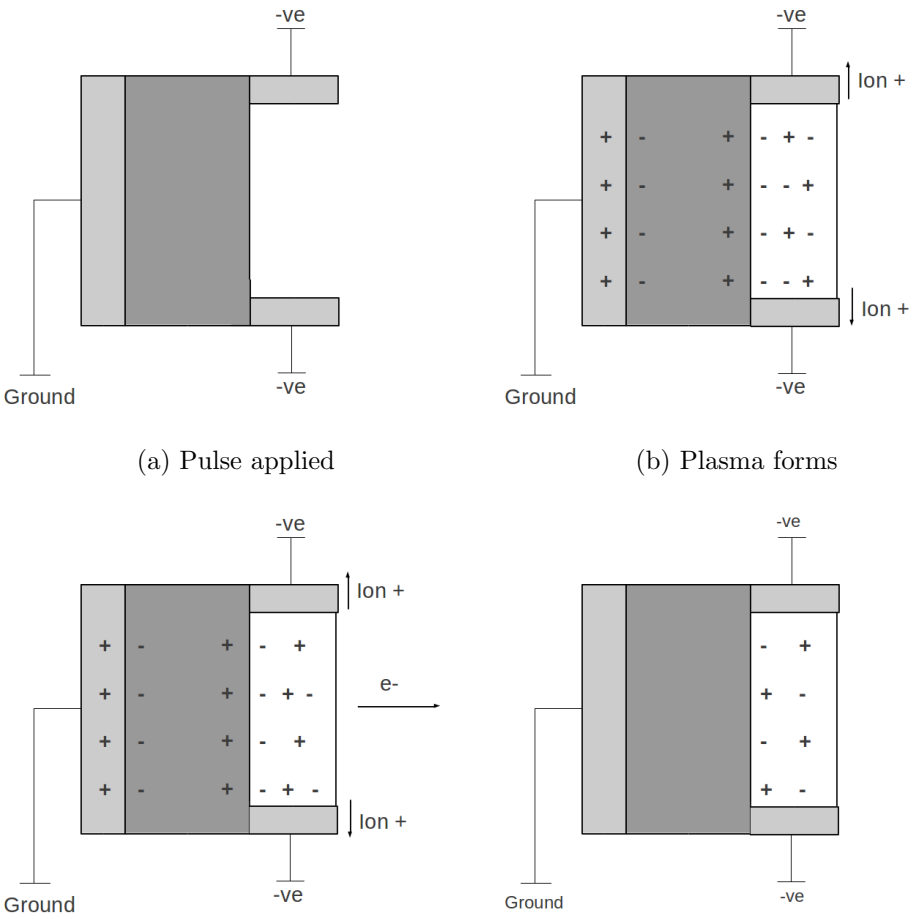

(a) Pulse applied

(b) Plasma forms

(c) Electron emission

(d) Process complete

Figure 5.10: Negative pulse applied to the front electrode by the pyro pulse generator

Figure 5.10 shows the emission process when a negative pulse is applied to the front electrode by the pyroelectric pulsign system. Figure 5.10a shows the application of the pulse. Figure 5.10b shows the formation of the plasma. The withdrawal of positive ions from the plasma to the pulsing systems should be noted. This results in more electrons avaliable for emission. Figure 5.10c shows the emission of electrons from the plasma. Figure 5.10d shows the final state of the system. Experimental data again supports this mechanism, since the withdrawl of ions from the plasma increases the number of uncompensated electrons available for emission, and a greater quantity of collected electrons

are seen in this configuration. The route to ground provided for the electrons in the rear pulse configuration may also assist in the large emission charge.

Figure 5.10 shows the emission process when a negative pulse is applied to the front electrode. The process is as follows. A negative pulse is applied to the front electrode, initiating the plasma formation process (Fig. 5.10a). The plasma expands, electron emission occurs and ions are withdrawn from the plasma by the applied pulse (Fig. 5.10b). Emission continues, as the voltage on the cathode reduces (Fig. 5.10c). Emission then ends (Fig.5.10d).

5.2.4 External Capacitance and Electrode Structure

The value of C_{Ext} was investigated to determine its effect on the emission current and charge. Also investigated was the structeure of the electrode. The results of this investigation for C_{Ext} = 50 pF, 72 pF, 82 pF, 100 pF, 110 pF and 122 pF, and electrode structures of ring, 50 bar, 50 mesh and 100 mesh is shown in Figs. 5.11 and 5.12. This shows that there is a general trend of increasing peak current and total emitted charge with increasing C_{Ext} , and that this trend is similar with all electrode types studied. Tables 5.2 and 5.3 show that peak current ranged from -13.2 mA with C_{Ext} = 50 pF and a 50 bar electrode, to -62.2 mA with C_{Ext} = 122 pF and a 100 mesh electrode. The total charge ranged from -10.1 nC with C_{Ext} = 50 pF and a 50 bar electrode to -60.2 nC with C_{Ext} = 122 pF and a 50 mesh electrode.

Table 5.4 shows the full data for this set of experiments. In addition to the electrode type, the distance between the grid elements d_{gap} is also shown. The temperature change of the pulsing is shown, from which the charge on the pulsing system is calculated. A pyroelectric coefficient value of $1.9 \times 10^{-4} Cm^{-2}K^{-1}$ is

Table 5.2: Peak current data for various external capacitances and different grid types of the electrode. A negative pulse is applied to the front electrode in all cases.

	I_{max} / mA			
C_{Ext} / pF	Ring	50 Bar	50 Mesh	100 Mesh
120	-48.0	-45.0	-60.9	-62.2
110	-45.4	-47.6	-48.6	-45.1
100	-39.3	-36.2	-50.3	-46.3
82	-33.0	-26.8	-37.4	-35.5
72	-30.8	-21.3	-30.2	-29.5
50	-14.0	-13.2	-20.0	-16.7

used for this calculation[11]. The collected charge value Q_{col} divided by this value is also shown to compensate for variations between runs. This shows that there is little variation between the anode types.

The similarity of the trends for the different electrode structures across the range of C_{Ext} can be explained by considering the role of the plasma and the pulsing section of the system. Since a greater charge on the pulsing system results in a greater charge transfer between the cathode and therfore the plasma. This suggests that the major role of the plasma is simply to provide a route for electrons to be emitted into vacuum from the emission system. It then follows that as long as the electrode is capable of generating surface plasma then there will be little difference in the emission charcteristics with differing electrodes.

Table 5.3: Total emitted charge data for various external capacitances and different grid types of the elecetrode. A negative pulse is applied to the front electrode in all cases.

	Q_{tot} / nC			
C_{Ext} / pF	Ring	50 Bar	50 Mesh	100 Mesh
122	-45.6	-51.2	-60.2	-54.0
110	-43.1	-46.7	-48.0	-53.6
100	-40.8	-47.1	-54.8	-38.7
82	-30.9	-24.6	-33.0	-39.2
72	-28.2	-16.9	-29.7	-25.0
50	-11.4	-10.1	-17.7	-21.3

Table 5.4: Full data for investigation of external capacitance and grid spacing. Spark gap voltage is 1500 V. The current was collected by the large anode.

Electrode	ΔT / K	C_{Ext} / pF	d_{gap} / μm	Q_{Pyro} / nC	I_{col} / mA	Q_{col} / nC	Q_{col} / Q_{Pyro}
Ring	39.3	120	2000	-186.7	-48.0	-45.6	24.4%
	37.3	110	2000	-177.2	-45.4	-43.1	24.3%
	35.7	100	2000	-169.6	-39.3	-40.8	24.1%
	29.8	82	2000	-141.6	-33.0	-30.9	21.8%
	26.7	72	2000	-126.8	-30.8	-28.2	22.2%
	21.0	50	2000	-99.8	-14.0	-11.4	11.4%
50 Bar	41.3	120	430	-196.2	-45.0	-51.2	26.1%
	37.3	110	430	-175.8	-47.6	-46.7	26.6%
	34.3	100	430	-162.0	-36.2	-47.1	29.1%
	29.6	82	430	-140.6	-26.8	-24.6	17.5%
	27.3	72	430	-129.7	-21.3	-19.9	13.0%
	20.0	50	430	-95.0	-13.2	-10.1	10.6%
50 Mesh	40.0	120	430	-190.0	-60.9	-60.2	31.7%
	37.3	110	430	-177.2	-48.6	-48.0	27.6%
	34.3	100	430	-162.9	-50.3	-54.8	28.1%
	30.4	82	430	-144.4	-37.4	-33.0	22.9%
	26.4	72	430	-125.4	-30.2	-29.7	23.7%
	19.0	50	430	-90.3	-20.0	-17.7	16.9%
100 Mesh	40.0	120	210	-190.0	-62.2	-54.0	28.4%
	36.9	110	210	-175.3	-45.1	-53.6	30.6%
	33.5	100	210	-159.1	-46.3	-38.7	24.3%
	30.0	82	210	-142.5	-35.5	-39.2	27.5%
	26.8	72	210	-127.3	-29.5	-25.0	19.6%
	20.4	50	210	-96.9	-16.7	-21.3	22.0%

5.2.5 Cathode Material

Several different cathode materials were studied in this section. Very thin (191 μm) PZT-5A and PZT-5H were used to create cathodes in a similar process to the previous cathodes. No emission was detected in these cathodes in the 'neg front' regieme. Thicker (1 mm) PZT samples of the Pz26 composition were also studied. It was also not possible to trigger emission from these cathodes. The most likely cause of this is the higher capacitance of these cathodes, which is much greater than the capacitance of C_{Ext} , due in the PZT-5A and 5H case to the thinness of the PZT and in the Pz26 case to the high dielectric constant of 1300. This results in a very low voltage appearing on the cathode, so the initial field emission does not occur.

5.2.6 Resetting Relay

It is clear that it is desireable that it is possible to ground the charging section of the pulsing circuit on demand, so as to reset it after emission. To do this the possible switching mechanisms were again looked at. The requirements were the same as previously, with the exceptions that switching speed was no longer important but the ability to manually switch is. The only device meeting this specification is the reed relay. A device was selected and connected to the system as shown in Fig. 5.13. This relay could be switched manually by a custom circuit. The system was then run as usual, but when an attempt to fire the system was made no pulse was detected on the cathode, even with temperature changes well in excess of those normally used. This is likely due to the impedance of the reed realy being insufficient. It was not possible to determine this definitevly from the data sheets for the relay due to the large variation between the typical and minimum impedance values stated by the manufacturer.

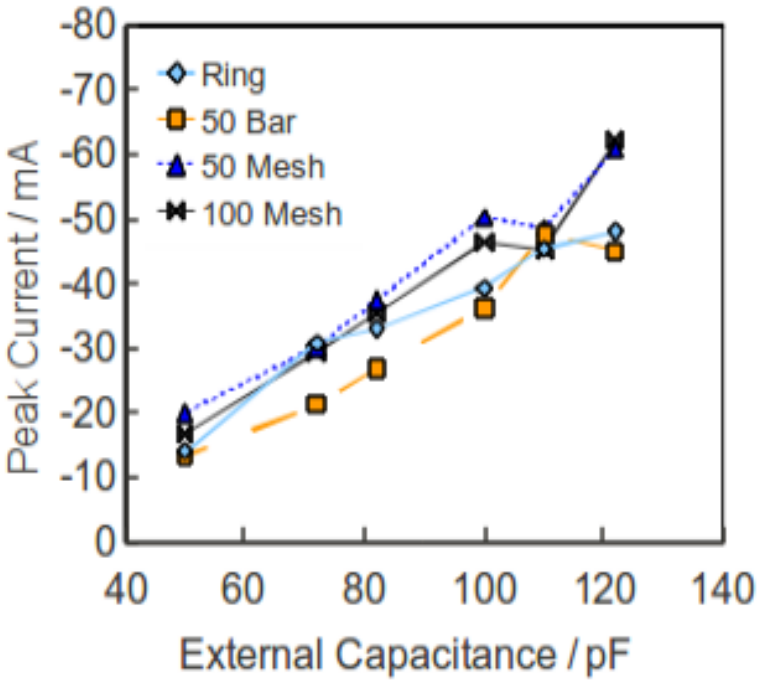

Figure 5.11: Variation of emission current with external capacitance for ring, 50 bar , 50 mesh and 100 mesh electrodes

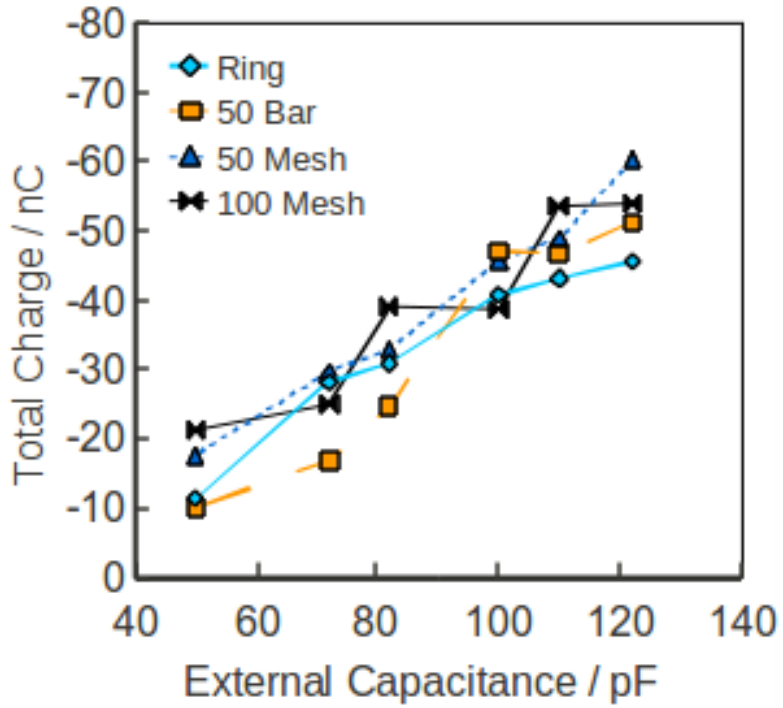

Figure 5.12: Variation of emitted charge with external capacitance for for ring, 50 bar, 50 mesh and 100 mesh electrodes

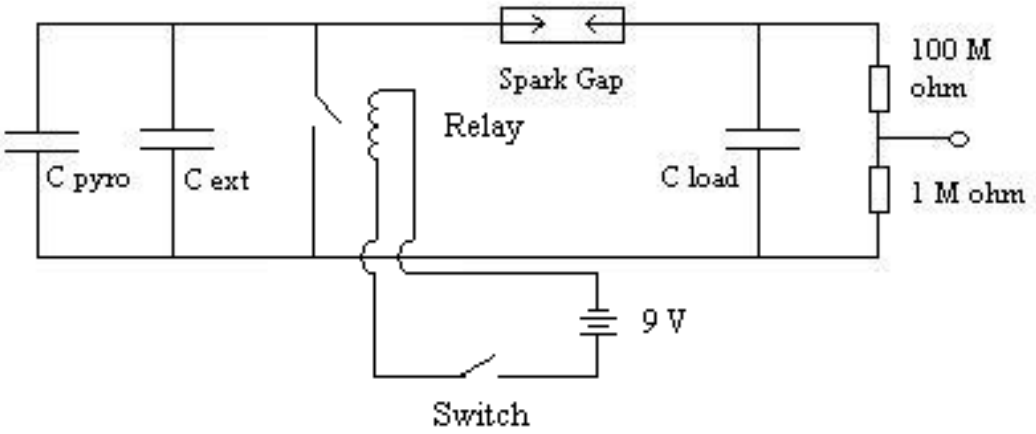

Figure 5.13: The usual pulse/FEE circuit modified to include the grounding relay.

5.2.7 Repeated firing

Since the voltage on the pulsing system does not fall to 0 V after an emission event, and is in fact typically several hundred volts it was proposed that this remaining charge on C_{Ext} could be put to use for a second emission event within a single run by continuing to heat the system. This was found to be possible, and an additional temperature change of around half of the initial temperture change was found to be sufficient.

5.3 Conclusions

This section has shown that pyroelectric materials may be used to generate high voltage pulses when combined with a suitable switching devices. Further, these pulses can be applied to a ferroelectric cathode (with the condition of

the cathode having a suitable capacitance) to trigger ferroelectric electron emission. This triggering mechanism has the advantage of allowing the analysis of the time profiles in a way not previously seen. Study of these time profiles with differing pulse paremeters allows differences in the emission process to be observed. It is shown that when a pulse is applied to the rear electrode the only component of emission is that associated directly with the plasma. However, when a pulse is applied to the front electrode it is shown that the plasma is in direct contact with the pulsing system. This causes significant differences in the emission process: a negative pulse absorbs positive charge from the plasma, thus increasing electron emission charge, while a positive pulse removes electrons from the plasma preventing any emission. The use of several electrode patterns shows that the emission process varies little with the electrode type with a negative pulse applied to the front electrode. This further supports the view that in this configuration the plasmas main function is to provide a route for electrons from the pulse system to be emitted. This observation is consistent with four electrode patterns, and across a range of C_{Ext} from 50 pF to 122 pF. Thus it is shown that a negative pulse applied to the front electode is the best method for giving a large emission current and charge.

Chapter 6

Accelerated Ferroelectric Electron Emission

6.1 Acceleration by External Pulse Generator

This section of the project builds on the results from the previous section with the introduction of an acceleration voltage. This voltage is investigated to determine the effect it has on the peak current and charge of the emission system. The effect of a retarding voltage is also investigated to determine the energy spectrum of the emitted electrons. Finally the introduction of a diode into the cathode system is investigated as a method for improving emission characteristics.

6.2 Results

6.2.1 Energy Analysis

This section covers the use of a retarding DC voltage on the emitted electrons to determine their energy spectrum. The Farady cup was used to collect the emitted charges. A high voltage DC supply was connected to a grid behind the 5 mm diameter aperture of the FC to allow a retarding voltage of 0 V to -1000 V to be applied to the emitted electrons. The FC aperture was held 10 mm from the cathode. The results of this investigation are shown in Fig 6.1. This shows that all the collected electrons have an energy of less than around 700 eV, and that the energy spectrum is similar with or without a shunt diode connected in parallel with the cathode.

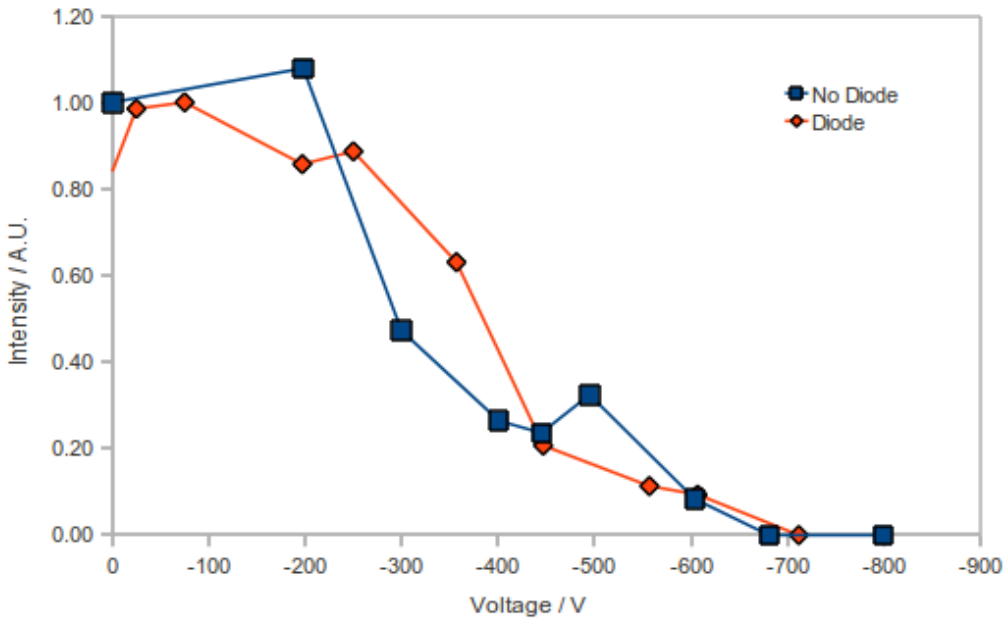

Figure 6.1: Electron energy spectrum of emitted electrons with and without the shunt diode

6.2.2 Acceleration by External Pulse Generator

6.2.2.1 System Voltages

This section looks at the behaviour of the pulsing and emission sections of the system simultaneously when a negative pulse is applied to the front electrode. A capacitive divider system is used to investigate the voltage of the pulsing system voltage, while the usual resistive divider system is used for the cathode system. Figure 6.3 shows the $V_{C_{ext}}$ and $V_{cathode}$ voltages with various V_{acc} . Figure 6.3a shows time profiles of $V_{C_{ext}}$ and $V_{cathode}$ with $V_{acc} = 0$ V. This shows that the pulse on the cathode is coincident with a drop of the voltage on C_{Ext} . Figures 6.3a to 6.3f show a pattern of the drop in $V_{C_{ext}}$ increasing with increasing V_{acc} . The voltage on is measured before and after emission, and the change in $V_{C_{ext}}$ calculated by subtracting the final voltage from the initial voltage. The change in $V_{C_{ext}}$ before and after the pulse varies from 600 V when $V_{acc} = 0$ V to 1395 V and 1320 V when $V_{acc} = 400$ V and 600 V. This is significant since it provides direct evidence for the transfer of charge from the pulsing system to the plasma. These same figures also show how the time profiles of the $V_{cathode}$ change with increasing V_{acc} . In all cases $V_{cathode}$ peaks at between 2000 V and 2500 V before rapidly falling to a steady level. It is the level to which it falls that is of particular interest in this case. When $V_{acc} = 0$ V $V_{cathode}$ falls to a steady value of -719 V, while with a V_{acc} of 600 V the voltage change on the cathode is so great that it becomes positive, settling at 507 V. These results are summarised in Table 6.1.

Figure 6.3 shows the results in Table 6.1 in graphical form. This shows that the change in the charge on the increases with increasing voltage, while the change in charge on the cathode 'dQ cat' begins negative (i.e the cathode is at 0 V before emisison and at a negative voltage after emission) and becomes positive

Table 6.1: Summary of system voltages results. V_{acc} is the accelerating voltage, I_{col} is the peak collected current, Q_{col} is the collected charge, ΔQ_C is the change in charge on the , $\Delta Q_{cathode}$ is the change in charge on the cathode and Q_{emit} is the calculated emitted charge.

V_{acc} / V	I_{col} / mA	Q_{col} / nC	ΔQ_C / nC	$\Delta Q_{cathode}$ / nC	Q_{emit} / nC
0	-33.3	-19.1	-43.8	-24.5	-19.4
100	-43.0	-24.6	-75.8	-20.2	-55.6
200	-55.0	-26.9	-80.3	-19.1	-61.2
300	-74.0	-32.5	-83.4	-16.0	-67.4
400	-90.7	-57.4	-101.8	2.8	-104.6
600	-106.5	-88.3	-96.4	17.2	-113.6

with increasing acceleration voltage. Combining these two values gives the total emitted charge. The collected charge is also shown.

The positive voltage on the cathode at the end of emission in Figs. 6.3e and 6.3f, and the 'dQ cat' plot in Fig 6.3 suggest that the emission of electrons will be lessened with at and above these voltages due to the decelerating effect that a positive voltage on the cathode will have on emitted electrons. This positive voltage will also reduce the energy of the emitted electrons at high acceleration voltages. Since both of these effects are undesireable it was proposed that a high voltage diode placed in parallel with the cathode may be useful. This diode would allow a negative voltage on the cathode, so the triggering pulse may be applied. However, the positive swing of the cathode voltage with higher acceleration voltages would be prevented since electrons may flow into the surface plasma from ground. This will not only prevent a positive voltage appearing on the cathode, but also replenish emitted electrons so that more are available for emission. The next sections of this thesis will investigate the use of this shunt diode.

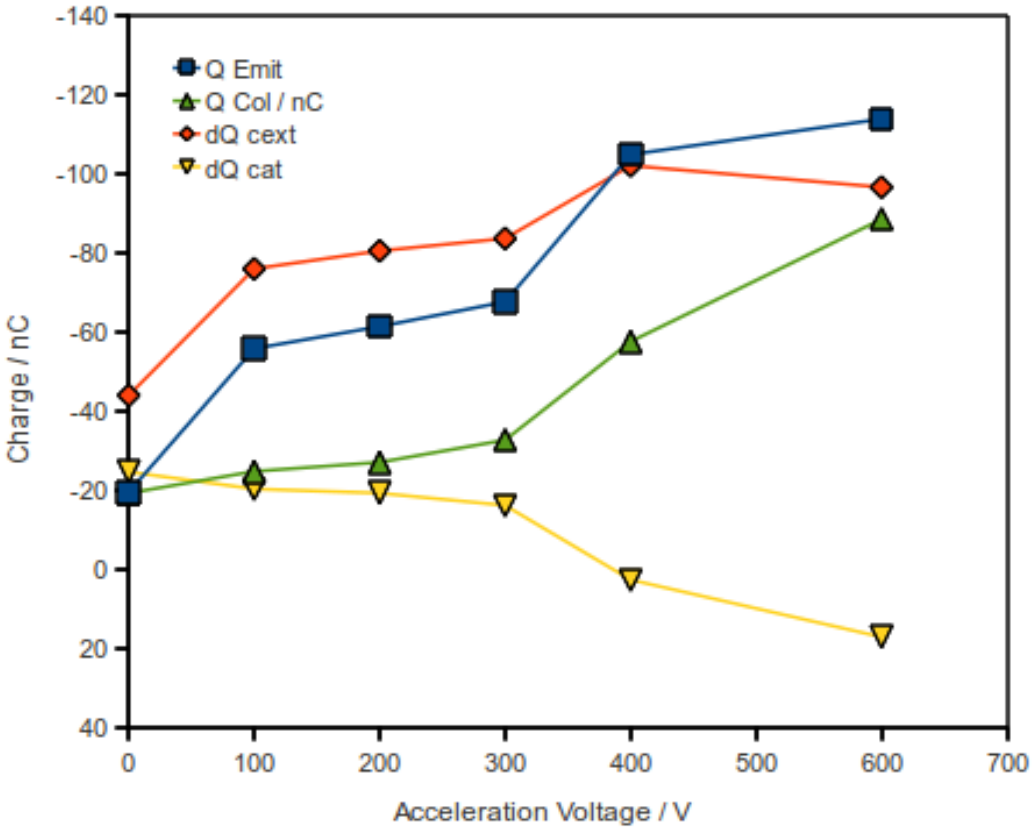

Figure 6.2: Summary of charges on various components of the emission system with various acceleration voltages

6.2.2.2 Acceleration Voltage and Emitted Charge and Current

This series of experiments shows the relationship between acceleration voltage and peak collected current and total collected charge. The effect of the shunt diode is also shown. Figure 6.4 shows the relationship between the acceleration voltage and the peak collected current with and without a shunt diode. This shows the general trend of increasing peak current with incrasing acceleration voltage. Figure 6.4 also shows that for all acceleration voltages the system with the shunt diode emits a greater value.

Figure 6.5 shows the total charge collected with various acceleration voltages. Again a similar trend is shown with this data, with a general increase of collected

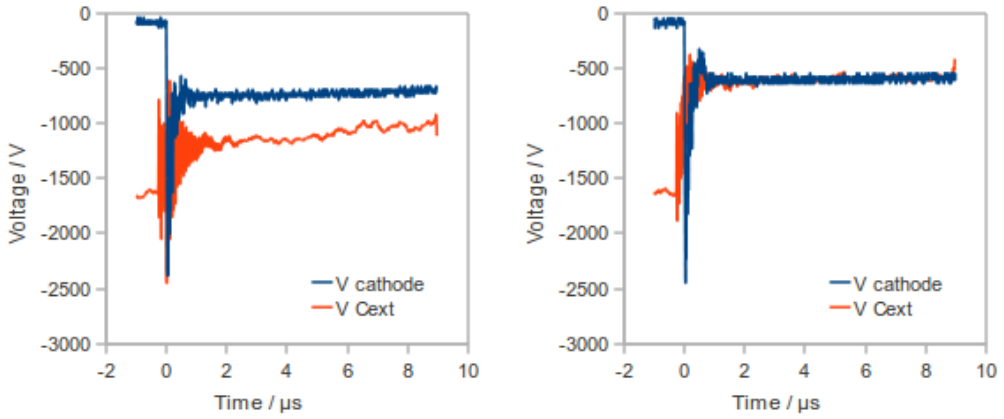

(a) $V_{acc} = 0$ V

(b) $V_{acc} = 100$ V

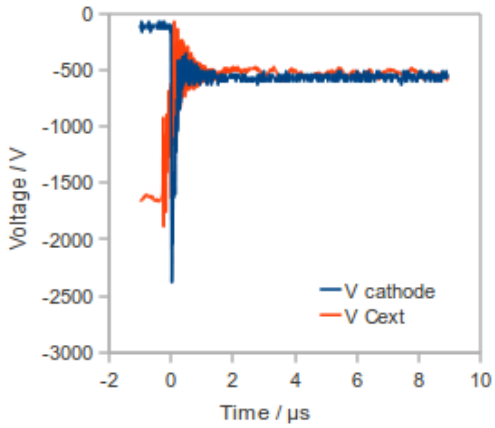

(c) $V_{acc} = 200$ V

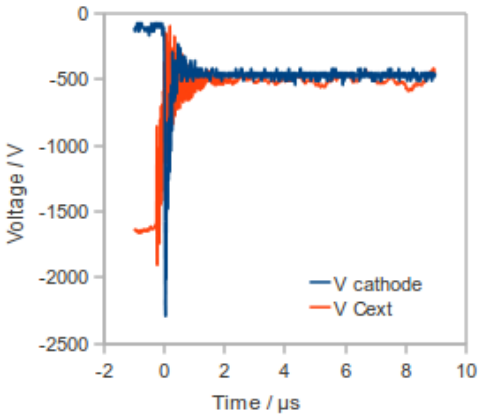

(d) $V_{acc} = 300$ V

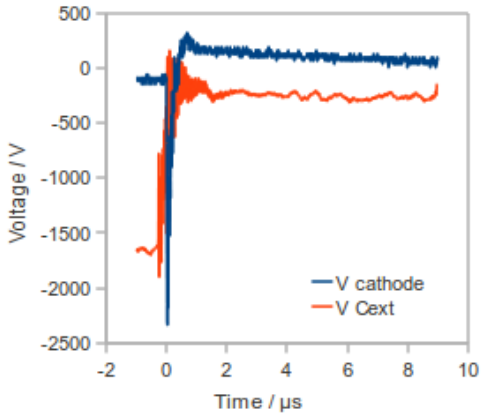

(e) $V_{acc} = 400$ V

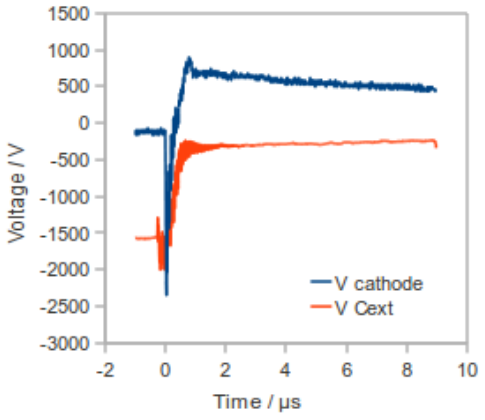

(f) $V_{acc} = 600$ V

Figure 6.3: Time profiles of the cathode and C_{Ext} voltages at various acceleration voltages.

Table 6.2: Summary data for accelerated pyroelectric electron emission using the external acceleration system, no shunt diode. V_{acc} is the acceleration voltage, E_{acc} is the electric field strength, ΔT is the change in temperature of the pyro crystal, I_{peak} is the peak collected current and Q_{col} is the total collected charge.

V_{acc} / V	E_{acc} / Vmm^{-1}	ΔT / K	I_{peak} / mA	Q_{col} / nC
0	0	20.4	-12.5	-3.9
93	9.3	20.3	-18.6	-7.6
227	22.7	19.2	-40.1	-28.7
425	42.5	19.2	-55.0	-27.0
678	67.8	18.8	-77.6	-37.9
861	86.1	19.8	-82.4	-40
1243	124.3	21.7	-95.0	-72.3
1610	161.0	21.1	-99.4	-88.9

Table 6.3: Summary data for accelerated pyroelectric electron emission using the external acceleration system, with shunt diode. V_{acc} is the acceleration voltage, E_{acc} is the electric field strength, ΔT is the change in temperature of the pyro crystal, I_{peak} is the peak collected current and Q_{col} is the total collected charge.

V_{acc} / V	E_{acc} / Vmm^{-1}	ΔT / K	I_{peak} / mA	Q_{col} / nC
0	0	18.3	-22.1	-11.1
121	12.1	19.6	-32.4	-10.4
254	25.4	19.8	-50.7	-25.9
439	43.9	19.6	-73.3	-30.3
656	65.6	19.1	-87.8	-55.8
894	89.4	21.4	-100.0	-76.1
1030	103.0	19.6	-143.0	-83.5

charge with increasing acceleration voltage. A greater collected charge is also seen with the shunt diode when compared to the system without.

6.2.3 Emission Process

Figure 6.6 shows a special case of the negative pulse front electrode system, where a positive voltage is applied to the anode to accelerate the electrons. The

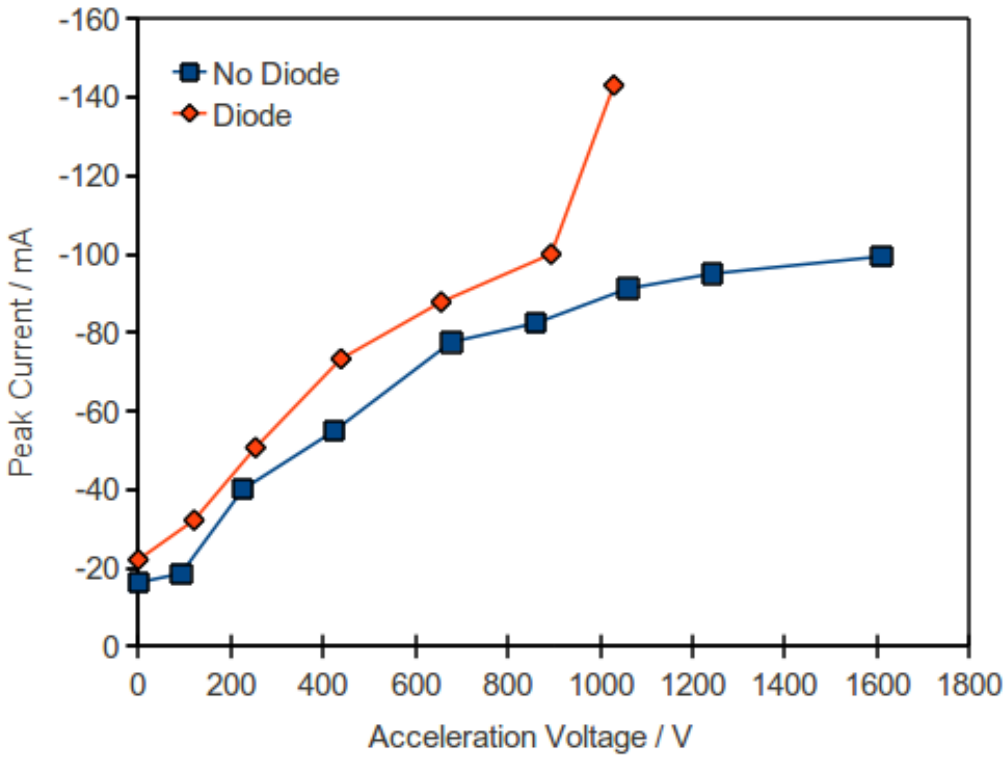

Figure 6.4: Peak current vs acceleration voltage with and without a shunt diode.

initial stages of the process are the same with and without the acceleration voltage, and shown in figures 6.6a to 6.6c. After this point the process changes, with a rapid fall in the cathode voltage in figure 6.6d as positive charges are withdrawn from the plasma. In Figure 6.6e the cathode voltage reverses as the external electric field continues removing screening electrons from the plasma. Thus the voltage on the cathode now becomes positive as a result of the accelerating field acting on the plasma. Higher accelerating voltages result in higher positive voltages in the cathode. The electron charge remaining on the cathode is dependent on the external voltage, as shown in figure 6.6f, with the final state of the system beign shown in figure 6.6g. This final state shows a positive voltage being present on the cathode when a negative voltage was used to trigger the emission process.

Figure 6.7 shows the system behavior when both an acceleration voltage and

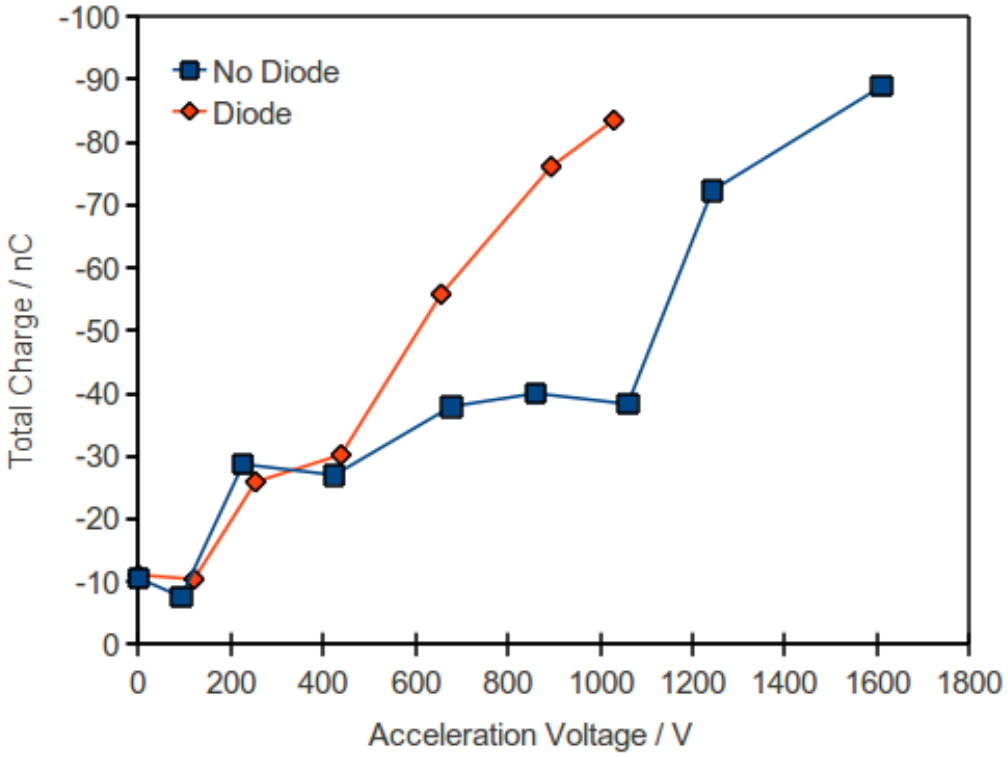

Figure 6.5: Total charge vs acceleration voltage with and without a shunt diode.

the shunt diode are used. The initial parts of the emission process (Fig. 6.7a to Fig. 6.7d) are the same as when no diode is present (Fig. 6.6a to Fig. 6.6d). After this point, when without the shunt diode the voltage on the cathode would become positive, electron conduction begins through the diode to compensate any positive ions on the grid electrode. Therefore the voltage on the front surface of the cathode is maintained around 0 V (Fig. 6.7e to Fig. 6.7g).

6.2.4 Anode Size

This section will look at the effect of anode size on the peak current and total charge collected during emission. Various circular anodes of diameter 0.6, 3, 5, 7, 8 and 12.5 mm were used. The anodes were always placed at 10 mm from the cathode. The experimantal procedure was the same as previously used in

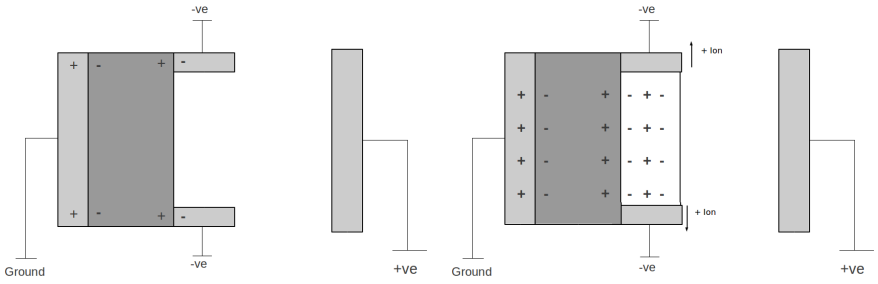

(a) Pulse applied

(b) Plasma forms

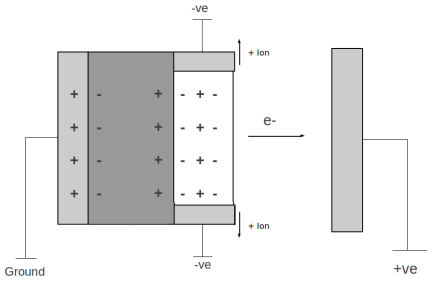

(c) Electron emission begins

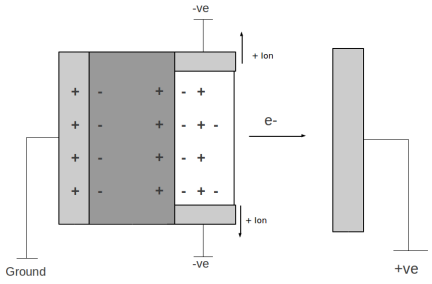

(d) Cathode voltage reduces

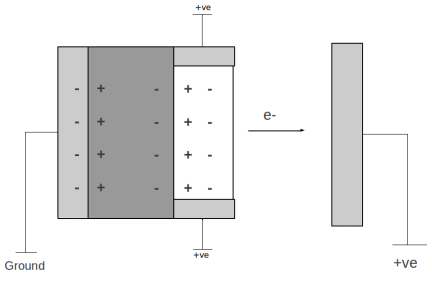

(e) Cathode voltage reverses

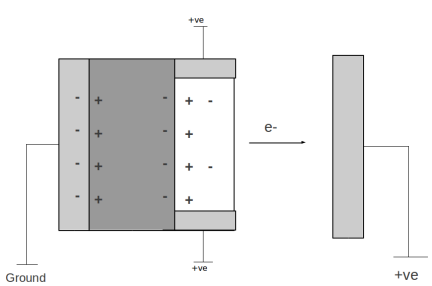

(f) Electron emission ends

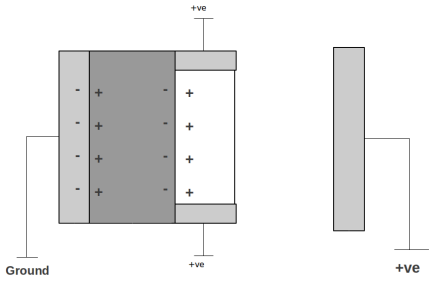

(g) Process completed

Figure 6.6: Schematic of the process when a negative pulse is applied to the front electrode by the pyro pulse generator, with an external acceleratiopn voltage

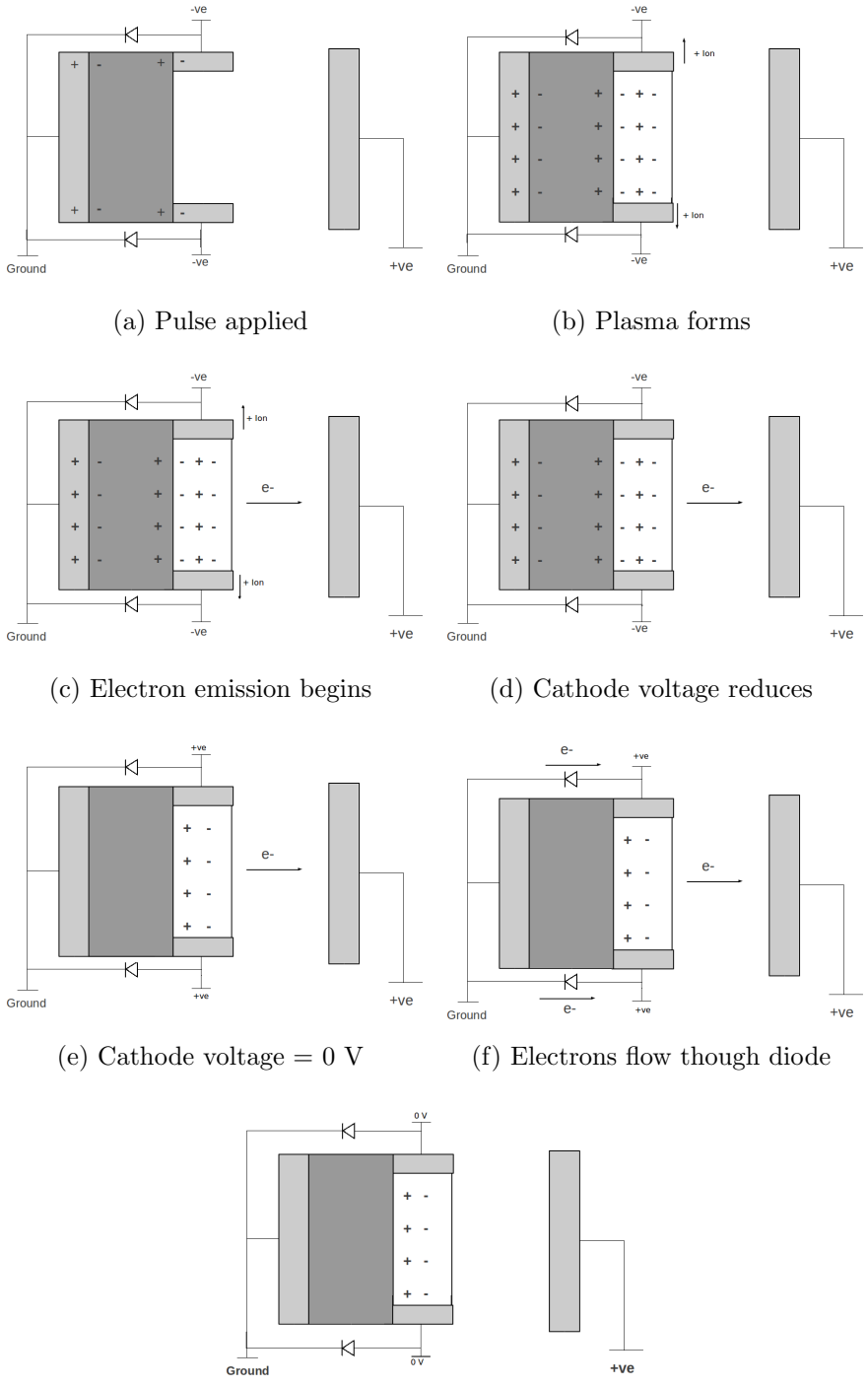

(a) Pulse applied

(b) Plasma forms

(c) Electron emission begins

(d) Cathode voltage reduces

(e) Cathode voltage = 0 V

(f) Electrons flow though diode

(g) Process completed

Figure 6.7: Schematic of the process when a negative pulse is applied to the front electrode by the pyro pulse generator, with an external acceleration voltage and with shunt diode

all accelerated FEE experiments. The results are shown in Figs. 6.8 and 6.9. Figure 6.8 shows that the current density varies greatly with both anode size and acceleration voltage. A decrease in current density with anode size is shown across all accleration voltages. With greater acceleration voltages the a greater peak current is seen at all anode sizes. A similar trend in seen in Fig 6.9 for charge densities with various anode sizes and acceleration voltages. From these results it can be noted that the electron beam produced by the ferroelectric cathode is highly divergent, as shown by the large drop in peak current and charge with increasing anode diameter. The focussing of the electron beam by the accelerating field is also readily apparent from the greater currents and charges across the anode size range with increasing acceleration voltage.

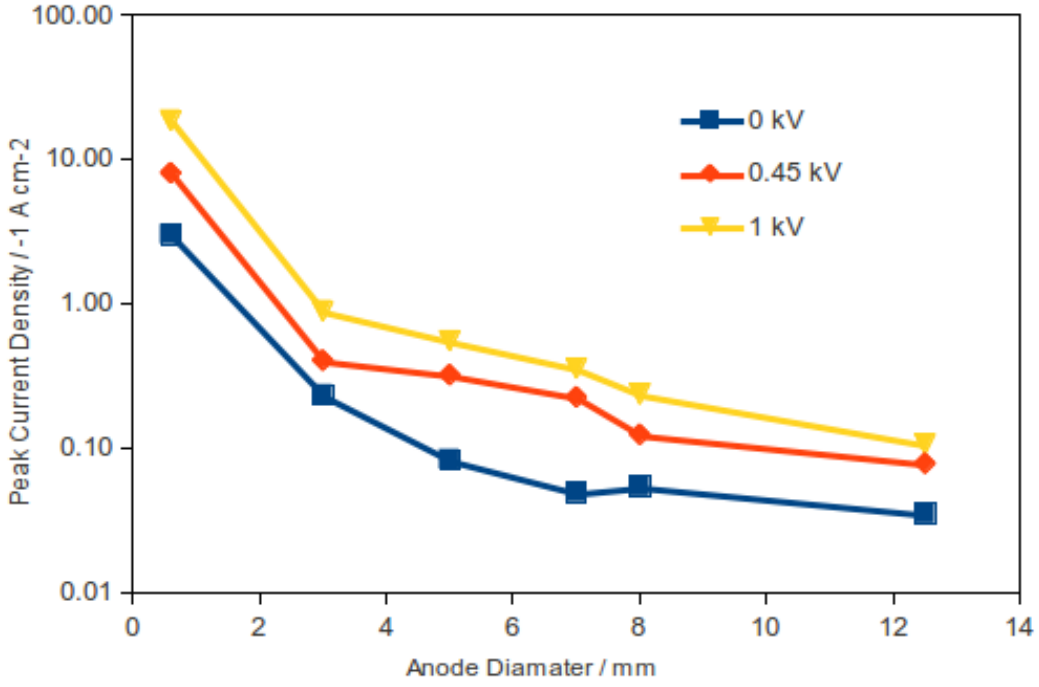

Figure 6.8: Peak current density at the anode with various acceleration voltages and anode sizes

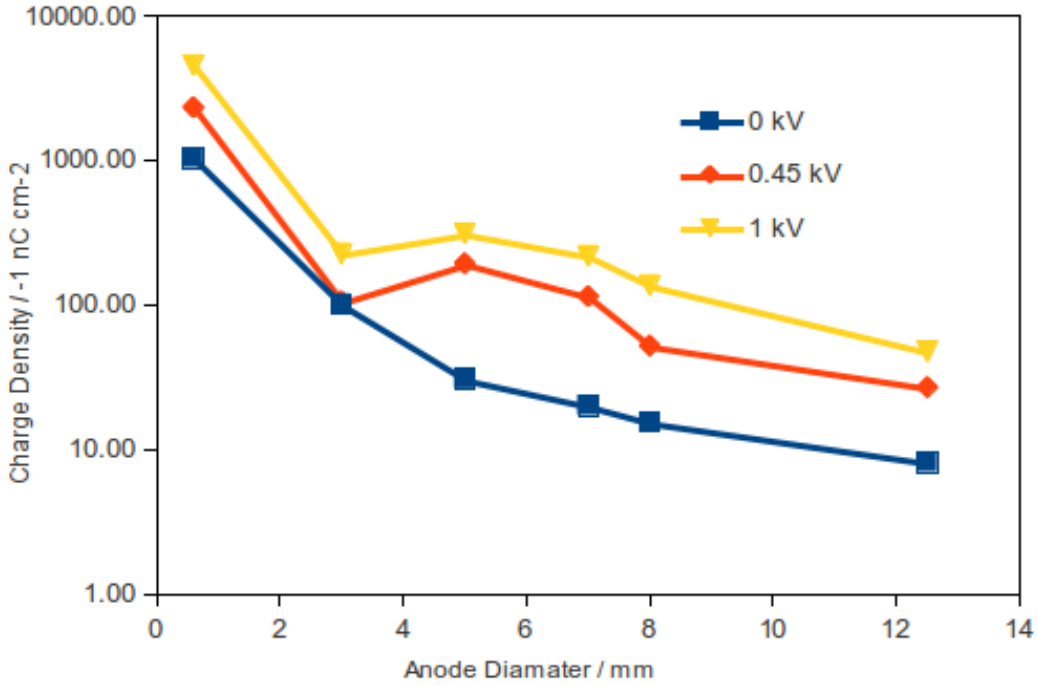

Figure 6.9: Charge density at the anode with various acceleration voltages and anode sizes

6.3 Conclusions

This chapter has shown that the pyroelectric pulse system can be expanded to generate an electron beam which can then be accelerated using an external acceleration system. Investigations of the time profiles of the collected charge and cathode voltage $V_{cathode}$ shed further light on the emission mechanism. This information is then used to implement a method for improving the collected charge and peak current for a given system. This method involved the use of a diode connected in parallel with the cathode. This shunt diode allows electrons to flow towards the cathode when the cathode voltage becomes positive, thus compensating positive charges. Therefore, more electrons are avaliable for emission from the plasma since they are not compenstaing positive ions in the plasma.

Chapter 7

Pyroelectrically Accelerated Ferroelectric Emission

7.1 Introduction

This section of the project builds on the previous results using the external acceleration system, and modifies it to use a pyroelectric crystal as the element providing the accelerating voltage. This enables a system that can generate a pulsed electron beam, and accelerate it using only a low power (15 V, 3 A i.e. 45 W) power supply. This is in contrast to most similar systems which require a high voltage power supply, which is usually bulky. This is similar to the Amptek Cool-X[8] device in that it can produce and accelerate an electron beam using only low power requirements.

In this section of the project the pyroelectric acceleration system is used to investigate the effect of the voltage on the accelerating element and the capacitance of the accelerating element. The effect of the external shunt diode is also

investigeated in each of these scenarios, which not only allows the optimum system to be determined, but also gives insight into the mechanism of FEE, particularly the role and behaviour of the surface plasma.

7.2 Results

7.2.1 Acceleration Capacitance

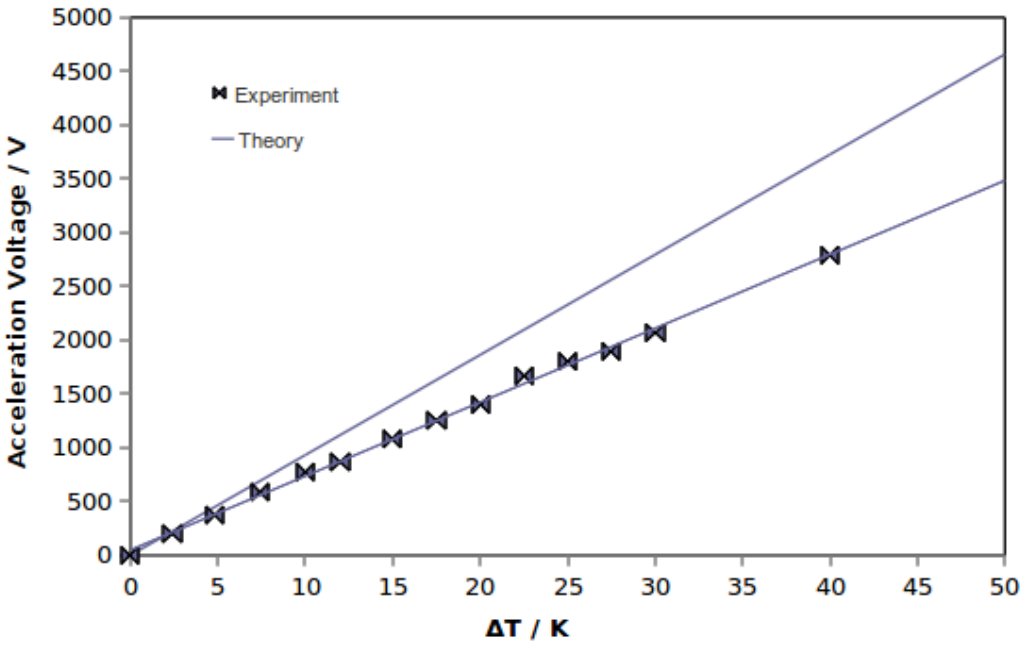

Figure 7.1: Experimental and theoretical pyroelectric acceleration voltage with a 50 pF C_{acc} .

Experiments were performed to investigate the voltage produced by the pyroelectric acceleration system. The results of this investigation with $C_{acc} = 50$ pF are shown in Fig. 7.1, and $C_{acc} = 10$ pF in Fig. 7.2. Experimental data

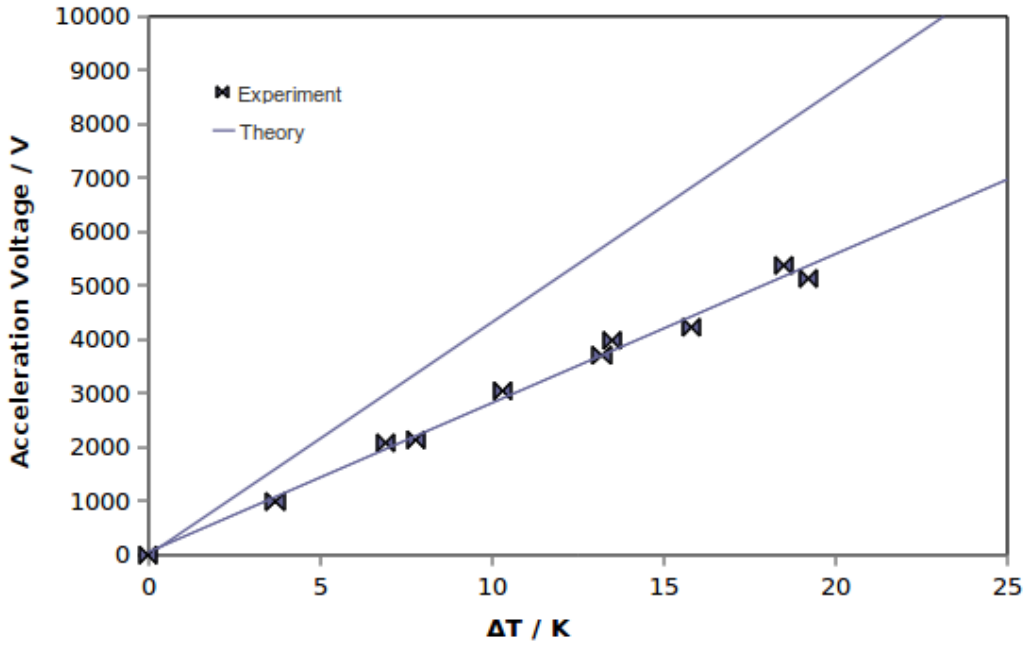

Figure 7.2: Experimental and theoretical pyroelectric acceleration voltage with a 10 pF C_{acc} .

points with linear fitting and theoretical data are shown. The theoretical data is calculated using a value for the pyroelectric coefficient of of -1.9 $Cm^{-2}K^{-1}$[11]. The theoretical values of the acceleration voltage are consistently larger than the experimental values, and observation which is consistent with either a lower value of the pyroelectric coefficient or the presence of stray capacitance.

From the experimental data the gradient of the fitting line is found to be 68.7 with $C_{acc} = 50$ pF and 276.7 with $C_{acc} = 10$ pF. These values allow the calculation of the acceleration voltage from the measured temperature of the crystal. It was necessary to determine the relationship between voltage and temperature this way, rather than direct measurment during emission runs due to the unacceptable noise levels caused by the voltage follower with fast signals.

7.2.2 Emitted Charge

This section shows the resutls of pyroelectrically triggered FEE using a pyroelectric acceleraiton system. Several configurations are used in this section. Two acceleration capacitances C_{acc} are used: 10 pF and 50 pF. Experiments with each of these values are conducted with and without a shunt diode in place, resulting in a total of four configurations. The results in each of these confrigurations is shown in tables 7.1 to 7.4. Each of these sets of resutls shows a general increase in the collected charge with increasing V_{acc} . The specifics of each case differ however and will be discussed below. Table 7.1 shows the results with a C_{acc} of 50 pF and no shunt diode. The collected charges range from -2.6 nC with V_{acc} = 0 V to -45.0 nC with V_{acc} = 2206 V. Table 7.2 shows that the collected charges range from -3.2 nC at V_{acc} = 0 V to -45.6 nC at V_{acc} = 1174 V with a 50 pF C_{acc} and a shunt diode. Table 7.3 shows that the the collected charges range from -2.7 nC at V_{acc} = 0 V and -40.9 nC at V_{acc} = 5021 V with C_{acc} = 10 pF and no shunt diode. Table 7.4 shows that the collected charge ranges from -3.0 nC at V_{acc} = 0 V to -41.3 nC at V_{acc} = 5077 V.

Figure 7.3 shows the reults detailed in Table 7.1 to 7.4 graphically. Figure 7.3a shows a comparison of the collected charges at various voltages with and without the shunt diode with C_{acc} = 50 pF. This clearly shows that the collected charge is greater when the shunt diode is used for all by the lowest few values. Also of note is the roughtly linear trend of the data when the shunt diode is used, while without the shunt diode the trend levels off as V_{acc} increases.

Figure 7.3b shows the data with a 10 pF C_{acc} . In this case there appears to be no difference between the data with and without the diode, with both cases showing nearly identical values for collected charge across the entire range of V_{acc} , as well as both showing a linear trend to the data.

The different results for the different configurations are explained by the differing electrical conditions in each set up, in particular by considering which section (anode or cathode) has the greatest charge avaliable. In the case of $C_{acc} = 50$ pF with no diode the charge avaliable for emission is simply that available due to usual plasma emission and injection from the pulsing system. Injection from the pulsing system will be limited due to V_{acc} decreasing as electrons are collected. This suggests that the charge avaliable for emission from the cathode is the limiting factor in this case. In the case of a 50 pF C_{acc} with a shunt diode the electrical condition is different. As long as there is a positive voltage on the anode and plasma exists on the cathode then electrons may be emitted due to replenishment of the electron supply through the diode. This results in the cathode having an (effectivly) infinte supply of electrons, while the anode has a limited supply. Therefore the limiting factor in this case is the supply of charge on the anode. This explains the differing characteristics of the two systems. Since the charge collected by the system with the diode is determined mostly by the charge on the anode C_{acc} the increase of collected charge should be linear, as is observed. Since the limiting factor without the diode is largely the 'focussing' of the electron beam by the accelerating field it would be expected that the collected charge would level off as the voltage incrases, which is again what is observed.

In the case of the two systems with $C_{acc} = 10$ pF the electrical condition is again different due to the significant difference in C_{acc} an C_{Ext} . The result of this is that either with or without the shunt diode the dominant source of charge is the cathode . This means that the shunt diode should have little or no effect, since the charge present on the cathode is already more that the anode can collect. Again this is what is observed.

Table 7.1: Results of the investigation into the effect of the pyro acceleration voltage with a 50 pF C_{acc} with no shunt diode. ΔT_{acc} is the temperature change of the accelerating crystal, ΔT_{pulse} is the temperature change of the voltage pulsing crystal, V_{acc} is the accelerating voltage, Q_{col} is the collected charge, Q_{acc} is the accelerating charge, Q_{pulse} is the pulsing system charge, Q_{col}/Q_{acc} is the collected charge divided by the accelerating charge and Q_{col}/Q_{pulse} is the collected charge divided by the pulse charge.

ΔT_{acc} / K	ΔT_{pulse} / K	V_{acc} / V	Q_{col} / nC	Q_{acc} / nC	Q_{pulse} / nC	Q_{col}/Q_{acc} %	Q_{col}/Q_{pulse} / %
0	20.7	0	-2.61	0	-98.3	-	2.7
4.8	21.1	339	-11.2	22.8	-100.7	49.1	11.1
7.2	20.0	509	-18.3	34.2	-95.0	53.9	19.3
11.1	20.6	714	-19.0	48.0	-97.9	35.6	19.4
16.5	21.6	1167	-27.2	78.4	-102.6	34.7	26.5
20.0	20.3	1414	-35.0	95.0	-96.4	36.8	36.3
23.8	21.8	1683	-39.3	113.1	-103.6	34.9	38.1
31.2	22.8	2206	-45	148.2	-108.3	29.0	39.7

Table 7.2: Results of the investigation into the effect of the pyro acceleration voltage with a 50 pF C_{acc} with shunt diode. ΔT_{acc} is the temperature change of the accelerating crystal, ΔT_{pulse} is the temperature change of the voltage pulsing crystal, V_{acc} is the accelerating voltage, Q_{col} is the collected charge, Q_{acc} is the accelerating charge, Q_{pulse} is the pulsing system charge, Q_{col}/Q_{acc} is the collected charge divided by the accelerating charge and Q_{col}/Q_{pulse} is the collected charge divided by the pulse charge.

ΔT_{acc} / K	ΔT_{pulse} / K	V_{acc} / V	Q_{col} / nC	Q_{acc} / nC	Q_{pulse} / nC	Q_{col}/Q_{acc} %	Q_{col}/Q_{pulse} / %
0	19.2	0	-3.2	0	-91.2	-	3.5
2.2	21.9	156	-8.4	10.5	-104.0	81.2	8.2
4.6	19.9	325	-15.4	21.5	-94.5	70.5	16.3
6.0	22.6	424	-21.1	29.0	-107.4	74.0	19.7
8.5	20.6	601	-21.2	40.4	-97.9	52.5	21.7
10.6	20.8	749	-26.3	50.4	-98.8	52.2	26.6
12.7	21.6	848	-34.3	60.3	-102.6	56.9	33.4
15	22.1	1061	-35.2	71.3	-105.0	49.4	33.5
16.6	21.3	1174	-45.6	78.9	-101.2	57.8	45.1

Table 7.3: Results of the investigation into the effect of the pyro acceleration voltage with a 10 pF C_{acc} with no shunt diode. ΔT_{acc} is the temperature change of the accelerating crystal, ΔT_{pulse} is the temperature change of the voltage pulsing crystal, V_{acc} is the accelerating voltage, Q_{col} is the collected charge, Q_{acc} is the accelerating charge, Q_{pulse} is the pulsing system charge, Q_{col}/Q_{acc} is the collected charge divided by the accelerating charge and Q_{col}/Q_{pulse} is the collected charge divided by the pulse charge.

ΔT_{acc} / K	ΔT_{pulse} / K	V_{acc} / V	Q_{col} / nC	Q_{acc} / nC	Q_{pulse} / nC	Q_{col}/Q_{acc} %	Q_{col}/Q_{pulse} / %
0	20.6	0	-2.7	0	-97.9	-	2.8
2.5	20.0	701	-7.7	11.9	-95.0	64.8	8.1
4.3	20.4	1206	-11.7	20.4	-96.9	57.3	12.1
6.5	20.5	1823	-14.5	30.9	-97.4	47.0	14.9
9.2	21.1	2581	-23.2	40.7	-105.0	53.1	22.1
12.2	20.9	3422	-30.9	58.0	-99.3	53.3	33.1
14.1	20.7	3955	-32.0	67.0	-98.3	47.8	32.6
17.9	19.7	5021	-40.9	85.0	-93.6	48.1	43.7

Table 7.4: Results of the investigation into the effect of the pyro acceleration voltage with a 10 pF C_{acc} with shunt diode. ΔT_{acc} is the temperature change of the accelerating crystal, ΔT_{pulse} is the temperature change of the voltage pulsing crystal, V_{acc} is the accelerating voltage, Q_{col} is the collected charge, Q_{acc} is the accelerating charge, Q_{pulse} is the pulsing system charge, Q_{col}/Q_{acc} is the collected charge divided by the accelerating charge and Q_{col}/Q_{pulse} is the collected charge divided by the pulse charge.

ΔT_{acc} / K	ΔT_{pulse} / K	V_{acc} / V	Q_{col} / nC	Q_{acc} / nC	Q_{pulse} / nC	Q_{col}/Q_{acc} %	Q_{col}/Q_{pulse} / %
0	20.8	0	-3.0	0	-98.8	-	3.0
2.6	22.3	729	-5.8	12.4	-106.0	47.0	5.5
4.5	20.2	1262	-10.3	21.4	-96.0	48.2	10.7
6.7	18.4	1897	-19.2	31.9	-87.4	60.3	22.0
8.7	20.2	2440	-22.1	41.3	-96.0	53.5	23.0
12.2	22.3	3422	-29.9	58	-106.0	51.6	28.2
13.9	22.4	3899	-32.4	66	-106.4	49.1	30.5
18.1	21.3	5077	-41.3	86.0	-101.2	48.0	40.8

7.2.3 Comparison with External Acceleration System

A comparison of the results of accelerated emission with and without the shunt diode when using the external accelration system, $C_{acc} = 50$ pF and $C_{acc} = 10$ pF is shown in Fig. 7.4. Figure 7.4a shows the results with no diode. This clearly shows that the external acceleration system gives the greatest total charge across all V_{acc} values, with a greater difference being displayed with increasing V_{acc} . As previously noted the $C_{acc} = 50$ pF system performs better than the $C_{acc} = 10$ pF system. Figure 7.4b shows a similar trend for the system with the shunt diode. These results are explained by considering the capacitance of the accelerating element of the system. Since all of the acceleration systems are essentially variations of one system in that they are an anode connected to a capacitor. The major difference is the capacitance of this capacitor: in the external acceleration system the $C_{acc} = 14$ nF, as compared to 50 pF and 10 pF in the pyro system. The major consequence of this is that the charge on C_{acc} in the external system is so much greater than the collected charge that the voltage voltage on the C_{acc} is only negligily different before and after emission. In the pyro system the charge on the C_{acc} is similar to the collected charge so the voltage change is significant. It is this reduction of accelerating voltage during the charge collection that causes the variation in performance of the different systems.

7.2.4 Time Profiles

The time profiles of the pulse voltage and collected current are shown in the following section. These are important since they allow the process to be closely analysed with of each of the differing conditions. These differing electrical

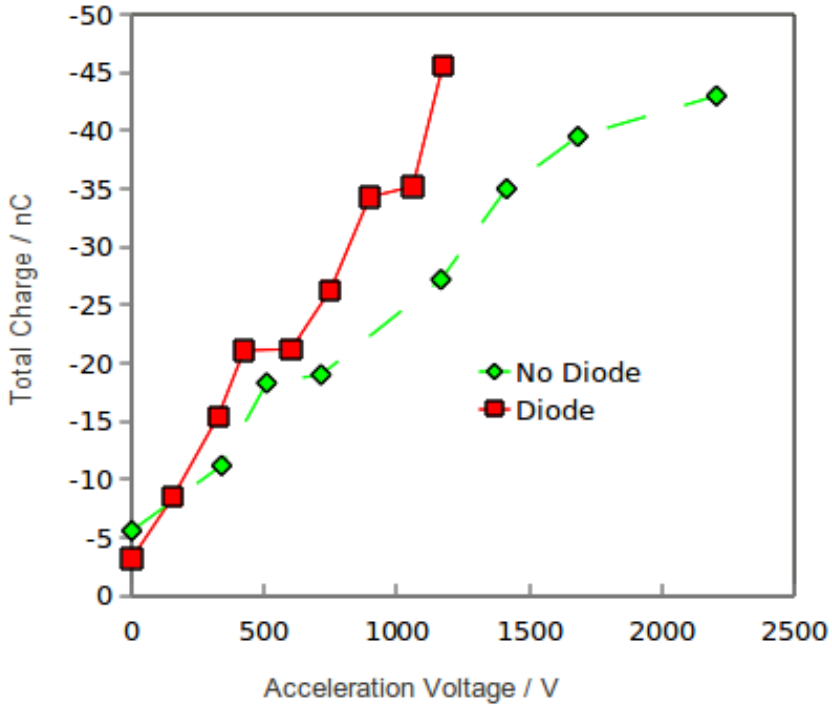

(a) $C_{acc} = 50$ pF

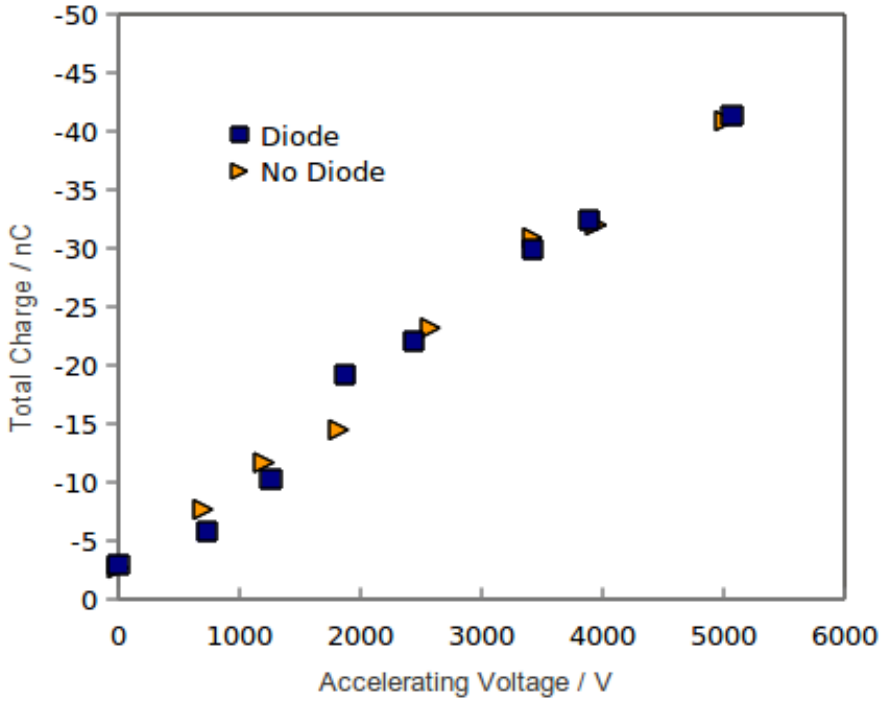

(b) $C_{acc} = 10$ pF

Figure 7.3: Acceleration voltage vs collected charge using various values of C_{acc} in the pyroelectric acceleration system, both with and without the shunt diode.

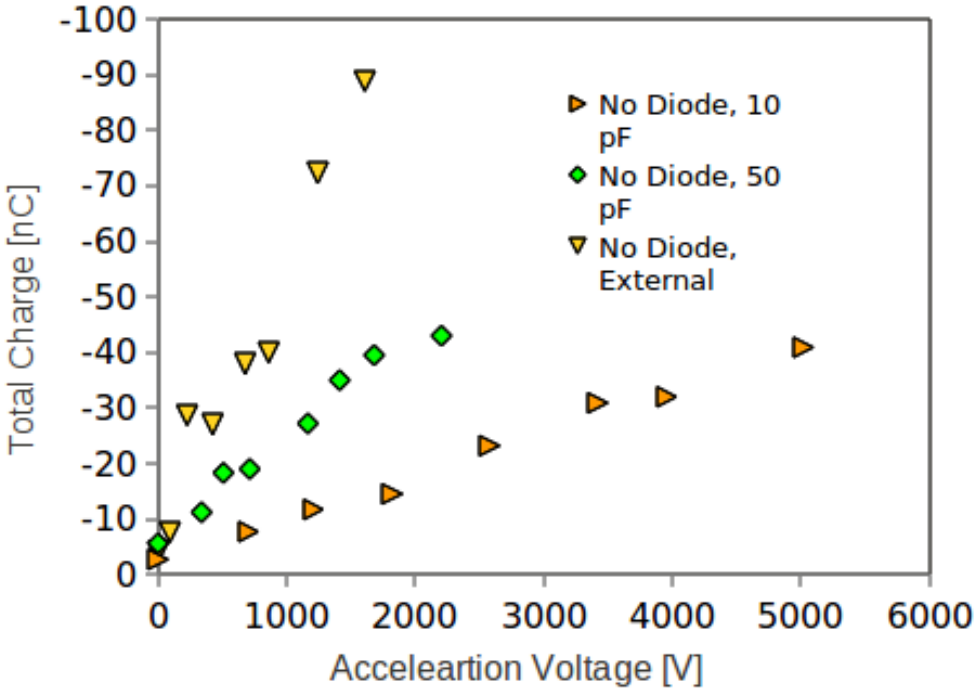

(a) Without shunt diode.

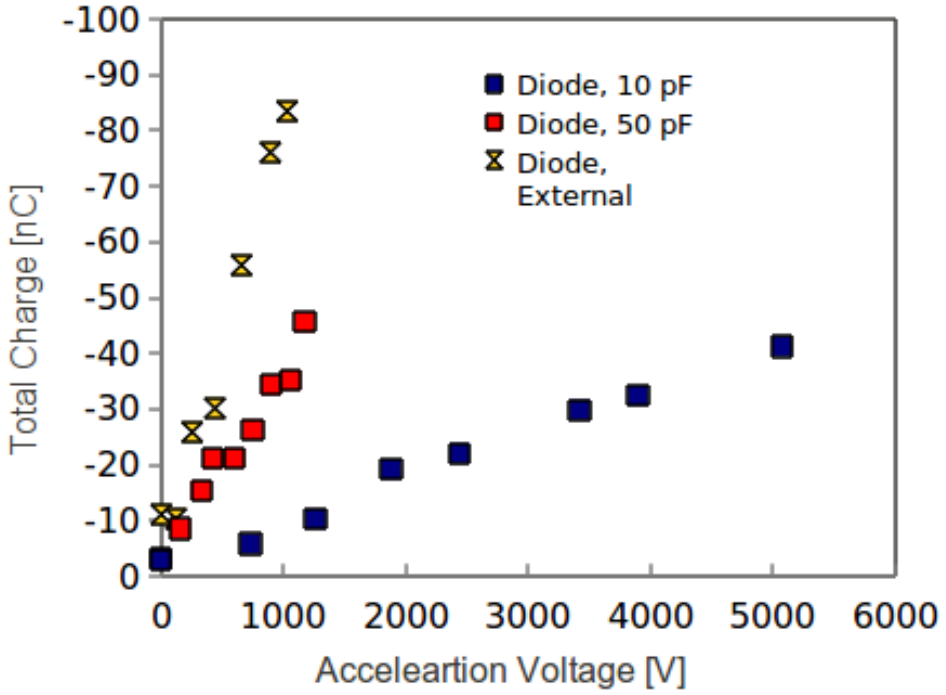

(b) With shunt diode.

Figure 7.4: Acceleration voltage vs collected charge for $C_{acc} = 10$ pF, $C_{acc} = 50$ pF and the external acceleration system, with and without the shunt diode.

conditions allow significant insight into the state of the plasma during the emission process.

7.2.4.1 C_{acc} = 50 pF, no diode

Figures 7.5 and 7.6 show the time profiles for the voltage on the cathode and the collected charge during the emission process, with various voltages generated by the pyro acceleration system using a 50 pF C_{acc} , without the shunt diode being used. The profiles of the charge simply show an increasing collected charge with increasing acceleration voltage, as shown in table 7.1. The time profiles of the voltage on the cathode however give useful inforamtion on the emission process. As the acceleration voltage increases the profile of the voltage on the cathode changes. Figure 7.5a shows the time profile with $V_{acc} = 0$ V. This shows the familiar profile of the pulse on the cathode: the pulse initially rises rapidly to a peak of a few thousand volts, and then drops rapidly. However, while the cathode voltage usually falls to around 0 V in this case it falls to around 1000 V. This is due to the difference in the acceleration system compared to the previous systems. Since this acceleration system has only a very limited capacitance even a small charge generates a significant voltage on it. This voltage which appears on the anode then generates a field opposing further collection of charges on the anode and further emission of charges from the cathode. This charge/voltage/field build up explains both the reduced collected charge when compared to the external acceleration system as well as the settling of the cathode voltage not falling to 0 V. As the acceleration voltage, and therefore the charge on C_{acc} increases the cathode voltage time profile changes. The initial peak remains similar, peaking at around a few kV, but falling to lower voltages as the acceleration voltage increases, with the cathode voltage falling to around 0 V in Figs 7.6b and 7.6c.

7.2.4.2 C_{acc} = 50 pF, with diode

Figures 7.7 and 7.8 show the time profiles for the collected charge and cathode voltage for the C_{acc} = 50 pF system with the shunt diode in place. Again the time profiles of the charge show an increase in collected charge with increasing V_{acc} . The time profiles for the voltage on the cathode are relatively similar to those seen in Fig. 7.5 and 7.6. There are however some important differences. The presence of the diode allows electrons to flow onto the cathode from ground, which under certain circumstances will result in greater emitted charge. Of particular note is the results above around 700 V. In this configuration the cathode voltage falls to around 0 V, so any further emission may come from the electrons drawn through the diode.

7.2.4.3 C_{acc} = 10 pF, no diode

Figures 7.9 and 7.10 show the time profiles for the collected charge and cathode voltage for the C_{acc} = 10 pF system with the shunt diode in place. Again the time profiles of the charge show an increase in collected charge with increasing V_{acc} . The time profiles for the voltage on the cathode a different trend to that seen in the other cases. Figure 7.11a shows a similar profile to that in the C_{acc} = 50 pF, no diode case (Fig 7.5a, however as the V_{acc} increases the trend differs. The profile remains similar for V_{acc} = 0 V to 2581 V, as shown in Figs. 7.5a to 7.10a. However, Figs. 7.10b to 7.10d show a significant decrease in the drop of the cathode voltage from its peak. This is due to the increasing V_{acc} drawing a greater charge onto the cathode from the C_{Ext} , as shown in Fig. 6.3. However, as V_{acc} decreases due to the collection of emitted charge on C_{acc} the emission of further charge form the cathode is prevented, thus causing the increasingly negative voltage observed on it at the end of emission.

7.2.4.4 C_{acc} = 10 pF, with diode

Figures 7.11 and 7.12 show the time profiles for the collected charge and cathode voltage for the C_{acc} = 50 pF system with the shunt diode in place. Again the time profiles of the charge show an increase in collected charge with increasing V_{acc} . The time profiles for the voltage on the cathode are again different to those previously seen. The voltage profiles do not appear to follow any particular trend in this case. This could be due to the very sensitive system using the diode. This may result in small differences in charge flows resulting in greatly differing time profiles in each case. For example, differences in the contribution to the cathode voltage from charge flow through the diode and charge transfer from the pulsing system (C_{Ext}). One consistent trend however is that in the case of a positive voltage being achieved the decay of the voltage to zero is much greater than when a negative voltage is present. This is due to charge flow through the diode, which cannot happen when a negative voltage is present.

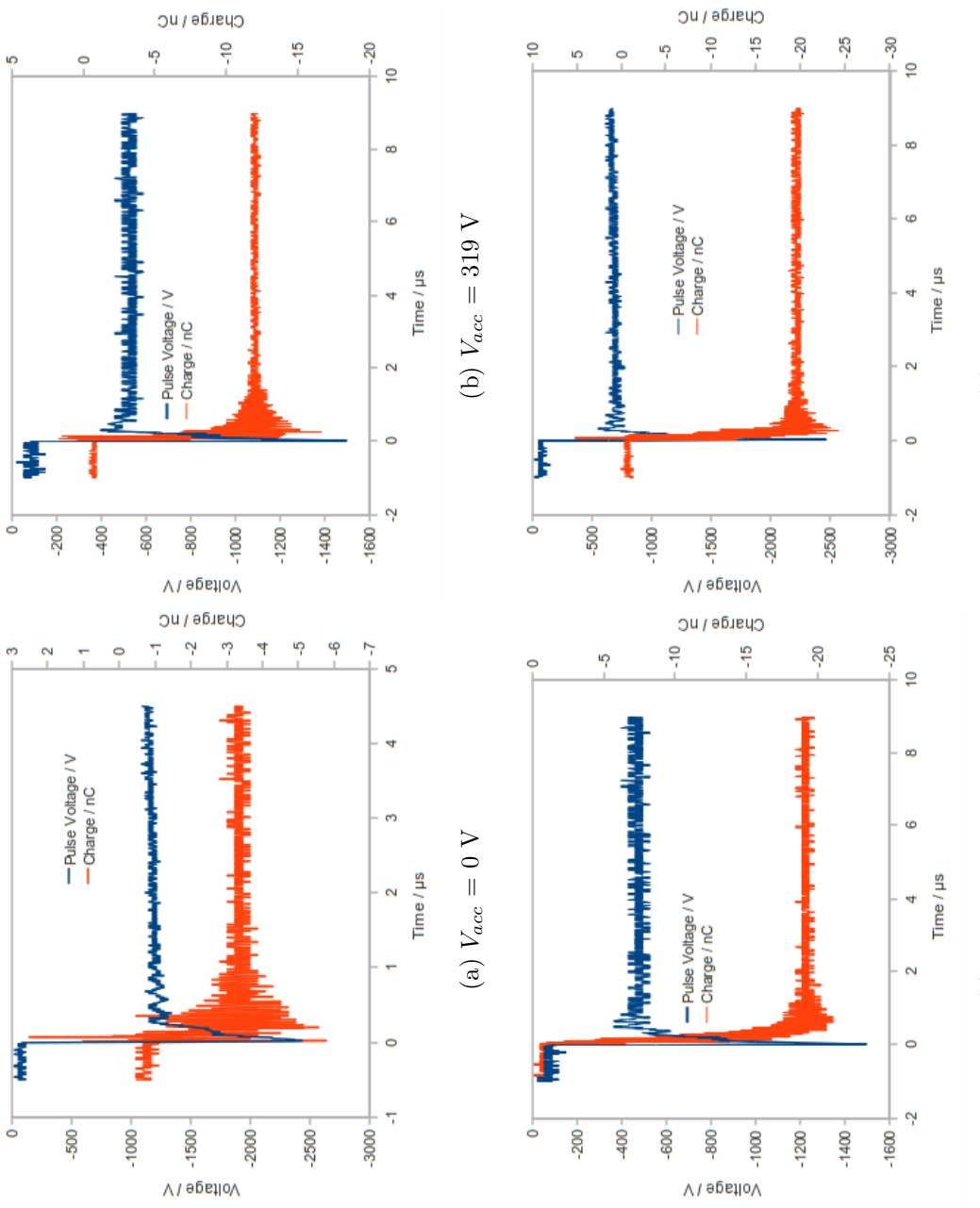

(a) $V_{acc} = 0$ V (b) $V_{acc} = 319$ V (c) $V_{acc} = 509$ V (d) $V_{acc} = 714$ V

Figure 7.5: Pulse voltage and emission current profiles for the pyro accelration system, 50 pF C_{acc} , no diode

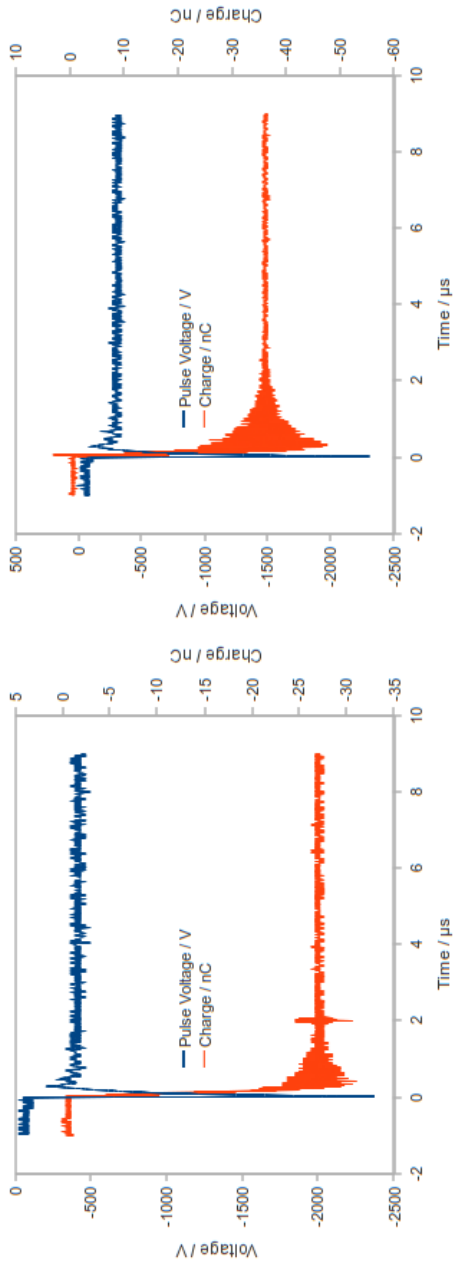

(a) $V_{acc} = 1167$ V

(b) $V_{acc} = 1414$ V

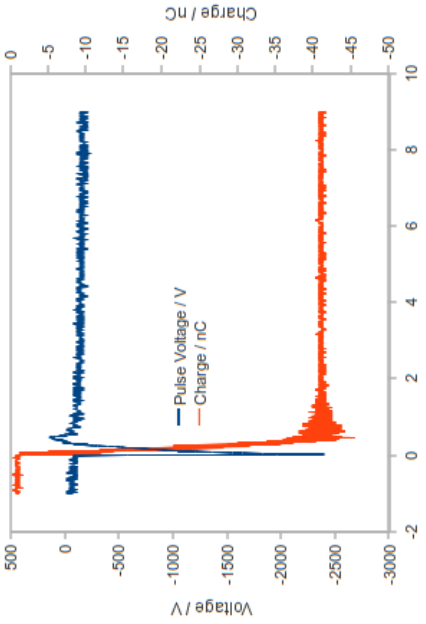

(c) $V_{acc} = 1683$ V

Figure 7.6: Pulse voltage and emission current profiles for the pyro accelration system, 50 pF C_{acc} , no diode

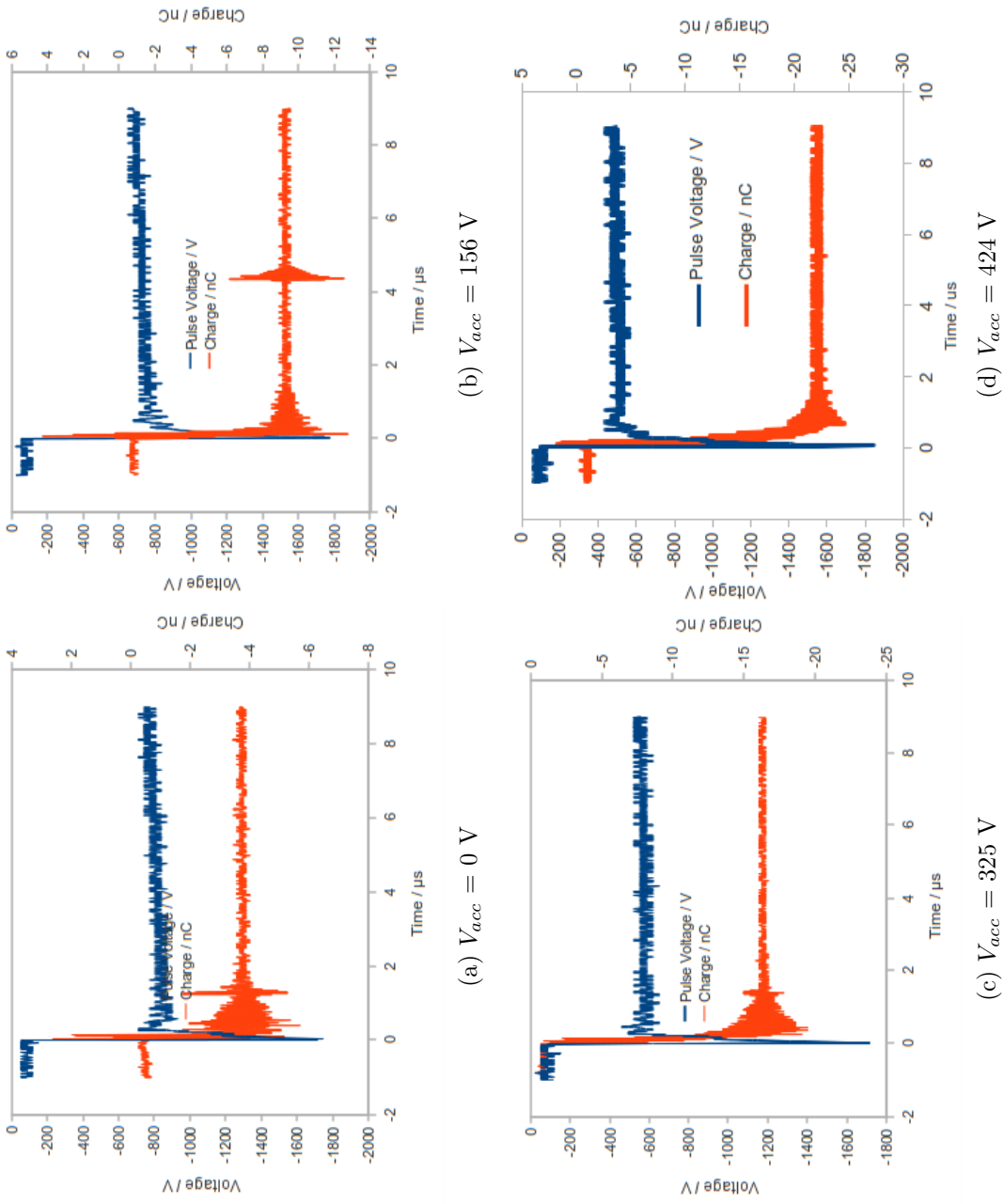

(a) $V_{acc} = 0$ V (b) $V_{acc} = 156$ V (c) $V_{acc} = 325$ V (d) $V_{acc} = 424$ V

Figure 7.7: Pulse voltage and emission current profiles for the pyro accelration system, 50 pF C_{acc} , diode

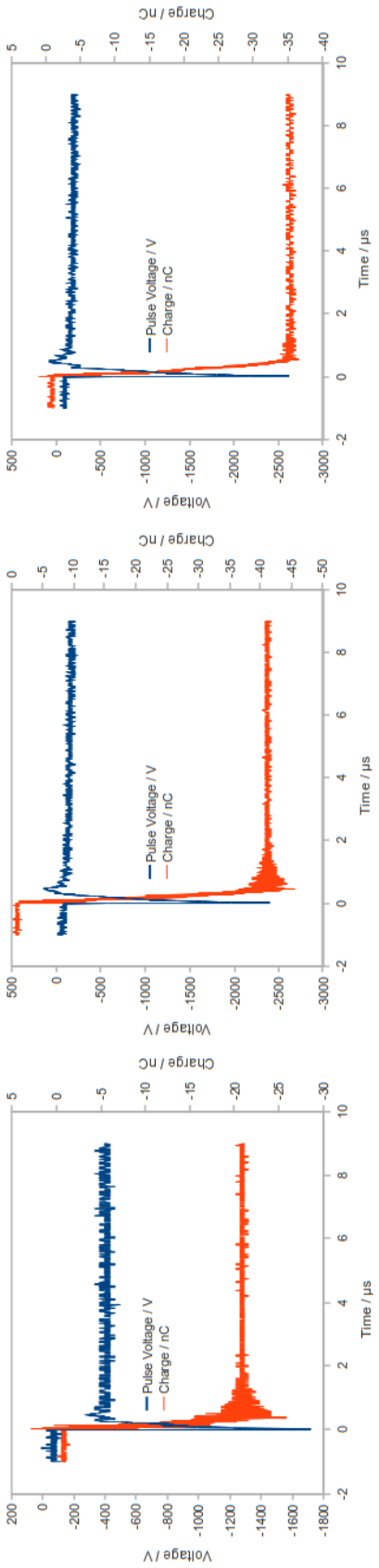

(a) $V_{acc} = 601$ V

(b) $V_{acc} = 749$ V

(c) $V_{acc} = 898$ V

(d) $V_{acc} = 1061$ V

(e) $V_{acc} = 1174$ V

Figure 7.8: Pulse voltage and emission current profiles for the pyro accelration system, 50 pF C_{acc} , diode

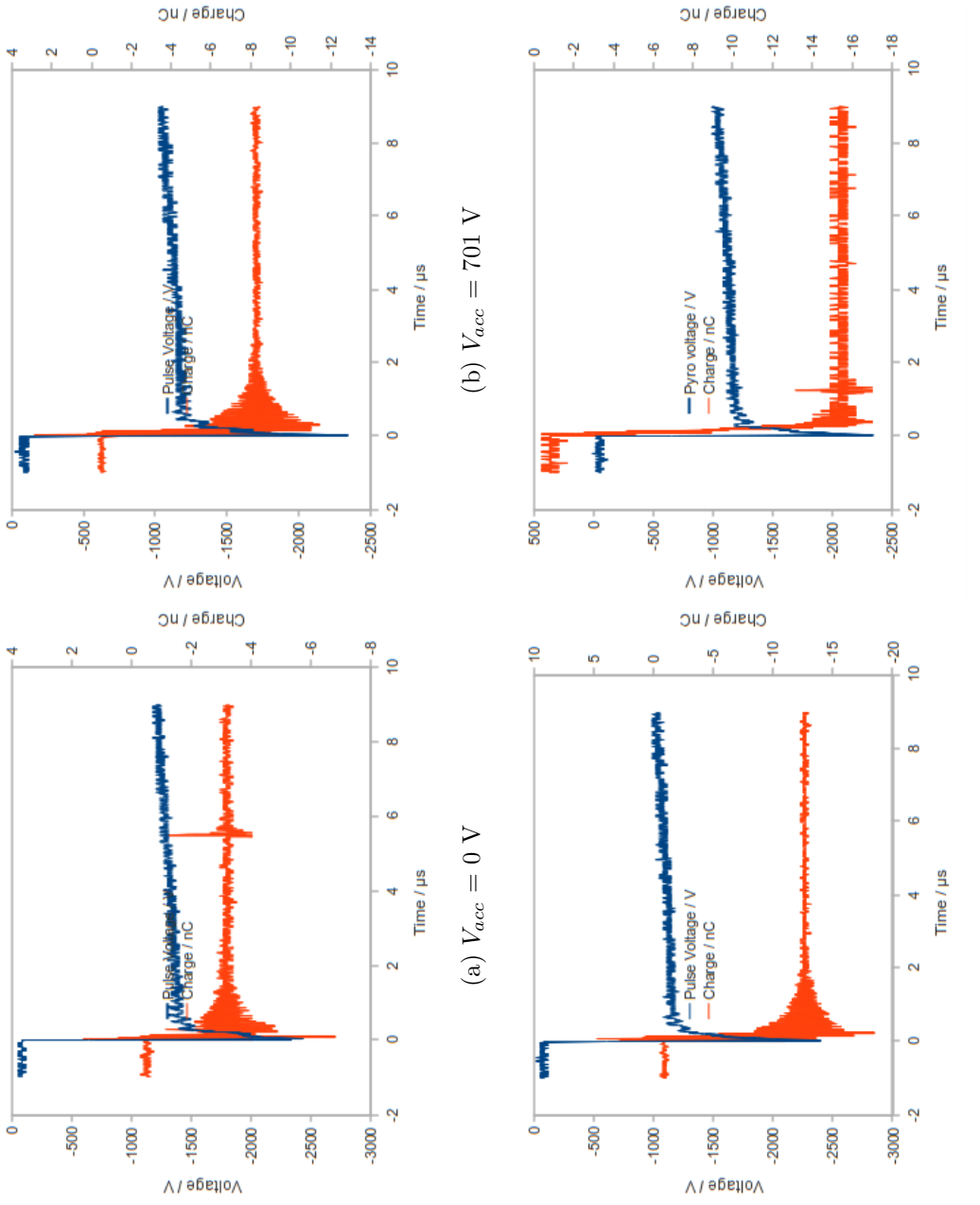

(a) $V_{acc} = 0$ V (b) $V_{acc} = 701$ V (c) $V_{acc} = 1206$ V (d) $V_{acc} = 1823$ V

Figure 7.9: Pulse voltage and emission current profiles for the pyro accelration system, 10 pF C_{acc} , no diode

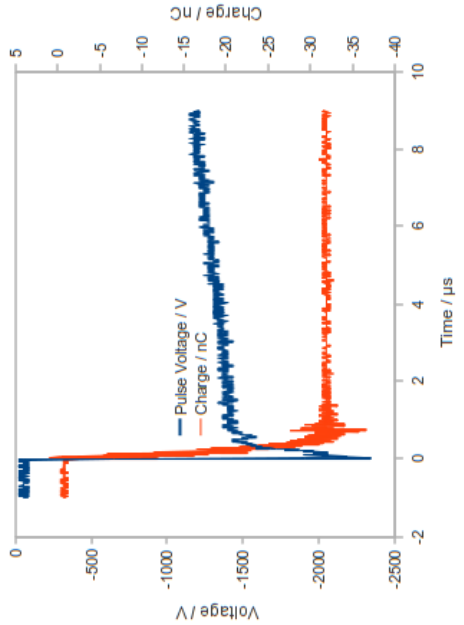

(a) $V_{acc} = 2581$ V

(b) $V_{acc} = 3422$ V

(c) $V_{acc} = 3955$ V

(d) $V_{acc} = 5021$ V

Figure 7.10: Pulse voltage and emission current profiles for the pyro accelration system, 10 pF C_{acc} , no diode

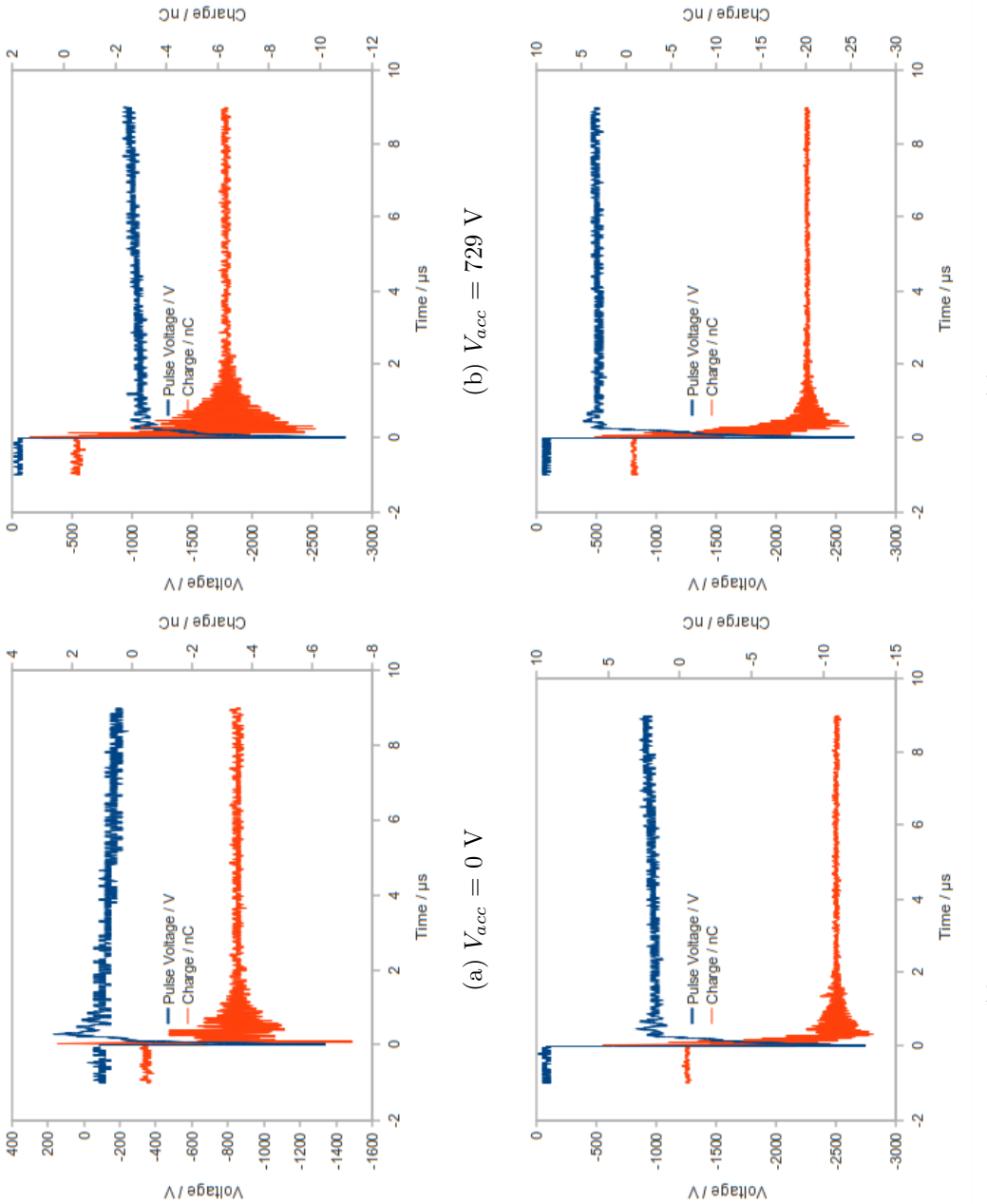

(a) $V_{acc} = 0$ V (b) $V_{acc} = 729$ V (c) $V_{acc} = 1262$ V (d) $V_{acc} = 1879$ V

Figure 7.11: Pulse voltage and emission current profiles for the pyro accelration system, 10 pF C_{acc} , diode

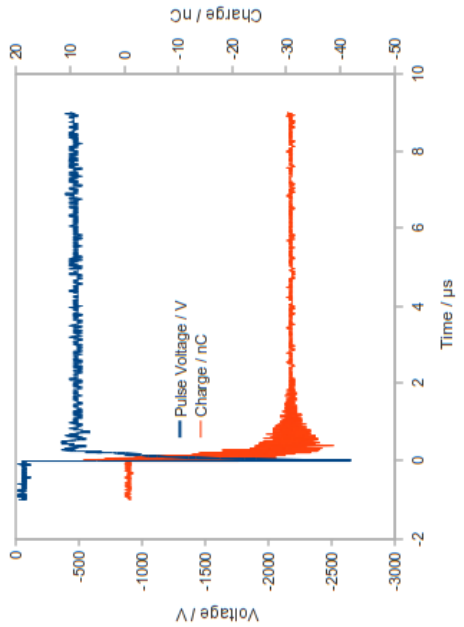

(a) $V_{acc} = 2440$ V

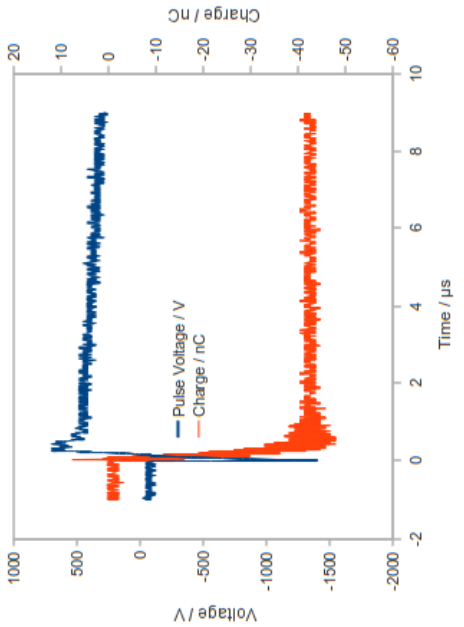

(b) $V_{acc} = 3422$ V

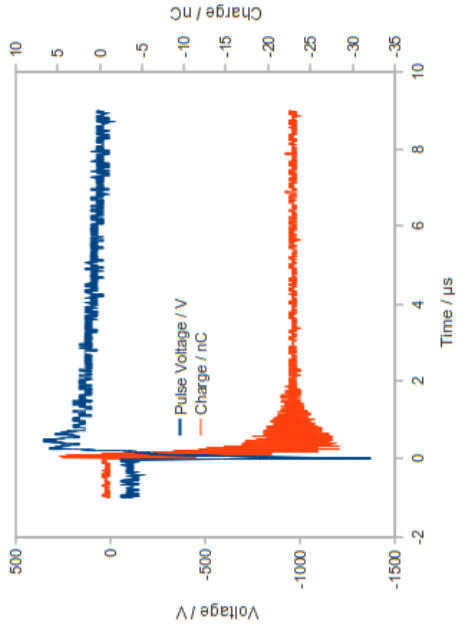

(c) $V_{acc} = 3955$ V

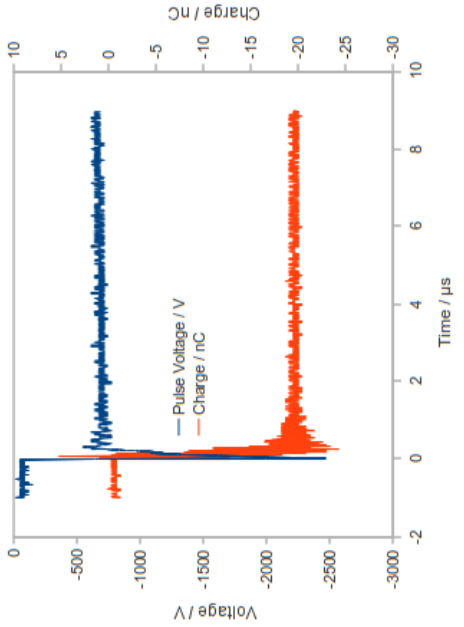

(d) $V_{acc} = 5021$ V

Figure 7.12: Pulse voltage and emission current profiles for the pyro accelration system, 10 pF C_{acc} , diode

7.2.5 Emission Process

This section will detail the differences in the emission process that result in the differing emission properties.

7.2.5.1 C_{acc} = 50 pF, no diode

Figures 7.13 and 7.14 show the emission process for the pyroelectric acceleration system with C_{acc} = 50 pF and no shunt diode when the acceleration voltage V_{acc} is small and large respectively. Figures 7.13a to 7.13c and 7.14a to 7.14d show the same usual process: The pulse is applied to the front electrode of the cathode, the plasma forms and emission begins. After this point the emission process differs depending on the charge, and therefore voltage on the anode V_{acc} . This difference is due to the collected charges reducing the voltage on the anode. If the voltage on the anode is small then the emitted charges can reverse the voltage on the anode, retarding any further charge collection. This situation is shown in Fig 7.13d With a larger voltage on the anode the voltage reduces but does not reverese, so further charge collection is not prevented. This process is shown in Figs 7.14d to 7.14f.

7.2.5.2 C_{acc} = 50 pF, with diode

Figures 7.15 and 7.16 show the emission process for the pyroelectric acceleration system with C_{acc} = 50 pF and the shunt diode when the the acceleration voltage V_{acc} is small and large respectively. Figures 7.15a to 7.15c and 7.16a to 7.16c show the usual process of pulse application, plasma formation and the start of emission. This process is similar to that described above. After this point the two emission processes are again different. With a small voltage (Fig 7.15d) the

process is the same as with no shunt diode, since the cathode voltage $V_{cathode}$ does not become positive due to the small positive / negative votlage on the cathode. If V_{acc} is large the emission may result in the cathode voltage $V_{cathode}$ dropping to 0 V, as shown in Figs 7.16d and 7.16e. As the $V_{cathode}$ passes 0 V conduction may begin through the cathode, as shown in Fig 7.16f. This allows additional emission to occur when compared to the case with no diode.

The observations presented here explain the emission properties shown in Fig 7.3a, where the emitted charge with and without the diode is similar with a small V_{acc} , but become increasingly different with increasing V_{acc} .

7.2.5.3 C_{acc} = 10 pF, no diode

Figure 7.17 shows the emission process for the pyroelectric acceleration system with C_{acc} = 10 pF and without the shunt diode. Figure 7.17a shows the pulse application, and Fig 7.17b shows the formation of the plasma. In Fig 7.17c electron emission begins. At this point the greater V_{acc} the greater the charge extracted from the plasma. The voltage on the anode V_{acc} falls due to the collected electrons, and may become 0 V if sufficient electrons are collected. Thus any further electrons collected by the anode would result in a negative voltage on the anode strongly opposing any further collection of electrons. Since a higher V_{acc} resulted in greater emission it also results in greater charge being repelled back towards the cathode. This greater amount of charge repelled back towards the cathode results in an increasing negative voltage on the cathode at the end of emission with increasnig acceleration voltage. This is the situation shown in Fig 7.17d

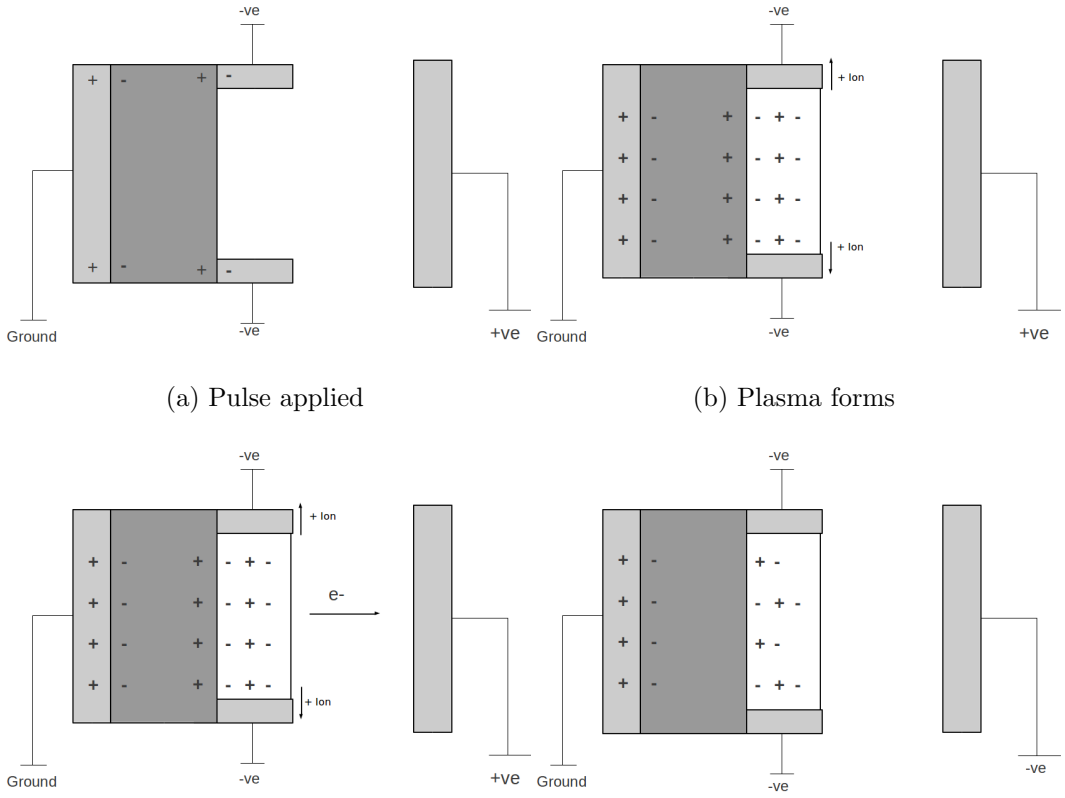

(a) Pulse applied

(b) Plasma forms

(c) Emission begins / V_{acc} falls

(d) Emission ends / V_{acc} reversed

Figure 7.13: Negative pulse to the front electrode with C_{acc} = 50 pF and no shunt diode, when V_{acc} is small.

7.2.5.4 C_{acc} = 10 pF, with diode

The emission process in this case is similar to that in the C_{acc} = 10 pF, no didoe case. However, the additional aspect of electron flow through the diode compensating positive charges in the plasma in some circumstances may lead to the varied behaviour seen in the pulse voltage time profiles.

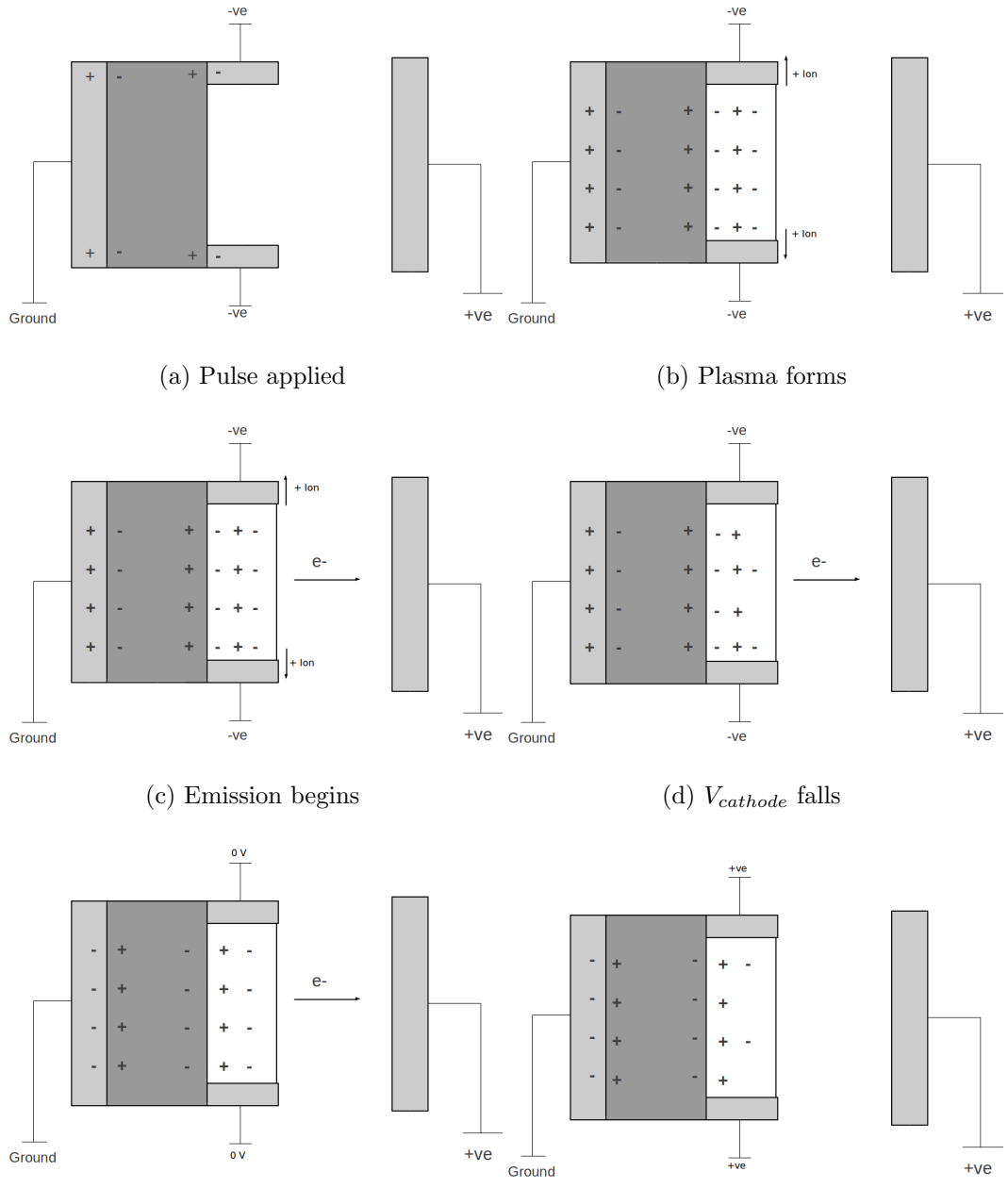

(a) Pulse applied

(b) Plasma forms

(c) Emission begins

(d) $V_{cathode}$ falls

(e) $V_{cathode} = 0$ V

(f) Emission ends

Figure 7.14: Negative pulse to the front electrode with $C_{acc} = 50$ pF and no shunt diode, when V_{acc} is large.

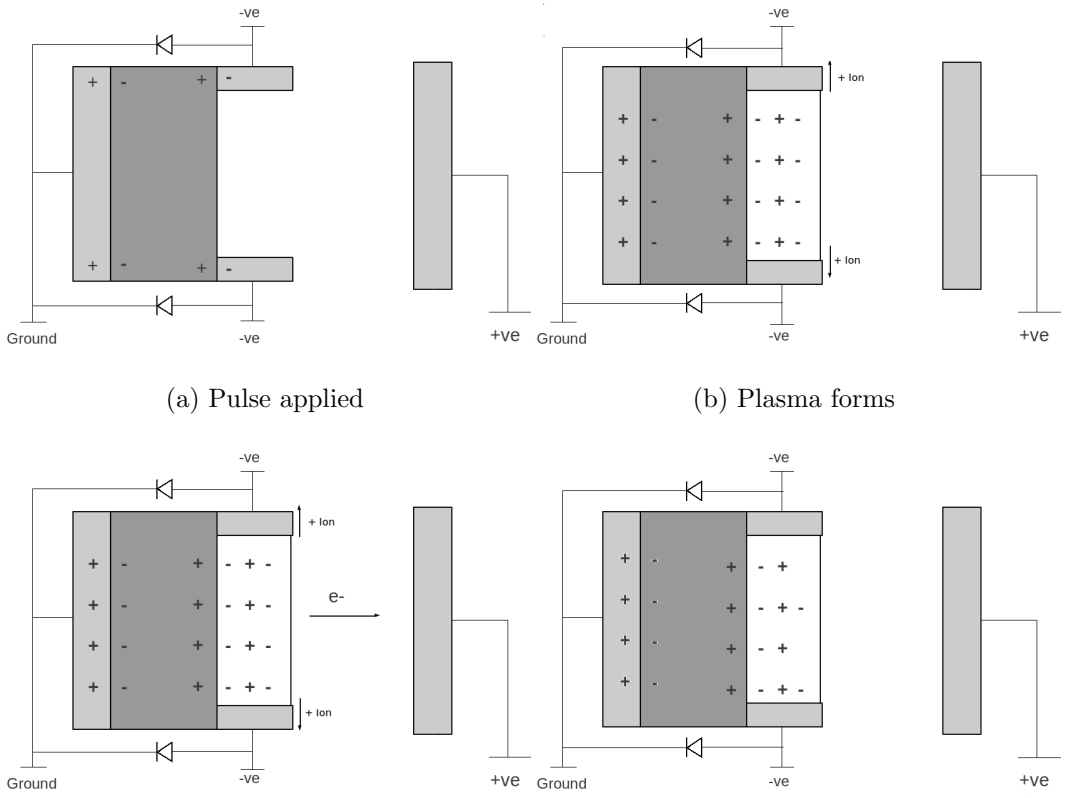

(a) Pulse applied

(b) Plasma forms

(c) Emission begins

(d) Emission ends

Figure 7.15: Negative pulse to the front electrode with $C_{acc} = 50$ pF and with shunt diode, when V_{acc} is small.

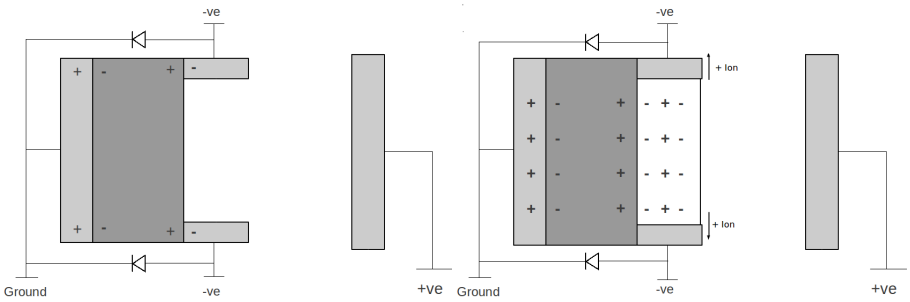

(a) Pulse applied

(b) Plasma forms

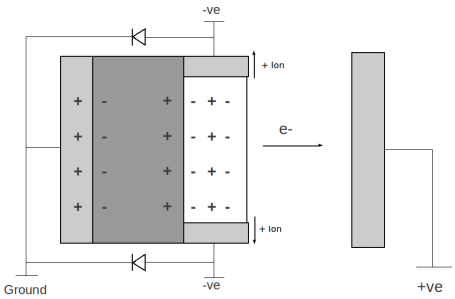

(c) Emission begins

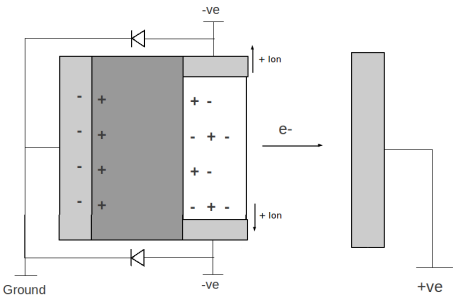

(d) $V_{cathode}$ drops

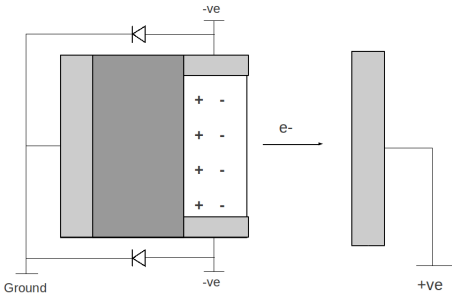

(e) $V_{cathode} = 0$ V

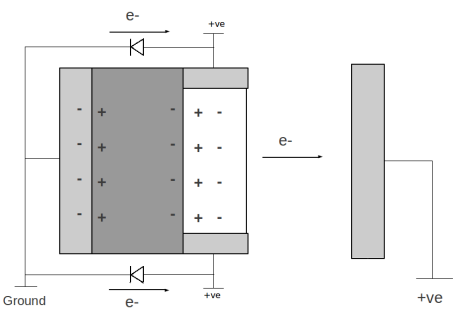

(f) Diode conducts

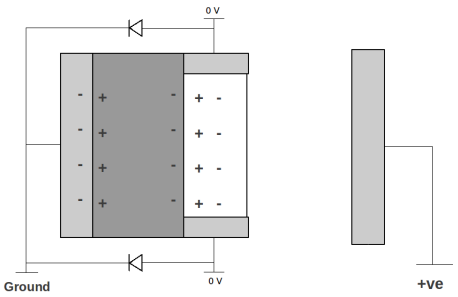

(g) Emission ends

Figure 7.16: Negative pulse to the front electrode with $C_{acc} = 50$ pF and with shunt diode, when V_{acc} is large.

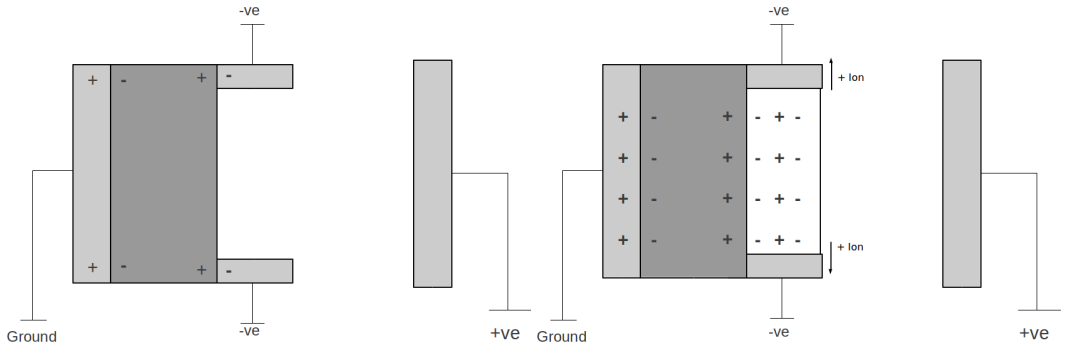

(a) Pulse applied

(b) Plasma forms

(c) Emission begins / V_{acc} falls

(d) Emission ends / Vcat is larger

Figure 7.17: Negative pulse to the front electrode with C_{acc} = 10 pF and no shunt diode.

7.3 Conclusions

This section of the thesis has demonstrated the feasibility of an electron beam generation and acceleration device based on high voltages generated by a pyroelectric system in conjunction with a ferroelectric cathode. Several configurations have been demonstrated with differing properties, showing that the previously useful shunt diode is only beneficial in certain configurations. The electrical condition of the system, in particular the section of the system which provides the dominant source of charge is very important in this configuration and small changes can result in significantly different emission properties.

Chapter 8

Conclusions

This project has demonstrated that the pyroelectric coefficient of PZT is different under open and short circuit condition, and that the use of laminar composites of PZT and stainless steel show an enhancment of the pyroelectric coefficient compared to bare PZT. Use of two systems for the measurment of the pyroelectric coefficient under open and short cirucit condition showed differences in the pyroelectric coefficient under both high and rough vacuum. Use of PZT-5A samples prepared as laminar composites with stainless steel showed increasing thicknesses of stainless steel compared to PZT thickness resulted in increasing enhamcement of the measured pyroelectric coefficient compared to the bare PZT value.

The use of a pyroelectric crystal to charge a circuit, which was then switched to generate a high voltage pulse has been demonstrated. Increasing the capacitance of this charging circuit increases the voltage of the produced pulse on a capacitive load. Both positive and negative voltage pulses were produce using this method. Use of these pyroelectric pulses to fire a ferroelectric cathode has been demonstrated. Use of a negative voltage applied to the rear electrode was found to be the optimum configuration for maximizing emitted electron charge

and current. Several differing front electrode grid structures for the cathode were shown to have little effect of the emission properties of the cathode.

The use of an accelerating voltage in conjunction with the pyroelectric pulse / ferroelectric cathode system has been demonstrated. Increasing the accelerating voltage increased the current and charge emitted by the cathode. The use of a diode connected in parallel with the cathode was shown to increase the emitted charge and current, with the improvement being more pronounced at higher acceleration voltages.

The use of a second pyroelectric crystal as the accelerating component for the system was demonstrated. A capacitor connected in parallel with the accelerating crystal is used to store the charge. A larger value of this capacitance gives a lower acceleration volatge for a given temperature change of the pyroelectric crystal, but results in greater charge collection at a given acceleration voltage. A diode connected in parallel with the cathode was shown to increase charge collection with a 50 pF capacitor in parallel with the accelerating crystal, but not with a 10 pF capacitor.

This project has shown the feasability of an electron beam generation and acceleration device based on a ferroelectric cathode fired by a pyroelectrically generated pulse and with acceleration voltage provided by a further pyroelectric element, although some development is still required for a practical system. Discussion of how to address some of these issuse is given in the next chapter.

Chapter 9

Future Work

Areas for futher work in on this technology have been identified and are presented in the following section.

9.1 System resetting

The major limitation of the present system when considering commercial applications is the time taken to reset the system. This is due to the only method of charge replenishment on the pulsing and acceleration sections is the vent the vacuum chamber to expose the charging elements to free charges is the atmosphere. Addressing may be sufficient to make this technology commercially viable. A method proposed for this is to construct a custom designed electrical relay. Such a relay should have a minimal structure so as to increase electrical conduction between the terminals. The material used for this purpose should also have a very high resistivity and dielectric strength. A suitable design may be a small plate of a ceramic material such as Macor or alumina. Such materials

have resistivities in excess of $10^{14}\Omega m$ [51, 52]. If only a minimal amount of structural material is used the current leakage through it will be negligible; a section of dimensions $2x1x0.5cm$ gives a resistance of $4x10^{16}\Omega$ along the 2 cm direction. The charge leakage through the vacuum should be considered negligible since it does not prevent charge build up in a normal emission run.

9.2 Increase in electron/x-ray energy and intensity

A greater range of energies and intesities avaliable would further broaden the range of potential applications. Possible methods to achieve this include using a greater temperature change on the accelerating $LiTaO_3$. This would enhance both the emission current and charge, as well as increasing the electron energy. Investigations could also be made into the shape of the used, e.g. a sample with greater surface are but the same thickness could increase the total charge avaliable at the expense of greater energy required for heating. Development of the repeated firing technique (see subsection 5.2.7) could also be a useful method for increasing the firing rate of the system by allowing several firings within one temperature cycle. Due to safety concern no voltage above 5 kV is produced during any stages of the experiments, therefore no hazardous X-rays were produced.

9.3 X-ray generation

Since this project has shown that electrons are accelerated into a metallic target, it can reasonably be believed that soft x-rays are generataed. However it would

be useful to directly detect these x-rays and analyse the specetrum of energies and intensities. This would allow the range of potential applications to be determined since different applications require different energies and intensities.

9.4 Packaging of system

At present the system is in a form suitable for research, which is not suitable for commercial use for several reasons, including size, cost and complexity of operation. The sytem could potentially be made into a compact bench-top form which would be substantially cheaper, smaller and could be made very easy operate. For example the system could be package in a system similar to that of the Amptek Cool-X [8], and use a similar operating scheme, i.e. an on/off switch and an 'operate/stop' switch.

References

[1] S. B. Lang, "Pyroelectricity: From ancient curiosity to modern imaging tool," *Physics Today*, vol. 58, no. 8, p. 31, 2005. 1, 8

[2] J. D. Brownridge and S. M. Shafroth, "Electrons and positive ion beams and x-rays produced by heated and cooled pyroelectric crystals such as linbo3 and litao3 in dilute gasses: Phenomenology and applications." 1, 10, 11

[3] J. D. Brownridge and S. M. Shafroth, "X-ray fluoresced high-z (up to z =82) k x rays produced by linbo 3 and litao3 pyroelectric crystal electron accelerators," *Applied Physics Letters*, vol. 85, no. 7, pp. 1298–1300, 2004. Cited By (since 1996): 9. 1, 11

[4] J. B. D. and S. Roboy, "Investigations of pyroelectric generation of x rays," *Japanese Journal of Applied Physics*, vol. 86, no. 1, p. 640, 1999. 1, 11

[5] J. A. Geuther and Y. Danon, "High-energy x-ray production with pyroelectric crystals," *Journal of Applied Physics*, vol. 97, no. 10, pp. 1–5, 2005. 1, 28

[6] J. Geuther, Y. Danon, and F. Saglime, "Nuclear reactions induced by a pyroelectric accelerator," *Phys.Rev.Lett.*, vol. 96, p. 054803, Feb 2006. 1

[7] B. Naranjo, J. G. K., and S. Putterman, "Observation of nuclear fusion driven by a pyroelectric crystal," *Nature*, vol. 434, p. 1115, 2005. 1, 11

[8] Amptek, "Cool-x device," 03/18/2008 2008. 1, 31, 32, 121, 157

[9] H. H. S. Chang, R. W. Whatmore, and Z. Huang, "Pyroelectric effect enhancement in laminate composites under short circuit condition," *Journal of Applied Physics*, vol. 106, no. 11, 2009. 2, 22, 61, 71

[10] H. H. S. Chang and Z. Huang, "Pyroelectric effect enhancement through product property under open circuit condition," *Journal of Applied Physics*, vol. 106, no. 1, 2009. Cited By (since 1996): 1. 2, 22, 23, 24, 62

[11] M. E. Lines and A. M. Glass, *Principles and Applications of Ferroelectrics and Related Materials*, p. 12. 1996. 8, 12, 99, 123

[12] C. Keawboonchuay and T. G. Engel, "Maximum power generation in a piezoelectric pulse generator," *Plasma Science, IEEE Transactions on*, vol. 31, no. 1, pp. 123–128, 2003. ID: 1. 9, 21

[13] T. G. Engel, C. Keawboonchuay, and W. C. Nunnally, "Energy conversion and high power pulse production using miniature piezoelectric compressors," *IEEE Transactions on Plasma Science*, vol. 28, no. 5, pp. 1333–1337, 2000. 9, 21

[14] T. G. Engel, W. C. Nunnally, J. Becker, R. Rahman, and C. Keawboonchuay, "Research progress on compact kinetic-to-electrical energy convertors," in *12th IEEE International Pulsed Power Conference*, vol. 2, (Piscataway, NJ, United States), pp. 1287–1290, Affiliation: Univ of Missouri-Columbia, Columbia, United States; Correspondence Address: Engel, T.G.; Univ of Missouri-Columbia, Columbia, United States, IEEE, 27 June 1999 through 30 June 1999 1999. Conference code: 56431. 9, 21

[15] C. Keawboonchuay and T. G. Engel, "Electrical power generation characteristics of piezoelectric generator under quasi-static and dynamic stress conditions," *IEEE transactions on ultrasonics, ferroelectrics, and frequency control*, vol. 50, no. 10, pp. 1377–1382, 2003. Cited By (since 1996): 30. 9, 21

[16] K. Yoo, C. W. Moon, W. Choi, S. Kim, E. Bae, and S. Chung, "Feasibility studies on pyroelectric emission for lithography application," *Integrated ferroelectrics*, vol. 41, 2001. 11

[17] L. E. Neidholdt and L. J. Beauchamp, "Ambient pressure pyroelectric ion source for harsh environment mass spectrometry." 11

[18] S. Chen, X. Dong, S. Zheng, Z. Zhu, and C. Tang, "Electron emission and phase transitions of zr-rich lead zirconate titanate ferroelectrics," *Materials Letters*, vol. 61, no. 11-12, p. 2439, 2007. 13, 20

[19] S. Chen, X. Dong, S. Zheng, Z. Zhu, and C. Tang, "Electron emission from barium strontium titanate ceramics," *Journal of the American Ceramics Society*, vol. 89, no. 7, p. 2118, 2006. 13, 15

[20] L. L. Zhang, Y. J. Feng, Z. Xu, and Z. X. Sheng, "Electron emission from la-doped pb(zr,sn,ti)o3 anti-ferroelectrics by pulse electric field and the relevant physical mechanism," *Chinese Science Bulletin*, vol. 54, no. 19, p. 3489, 2009. 13

[21] S. Chen, S. Zhang, X. Cai, and S. Guo, "Experimental study on the mechanism of the ferroelectric emission from plzt ceramics," *Microelectronics Engineering*, vol. 66, p. 670, 2003. 14

[22] A. Dunaevsky, Y. E. Krasik, J. Feisteiner, S. Dorfman, NewAuthor4, and A. Sternlieb, "Lifetime of ferroelectric cathodes," *Journal of Applied Physics*, vol. 89, no. 8, p. 4480, 2001. 17

[23] O. Peleg, K. Chirko, V. Gurovich, J. Felsteiner, Y. K. E., and V. Bernshtam, "Parameters of plasma produced at the surface of a ferroelectric cathode by different driving pulses," *Journal of Applied Physics*, vol. 97, no. 11, p. 3307, 2005. 18

[24] H. Riege, "Electron emission from ferroelectrics - a review," *Nuclear Instruments and Methods in Physics Research*, no. 340, p. 80, 1994. 19, 20

[25] Z. X. Sheng, Y. J. Feng, Z. Xu, and X. Sun, "Electron emission from la-doped lead zirconate stannate titanate antiferroelectric ceramic under fast electric field pulses," *Journal of Material Science*, vol. 44, p. 556, 2008. 19

[26] G. Mesyats, "Physics of electron emission from metal-dielectric cathodes," *IEEE Transactions on Dielectrics and Electrical Insulation*, vol. 2, no. 2, 1995. 20

[27] B. Jiang, G. Kirkman, and N. Riehardt, "High brightness electron beam produced by a ferroelectric cathode," *Applied Physics Letters*, vol. 66, no. 10, p. 1196, 1994. 20

[28] F. Liu and B. C. Fleddermann, "Electron emission from thin-film ferroelectric cathodes," *Applied Physics Letters*, vol. 76, no. 12, 2000. 20

[29] M. Seo and K. Hong, "characteristics of electron emission from a (pb,la)(zr,ti)03 ferroelectric cathode," *Japanese Journal of Applied Physics*, vol. 49, no. 7, p. 076001, 2010. 20

[30] J. Z. Gleizer, A. Krokmal, Y. E. Krasik, and J. Felsteiner, "Investigation of a hollow anode with an incorporated ferroelectric plasmasource for generation of high-current electron beams," *Journal of Applied Physics*, vol. 94, no. 10, p. 6319, 2003. 20

[31] A. Moorti, P. A. Naik, and P. D. Gupta, "High-current-density electron emission fromlead zirconium titanate ferroelectric disc underapplication of short-duration high-voltage pulses," *IEEE Transactions on Plasma Science*, vol. 32, no. 1, p. 256, 2004. 20

[32] G. Benedek, I. Boscolo, J. Handerek, and H. Riege, "Electron emission from ferroelectric/antiferroelectric cathodes excited by short high-voltage pulses," *Journal of Applied Physics*, vol. 81, no. 3, p. 1396, 1996. 20

[33] Y. Hayashi, D. Fletchner, and E. Hotta, "Characteristics of electron emission from pzt ferroelectric cathode under strong accelerating field," *Journal of Physics D: Applied Physics*, vol. 35, p. 281, 2002. 20, 21

[34] C. Keawboonchuay and T. G. Engel, "Design, modeling, and implementation of a 30-kw piezoelectric pulse generator," *Plasma Science, IEEE Transactions on*, vol. 30, no. 2, pp. 679–686, 2002. ID: 1. 21

[35] C. Keawboonchuay and T. G. Engel, "Scaling relationships and maximum peak power generation in a piezoelectric pulse generator," *IEEE Transactions on Plasma Science*, vol. 32, no. 5 I, pp. 1879–1885, 2004. Cited By (since 1996): 2. 21

[36] C. Keawboonchuay and T. G. Engel, "Factors affecting maximum power generation in a piezoelectric pulse generator," in *14th IEEE International Pulsed Power Conference* (G. M. and N. A., eds.), pp. 327–330, Affiliation: Department of Electrical Engineering, University of Missouri-Columbia, Columbia, MO 65211, United States; Correspondence Address: Keawboonchuay, C.; Department of Electrical Engineering, University of Missouri-Columbia, Columbia, MO(TRUNCATED), 15 June 2003 through 18 June 2003 2003. 21

[37] H. H. S. Chang and Z. Huang, "Substantial pyroelectric effect enhancement in laminated composites," 2008. Cited By (since 1996): 1. 22, 61, 71

[38] H. H. S. Chang and Z. Huang, "Laminate composites with enhanced pyroelectric effects for energy harvesting," *Smart Materials and Structures*, vol. 19, no. 6, 2010. 22, 61

[39] M. J. Hockley, H. S. S. Chang, and Z. Huang, "Pyroelectric coefficient under open circuit condition and its enhancements through product property," *Proceedings of the 2010 IEEE International Symposium on the Applications of Ferroelectrics, ISAF 2010, Co-located with the 10th European Conference on the Applications of Polar Dielectrics, ECAPD 2010*, 2010. 23

[40] M. J. Hockley, H. S. S. Chang, and Z. Huang, "Pyroelectric coefficient differrence under open and short circuit conditions and their enhancement in laminate composites," *Journal of Applied Physics*, vol. 109, no. 6, 2011. 23

[41] R. E. Newnham, D. P. Skinner, and L. E. Cross, "Connectivity and piezoelectric-pyroelectric composites," *Materials Research Bulletin*, vol. 13, pp. 525–536, 5 1978. 23, 61

[42] C. W. Nan, "Product property between thermal expansion and piezoelectricity in piezoelectric composites: pyroelectricity," *Journal of Material Science Letters*, vol. 13, no. 19, p. 1392, 1994. 23, 61

[43] J. N. F., *Physical properties of crystals*. Oxford University Press, 1979. 23

[44] W. S. T., *Fundamentals of X-Ray Tubes*, p. 7. X-Rays in Practice, McGraw-Hill Book Company, Inc, first ed., 1946. 25

[45] "http://home.comcast.net/ znhakim/web6/gasdischargetubes/earlycrookestube.htm." 25

[46] "http://www.orau.org/ptp/collection/xraytubescoolidge/coolidgeinformation.htm." 26

[47] Almaz Optics Inc. 28

[48] B. Rosenblum, P. Braunlich, and J. P. Carrico, "Thermally stimulated field emission from pyroelectric linbo3," *Applied Physics Letters*, vol. 25, no. 1, p. 17, 1974. 29

[49] J. D. Brownridge and S. M. Shafroth, "Using static charges on pyroelectric to produce self-focussing electron and ion beams and transport through tubes," *Journal of Electrostatics*, vol. 63, p. 249, 2005. 29

[50] "http://www.rdmag.com/awards/rd-100-awards/2003/09/2003-r-d-100-award-winners/." 32

[51] "http://www.pgo-online.com/intl/katalog/macor.html." 156

[52] "http://www.azom.com/article.aspx?articleid=3382." 156

Appendix A: Research Papers

APPENDIX A: RESEARCH PAPERS

Figure 1: Journal of Applied Physics, 2011

JOURNAL OF APPLIED PHYSICS **109**, 064102 (2011)

Pyroelectric coefficient difference under open and short circuit conditions and their enhancements in laminate composites

M. J. Hockley, H. H. S. Chang, and Z. Huang[a)]
Department of Materials, Cranfield University, Bedfordshire MK43 0AL, United Kingdom

(Received 13 January 2011; accepted 23 January 2011; published online 17 March 2011)

The pyroelectric coefficient is normally measured under the short circuit condition, while many pyroelectric applications are under the open circuit condition. We present experimental results demonstrating a difference in the pyroelectric coefficient under open and short circuit conditions. We also present results on pyroelectric coefficient enhancement using laminate composites, and show that this technique can enhance the pyroelectric coefficient at open circuit condition, as well as at short circuit condition. © *2011 American Institute of Physics*. [doi:10.1063/1.3559268]

I. INTRODUCTION

The pyroelectric (PY) effect is the change in spontaneous polarization of a material in response to a temperature change, and is exhibited by all materials with a polar axis. The PY effect includes the primary and secondary effects, and can be expressed as[1]

$$P_m^{T,E} = P_m^{S,E} + d_{mkl}^{E,\Theta} c_{ijkl}^{E,\Theta} \alpha_{ij}^{T,E}, \quad (1)$$

where T, E, S, and Θ represent stress, electric field, strain, and temperature, respectively. $P_m^{T,E}$ is the total PY coefficient at constant stress and electric field, $P_m^{S,E}$ is the primary PY coefficient at constant strain and electric field, $d_{mkl}^{E,\Theta}$ is the piezoelectric constant, $c_{ijkl}^{E,\Theta}$ is the elastic stiffness at constant temperature and electric field, and $\alpha_{ij}^{T,E}$ is the thermal expansion coefficient at constant stress and electric field. Equation (1) describes the PY effect under the short circuit condition since all terms are at constant electric field. However, many pyroelectric applications use materials in the open circuit condition, such as thermal imaging, motion detection and more recently pyroelectric x- ray and neutron generation.[2–5] Previously, we have reported calculated PY coefficients under open circuit (OC) and short circuit (SC) conditions and the results indicated that the PY coefficients may be different under OC and SC conditions[6,7] for some materials. Here we present the results of experimental investigation on this matter.

In Eq. (1) the term $d_{mkl}^{E,\Theta} c_{ijkl}^{E,\Theta} \alpha_{ij}^{T,E}$ gives the secondary PY coefficient, which arises from the piezoelectric response to the strain induced by thermal expansion. The possibility of utilizing secondary PY effect to enhance the total PY coefficient was researched by Newnham *et al.*[8] and Nan.[9] Their works led to the development of various composites with superior mechanical flexibility accompanied by good PY performances.[10–14] They concluded that in most cases due to the small hydrostatic piezoelectric effect, arising from cancellation between coefficients of opposite signs, the enhancement available through the secondary contribution is rather limited.

In our previous communications, we demonstrated by both modeling and measurement under short circuit condition that the use of a laminar composite structure of lead zirconate titanate (PZT) sandwiched between two stainless steel sheets can increase the PY coefficient of the PZT significantly.[7,15] This is due to the steel having a very different coefficient of thermal expansion to that of the PZT. This mismatch leads to the forced strain of the PZT, enhancing the secondary pyroelectric effect. In another communication through numerical calculation we suggested that this pyroelectric enhancement in laminar composite exists also under open circuit conditions,[6] the experimental results confirming this will also been presented in this communication.

II. EXPERIMENTAL

Pyroelectric PZT-5A (Piezo Systems Inc., USA) samples were heated and cooled using a custom built Peltier stage, which comprised a Peltier element bonded to a blanking plate and heat-sink on one surface, and a 4 mm thick aluminum plate on the other. This aluminum plate evenly distributed the heat produced, preventing any significant tertiary PY effect.[1] The Peltier element and a thermistor for temperature monitoring were connected to a PC via a control circuit. The PC was used to control and record the Peltier temperature. The PZT samples were connected to a custom made voltage follower circuit with a very high input impedance in excess of 1.5 TΩ. The output of the voltage follower circuit was monitored by an oscilloscope (Agilent MSO6104A). The experiments were conducted under a vacuum of approximately 4×10^{-5} Torr, maintained by a turbomolecular pump. The samples were heated to 5 K above room temperature, and then allowed to cool slowly. During the cooling the voltage produced was recorded using the oscilloscope. A sampling rate of 20 Hz was used for both the voltage and temperature, with a run time of 50 s. The PY coefficient was calculated from the plot of voltage versus temperature.

The voltage follower circuit was used in two configurations, one for the open circuit condition and the other for the short circuit condition. Equivalent circuit for both systems are shown in Fig. 1. The OC system used a standard voltage follower, with the PZT sample being connected to the input. The very high impedance of the input resulted in almost all the produced charge remaining on the PZT during the course

a)Electronic mail: z.huang@cranfield.ac.uk.

Figure 2: IEEE Proceedings of ISAF, 2010

Pyroelectric coefficient under open circuit condition and its enhacement through product property

M. J. Hockley, H. H .S. Chang, Z. Huang
Department of Materials
Cranfield University
Bedfordshire, MK43 0AL, United Kingdom

This paper presents experimental results showing an increase in the pyroelectric coefficient of PZT ceramic when bonded between two layers of stainless steel to form a laminated composite structure. This enhancement is shown to be dependent on the ratio of thickness of PZT to steel, with small ratios showing the greatest enhancement. Experimental results are also presented showing a difference in the pyroelectric coefficient of these composites when measured under the short or open circuit conditions.

I. INTRODUCTION

The pyroelectric effect is the change in surface charge density of a material in response to a change in temperature. All materials with a polar axis exhibit this effect. The pyroelectric coefficient can be expressed as:

$$\rho = \frac{\Delta P_s}{\Delta T} \quad (1)$$

where ΔPs is the change of spontaneous polarization, ρ is the pyroelectric coefficient and ΔT is the temperature change. The pyroelectric effect has many applications, such as thermal imaging, intruder detectors and more recently x ray generation[1; 2]. Some of these applications are performed with the pyroelectric material in the open circuit condition, while pyroelectric coefficients are usually measured at the short circuit condition.

Theoretical work on the subject of open and short circuit pyroelectric coefficients has been conducted by Chang and Huang[3]. Their work has shown that there may be a difference between the open circuit and short circuit pyroelectric coefficient for some materials. This difference is due to the secondary pyroelectric effect, which is a piezoelectric response due to the strain generated in the material during a temperature change. This component is added to the primary coefficient to obtain the total coefficient, as shown below:

$$\rho_m^{T,E} = \rho_m^{S,E} + d_{mkl}^{E,\Theta} c_{ijkl}^{E,\Theta} \alpha_{ij}^{T,E} \quad (2)$$

where $\rho_m^{T,E}$ is the total pyroelectric coefficient measured at constant stress, $\rho_m^{S,E}$ is the primary coefficient at constant strain, $d_{mkl}^{E,\Theta}$ is the piezoelectric constant, $c_{ijkl}^{E,\Theta}$ is the elastic stiffness and $\alpha_{ij}^{T,E}$ is the thermal expansion coefficient. This clearly shows that if the two components of the coefficient are of the same sign, an increase in the secondary coefficient will result in an increase in the total coefficient, while if the two components are of opposite sign a decrease in the secondary component will result in an overall increase.

Their work has also shown, both analytically and experimentally that the use of pyroelectric material in a composite structure of PZT sandwiched between two stainless steel sheets, can increase the pyroelectric coefficient of the PZT significantly[4; 5]. This effect is again due to the secondary pyroelectric effect, with the steel having a different coefficient of thermal expansion to that of the PZT. This mismatch leads to the forced strain of the PZT, enhancing the secondary effect. It should also be noted that there still remains much room for improvement in this technique, as smaller thickness ratios will give greater increases still, and improved bonding between the laminate layers will also improve matters. Similar studies have been performed using PZT thin films on a substrate material to create stress, and therefore increase the secondary effect in a manner similar to that described above[6; 7].

In this paper we present results of the measurement of the pyroelectric coefficient of PZT laminate composites of various thickness ratios, for both open and short circuit conditions.

II. EXPERIMENTAL

The PZT5A was commercially sourced from Piezo Systems INC. PZT of thickness 127, 191 and 267 μm was used in conjunction with stainless steel (SS) of thickness 50, 125 and 250 μm to achieve several thickness ratios of PZT:SS in the range 0.25 to 2.7. The composites were produced as detailed by Chang and Huang[4]. The composite structure is shown schematically in fig. 1.

A system for controlling the temperature of the samples was constructed using a Peltier element controlled by a Supercool

Figure 1. Structure of the PZT composites. The outer lightly coloured layers are the stainless steel, and the darker inner layer is the PZT.

978-1-4244-8191-0/10/$26.00 ©2010 IEEE

Appendix B: Circuits

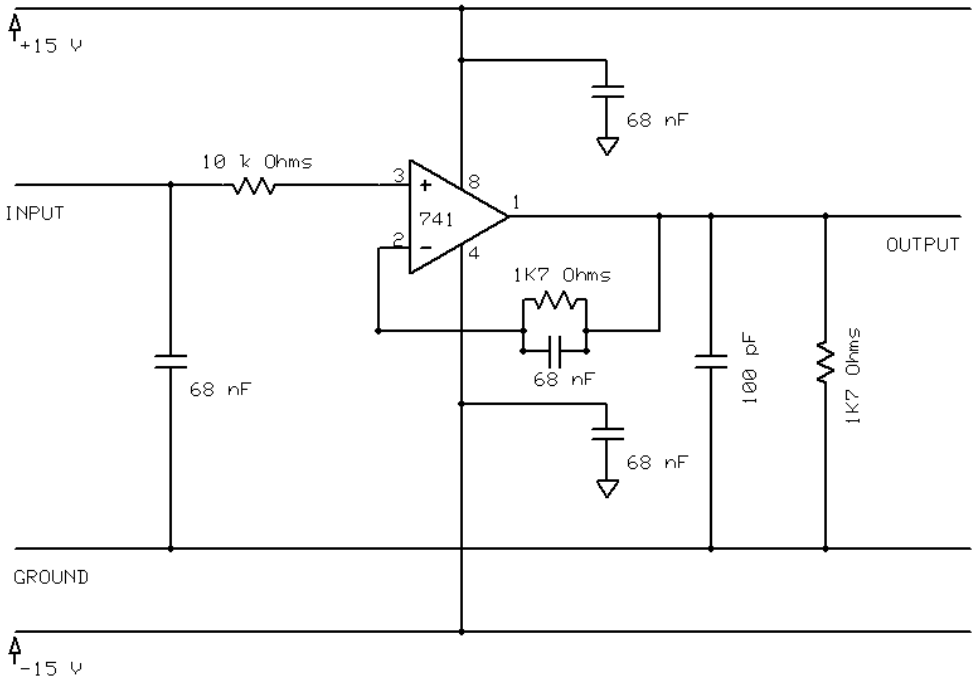

Figure 3: Schematic of the voltage follower circuit used in the OC pyroelectric experiments

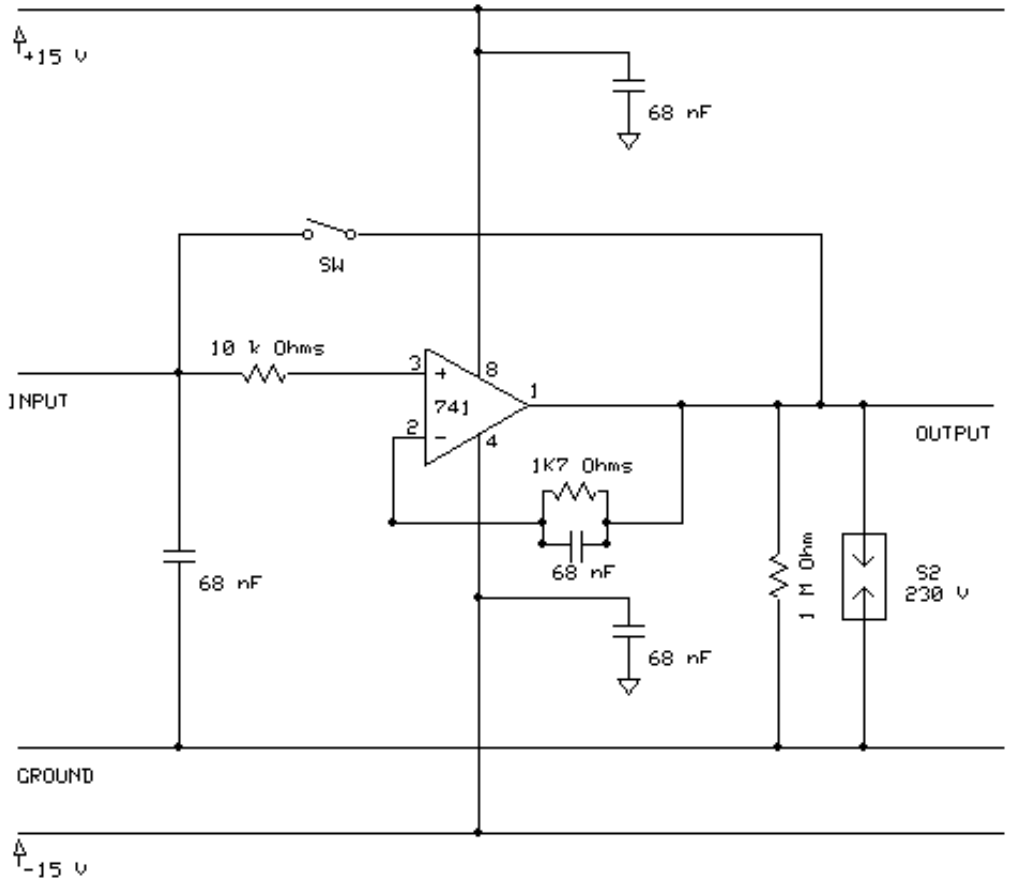

Figure 4: Circuit diagram of the emission current and acceleration voltage measurement circuit. When switch SW is open the pyro acceleration voltage is measured, when it is closed the charge is measured. S2 is a spark gap protecting the measurement device in case of electrical failure of any high voltage components.

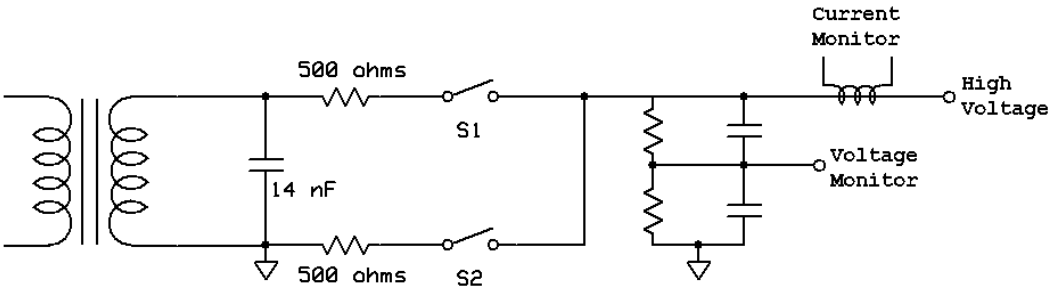

Figure 5: Schematic of the high voltage pulse generation circuit with measurement circuit shown. The 14 nF capacitor is charge with S1 and S2 open. The voltage pulse is then applied by closing S1. The pulse is stopped by closing opening S1 and closing S2, grounding the load.

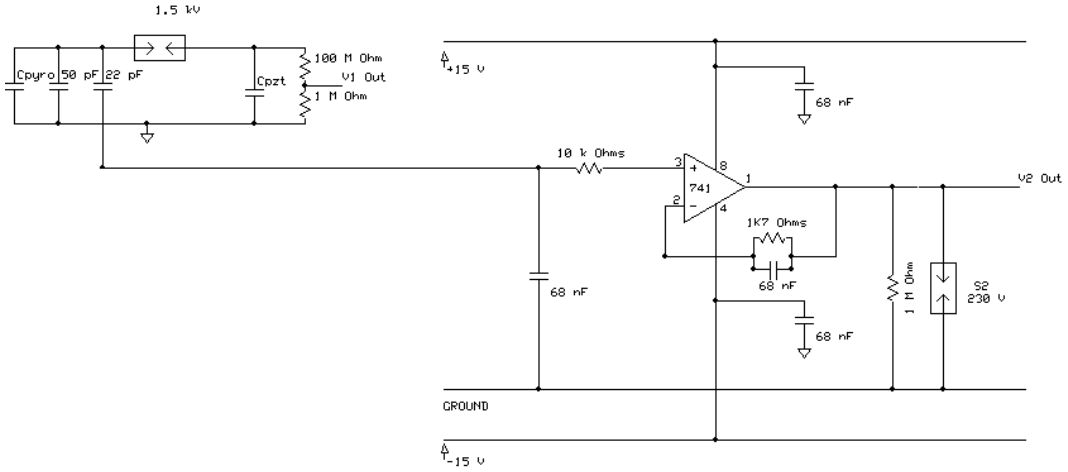

Figure 6: Schematic of the V1 V2 measurement system showing the resistive divider for the measurement of V1 and the capacitive divider / voltage follower system of the V2 measurement system.